doi:10.1088/0067-0049/199/2/31

FERMI LARGE AREA TELESCOPE SECOND SOURCE CATALOG[*]

P. L. Nolan[1,82], A. A. Abdo[2,83], M. Ackermann[3], M. Ajello[1], A. Allafort[1], E. Antolini[4,5], W. B. Atwood[6],
M. Axelsson[7,8,9], L. Baldini[10], J. Ballet[11], G. Barbiellini[12,13], D. Bastieri[14,15], K. Bechtol[1], A. Belfiore[6,16,17],
R. Bellazzini[10], B. Berenji[1], G. F. Bignami[18], R. D. Blandford[1], E. D. Bloom[1], E. Bonamente[4,5], J. Bonnell[19,20],
A. W. Borgland[1], E. Bottacini[1], A. Bouvier[6], T. J. Brandt[21,22], J. Bregeon[10], M. Brigida[23,24], P. Bruel[25], R. Buehler[1],
T. H. Burnett[26], S. Buson[14,15], G. A. Caliandro[27], R. A. Cameron[1], R. Campana[28], B. Cañadas[29,30], A. Cannon[19,31],
P. A. Caraveo[17], J. M. Casandjian[11], E. Cavazzuti[32], M. Ceccanti[10], C. Cecchi[4,5], Ö. Çelik[19,33,34], E. Charles[1],
A. Chekhtman[35,83], C. C. Cheung[36,83,84], J. Chiang[1], R. Chipaux[37], S. Ciprini[5,38], R. Claus[1], J. Cohen-Tanugi[39],
L. R. Cominsky[40], J. Conrad[8,41,85], R. Corbet[19,34], S. Cutini[32], F. D'Ammando[28,42], D. S. Davis[19,34], A. de Angelis[43],
M. E. DeCesar[19,20], M. DeKlotz[44], A. De Luca[18], P. R. den Hartog[1], F. de Palma[23,24], C. D. Dermer[45], S. W. Digel[1],
E. do Couto e Silva[1], P. S. Drell[1], A. Drlica-Wagner[1], R. Dubois[1], D. Dumora[46], T. Enoto[1], L. Escande[46], D. Fabiani[10],
L. Falletti[39], C. Favuzzi[23,24], S. J. Fegan[25], E. C. Ferrara[19], W. B. Focke[1], P. Fortin[25], M. Frailis[43,47], Y. Fukazawa[48],
S. Funk[1], P. Fusco[23,24], F. Gargano[24], D. Gasparrini[32], N. Gehrels[19], S. Germani[4,5], B. Giebels[25], N. Giglietto[23,24],
P. Giommi[32], F. Giordano[23,24], M. Giroletti[49], T. Glanzman[1], G. Godfrey[1], I. A. Grenier[11], M.-H. Grondin[50,51],
J. E. Grove[45], L. Guillemot[52], S. Guiriec[53], M. Gustafsson[14], D. Hadasch[27], Y. Hanabata[48], A. K. Harding[19],
M. Hayashida[1,54], E. Hays[19], A. B. Hill[55], D. Horan[25], X. Hou[56], R. E. Hughes[57], G. Iafrate[12,47], R. Itoh[48],
G. Jóhannesson[58], R. P. Johnson[6], T. E. Johnson[19], A. S. Johnson[1], T. J. Johnson[36,83,84], T. Kamae[1], H. Katagiri[59],
J. Kataoka[60], J. Katsuta[1], N. Kawai[61,62], M. Kerr[1], J. Knödlseder[21,22], D. Kocevski[1], M. Kuss[10], J. Lande[1], D. Landriu[11],
L. Latronico[63], M. Lemoine-Goumard[46,86], A. M. Lionetto[29,30], M. Llena Garde[8,41], F. Longo[12,13], F. Loparco[23,24],
B. Lott[46], M. N. Lovellette[45], P. Lubrano[4,5], G. M. Madejski[1], M. Marelli[17], E. Massaro[64], M. N. Mazziotta[24],
W. McConville[19,20], J. E. McEnery[19,20], J. Mehault[39], P. F. Michelson[1], M. Minuti[10], W. Mitthumsiri[1], T. Mizuno[48],
A. A. Moiseev[20,33], M. Mongelli[24], C. Monte[23,24], M. E. Monzani[1], A. Morselli[29], I. V. Moskalenko[1], S. Murgia[1],
T. Nakamori[60], M. Naumann-Godo[11], J. P. Norris[65], E. Nuss[39], T. Nymark[8,9], M. Ohno[66], T. Ohsugi[67], A. Okumura[1,66],
N. Omodei[1], E. Orlando[1,68], J. F. Ormes[69], M. Ozaki[66], D. Paneque[1,70], J. H. Panetta[1], D. Parent[2,83], J. S. Perkins[19,33,34,71],
M. Pesce-Rollins[10], M. Pierbattista[11], M. Pinchera[10], F. Piron[39], G. Pivato[15], T. A. Porter[1], J. L. Racusin[19],
S. Rainò[23,24], R. Rando[14,15], M. Razzano[6,10], S. Razzaque[2,83], A. Reimer[1,72], O. Reimer[1,72], T. Reposeur[46], S. Ritz[6],
L. S. Rochester[1], R. W. Romani[1], M. Roth[26], R. Rousseau[56], F. Ryde[8,9], H. F.-W. Sadrozinski[6], D. Salvetti[17],
D. A. Sanchez[50], P. M. Saz Parkinson[6], C. Sbarra[14], J. D. Scargle[73], T. L. Schalk[6], C. Sgrò[10], M. S. Shaw[1], C. Shrader[33],
E. J. Siskind[74], D. A. Smith[46], G. Spandre[10], P. Spinelli[23,24], T. E. Stephens[19,75], M. S. Strickman[45],
D. J. Suson[76], H. Tajima[1,77], H. Takahashi[67], T. Takahashi[66], T. Tanaka[1], J. G. Thayer[1], J. B. Thayer[1], D. J. Thompson[19],
L. Tibaldo[14,15], O. Tibolla[78], F. Tinebra[64], M. Tinivella[10], D. F. Torres[27,79], G. Tosti[4,5], E. Troja[19,87], Y. Uchiyama[1],
J. Vandenbroucke[1], A. Van Etten[1], B. Van Klaveren[1], V. Vasileiou[39], G. Vianello[1,80], V. Vitale[29,30], A. P. Waite[1],
E. Wallace[26], P. Wang[1], M. Werner[72], B. L. Winer[57], D. L. Wood[81,83], K. S. Wood[45], M. Wood[1],
Z. Yang[8,41], AND S. Zimmer[8,41]

[1] W. W. Hansen Experimental Physics Laboratory, Kavli Institute for Particle Astrophysics and Cosmology, Department of Physics and
SLAC National Accelerator Laboratory, Stanford University, Stanford, CA 94305, USA; digel@stanford.edu
[2] Center for Earth Observing and Space Research, College of Science, George Mason University, Fairfax, VA 22030, USA
[3] Deutsches Elektronen Synchrotron DESY, D-15738 Zeuthen, Germany
[4] Istituto Nazionale di Fisica Nucleare, Sezione di Perugia, I-06123 Perugia, Italy; Gino.Tosti@pg.infn.it
[5] Dipartimento di Fisica, Università degli Studi di Perugia, I-06123 Perugia, Italy
[6] Santa Cruz Institute for Particle Physics, Department of Physics and Department of Astronomy and Astrophysics,
University of California at Santa Cruz, Santa Cruz, CA 95064, USA
[7] Department of Astronomy, Stockholm University, SE-106 91 Stockholm, Sweden
[8] The Oskar Klein Centre for Cosmoparticle Physics, AlbaNova, SE-106 91 Stockholm, Sweden
[9] Department of Physics, Royal Institute of Technology (KTH), AlbaNova, SE-106 91 Stockholm, Sweden
[10] Istituto Nazionale di Fisica Nucleare, Sezione di Pisa, I-56127 Pisa, Italy
[11] Laboratoire AIM, CEA-IRFU/CNRS/Université Paris Diderot, Service d'Astrophysique, CEA Saclay, 91191 Gif sur Yvette, France; jean.ballet@cea.fr
[12] Istituto Nazionale di Fisica Nucleare, Sezione di Trieste, I-34127 Trieste, Italy
[13] Dipartimento di Fisica, Università di Trieste, I-34127 Trieste, Italy
[14] Istituto Nazionale di Fisica Nucleare, Sezione di Padova, I-35131 Padova, Italy
[15] Dipartimento di Fisica "G. Galilei," Università di Padova, I-35131 Padova, Italy
[16] Dipartimento di Fisica Nucleare e Teorica, Università degli Studi di Pavia, 27100 Pavia, Italy
[17] INAF-Istituto di Astrofisica Spaziale e Fisica Cosmica, I-20133 Milano, Italy
[18] Istituto Universitario di Studi Superiori (IUSS), I-27100 Pavia, Italy
[19] NASA Goddard Space Flight Center, Greenbelt, MD 20771, USA
[20] Department of Physics and Department of Astronomy, University of Maryland, College Park, MD 20742, USA
[21] CNRS, IRAP, F-31028 Toulouse Cedex 4, France
[22] GAHEC, Université de Toulouse, UPS-OMP, IRAP, Toulouse, France
[23] Dipartimento di Fisica "M. Merlin," dell'Università e del Politecnico di Bari, I-70126 Bari, Italy
[24] Istituto Nazionale di Fisica Nucleare, Sezione di Bari, I-70126 Bari, Italy
[25] Laboratoire Leprince-Ringuet, École polytechnique, CNRS/IN2P3, Palaiseau, France
[26] Department of Physics, University of Washington, Seattle, WA 98195-1560, USA; tburnett@u.washington.edu
[27] Institut de Ciències de l'Espai (IEEE-CSIC), Campus UAB, 08193 Barcelona, Spain

[28] INAF-Istituto di Astrofisica Spaziale e Fisica Cosmica, I-00133 Roma, Italy

[29] Istituto Nazionale di Fisica Nucleare, Sezione di Roma "Tor Vergata," I-00133 Roma, Italy

[30] Dipartimento di Fisica, Università di Roma "Tor Vergata," I-00133 Roma, Italy

[31] Experimental Physics Department, University College Dublin, Belfield, Dublin 4, Ireland

[32] Agenzia Spaziale Italiana (ASI) Science Data Center, I-00044 Frascati (Roma), Italy

[33] Center for Research and Exploration in Space Science and Technology (CRESST) and NASA Goddard Space Flight Center, Greenbelt, MD 20771, USA

[34] Department of Physics and Center for Space Sciences and Technology, University of Maryland Baltimore County, Baltimore, MD 21250, USA

[35] Artep Inc., 2922 Excelsior Springs Court, Ellicott City, MD 21042, USA

[36] National Academy of Sciences, Washington, DC 20001, USA

[37] IRFU/SEDI, CEA Saclay, 91191 Gif sur Yvette, France

[38] ASI Science Data Center, I-00044 Frascati (Roma), Italy

[39] Laboratoire Univers et Particules de Montpellier, Université Montpellier 2, CNRS/IN2P3, Montpellier, France

[40] Department of Physics and Astronomy, Sonoma State University, Rohnert Park, CA 94928-3609, USA

[41] Department of Physics, Stockholm University, AlbaNova, SE-106 91 Stockholm, Sweden

[42] IASF Palermo, I-90146 Palermo, Italy

[43] Dipartimento di Fisica, Università di Udine and Istituto Nazionale di Fisica Nucleare, Sezione di Trieste, Gruppo Collegato di Udine, I-33100 Udine, Italy

[44] Stellar Solutions Inc., 250 Cambridge Avenue, Suite 204, Palo Alto, CA 94306, USA

[45] Space Science Division, Naval Research Laboratory, Washington, DC 20375-5352, USA

[46] Centre d'Études Nucléaires de Bordeaux Gradignan, Université Bordeaux 1, CNRS/IN2p3, 33175 Gradignan, France

[47] Osservatorio Astronomico di Trieste, Istituto Nazionale di Astrofisica, I-34143 Trieste, Italy

[48] Department of Physical Sciences, Hiroshima University, Higashi-Hiroshima, Hiroshima 739-8526, Japan

[49] INAF Istituto di Radioastronomia, I-40129 Bologna, Italy

[50] Max-Planck-Institut für Kernphysik, D-69029 Heidelberg, Germany

[51] Landessternwarte, Universität Heidelberg, Königstuhl, D-69117 Heidelberg, Germany

[52] Max-Planck-Institut für Radioastronomie, Auf dem Hügel 69, D-53121 Bonn, Germany

[53] Center for Space Plasma and Aeronomic Research (CSPAR), University of Alabama in Huntsville, Huntsville, AL 35899, USA

[54] Department of Astronomy, Graduate School of Science, Kyoto University, Sakyo-ku, Kyoto 606-8502, Japan

[55] School of Physics and Astronomy, University of Southampton, Highfield, Southampton, SO17 1BJ, UK

[56] Centre d'Études Nucléaires de Bordeaux Gradignan, IN2P3/CNRS, Université Bordeaux 1, BP120, F-33175 Gradignan Cedex, France

[57] Department of Physics, Center for Cosmology and Astro-Particle Physics, The Ohio State University, Columbus, OH 43210, USA

[58] Science Institute, University of Iceland, IS-107 Reykjavik, Iceland

[59] College of Science, Ibaraki University, 2-1-1, Bunkyo, Mito 310-8512, Japan

[60] Research Institute for Science and Engineering, Waseda University, 3-4-1, Okubo, Shinjuku, Tokyo 169-8555, Japan

[61] Department of Physics, Tokyo Institute of Technology, Meguro City, Tokyo 152-8551, Japan

[62] Cosmic Radiation Laboratory, Institute of Physical and Chemical Research (RIKEN), Wako, Saitama 351-0198, Japan

[63] Istituto Nazionale di Fisica Nucleare, Sezioine di Torino, I-10125 Torino, Italy

[64] Physics Department, Università di Roma "La Sapienza," I-00185 Roma, Italy

[65] Department of Physics, Boise State University, Boise, ID 83725, USA

[66] Institute of Space and Astronautical Science, JAXA, 3-1-1 Yoshinodai, Chuo-ku, Sagamihara, Kanagawa 252-5210, Japan

[67] Hiroshima Astrophysical Science Center, Hiroshima University, Higashi-Hiroshima, Hiroshima 739-8526, Japan

[68] Max-Planck Institut für extraterrestrische Physik, D-85748 Garching, Germany

[69] Department of Physics and Astronomy, University of Denver, Denver, CO 80208, USA

[70] Max-Planck-Institut für Physik, D-80805 München, Germany

[71] Harvard-Smithsonian Center for Astrophysics, Cambridge, MA 02138, USA

[72] Institut für Astro- und Teilchenphysik and Institut für Theoretische Physik, Leopold-Franzens-Universität Innsbruck, A-6020 Innsbruck, Austria

[73] Space Sciences Division, NASA Ames Research Center, Moffett Field, CA 94035-1000, USA

[74] NYCB Real-Time Computing Inc., Lattingtown, NY 11560-1025, USA

[75] Wyle Laboratories, El Segundo, CA 90245-5023, USA

[76] Department of Chemistry and Physics, Purdue University Calumet, Hammond, IN 46323-2094, USA

[77] Solar-Terrestrial Environment Laboratory, Nagoya University, Nagoya 464-8601, Japan

[78] Institut für Theoretische Physik and Astrophysik, Universität Würzburg, D-97074 Würzburg, Germany

[79] Institució Catalana de Recerca i Estudis Avançats (ICREA), Barcelona, Spain

[80] Consorzio Interuniversitario per la Fisica Spaziale (CIFS), I-10133 Torino, Italy

[81] Praxis Inc., Alexandria, VA 22303, USA

ABSTRACT

We present the second catalog of high-energy γ-ray sources detected by the Large Area Telescope (LAT), the primary science instrument on the *Fermi Gamma-ray Space Telescope (Fermi)*, derived from data taken during the first 24 months of the science phase of the mission, which began on 2008 August 4. Source detection is based on the average flux over the 24 month period. The second *Fermi*-LAT catalog (2FGL) includes source location regions, defined in terms of elliptical fits to the 95% confidence regions and spectral fits in terms of power-law, exponentially cutoff power-law, or log-normal forms. Also included are flux measurements in five energy bands and light curves on monthly intervals for each source. Twelve sources in the catalog are modeled as spatially extended. We provide a detailed comparison of the results from this catalog with those from the first *Fermi*-LAT catalog (1FGL). Although the diffuse Galactic and isotropic models used in the 2FGL analysis are improved compared to the 1FGL catalog, we attach caution flags to 162 of the sources to indicate possible confusion with residual imperfections in the diffuse model. The 2FGL catalog contains 1873 sources detected and characterized in the 100 MeV to 100 GeV range of which we consider 127 as being firmly identified and 1171 as being reliably associated with counterparts of known or likely γ-ray-producing source classes.

Key words: catalogs – gamma rays: general

Online-only material: color figures, machine-readable tables

1. INTRODUCTION

This paper presents a catalog of high-energy γ-ray sources detected in the first two years of the *Fermi Gamma-ray Space Telescope* mission by the Large Area Telescope (LAT). It is the successor to the LAT Bright Source List (Abdo et al. 2009d) and the first *Fermi*-LAT (1FGL; Abdo et al. 2010f) catalog, which were based on 3 months and 11 months of flight data, respectively. The new catalog represents the deepest-ever catalog in the 100 MeV–100 GeV energy range and includes a number of analysis refinements.

Some important improvements compared to the 1FGL catalog are the following.

1. The 2FGL catalog is based on data from 24 months of observations.
2. The data and instrument response functions (IRFs) use the newer Pass 7 event selections, rather than the Pass 6 event selections used previously.
3. This catalog employs a new, higher-resolution model of the diffuse Galactic and isotropic emissions.
4. Spatially extended sources and sources with spectra other than power laws (PLs) are incorporated into the analysis.
5. The source association process has been refined and expanded.

Owing to the nearly continuous all-sky survey observing mode and large field of view of the LAT, the catalog covers the entire sky with little observational bias. The sensitivity is not uniform, due to the large range of brightness of the foreground diffuse Galactic γ-ray emission. In addition, because the point-spread function (PSF) and effective area of the LAT depend on energy, the sensitivity limit depends markedly on the intrinsic source spectrum.

As has been established with the 1FGL catalog, a number of source populations are known to be present in the data. For individual sources, associations with objects in other astronomical catalogs are evaluated quantitatively.

In Section 2 we describe the LAT and the models for the diffuse backgrounds, celestial, and instrumental. Section 3 describes how the catalog is constructed, with emphasis on what has changed since the analysis for the 1FGL catalog. The 2FGL catalog itself is presented in Section 4, along with a comparison to the 1FGL catalog. We discuss associations and identifications in Section 5. After the conclusions in Section 6 we provide appendices with technical details of the analysis and of the format of the electronic version of the 2FGL catalog.

2. INSTRUMENT AND BACKGROUND

2.1. The Data

The LAT is a γ-ray detector designed to distinguish γ-rays in the energy range 20 MeV to more than 300 GeV from the intense background of energetic charged particles found in the 565 km altitude orbit of the *Fermi* satellite. For each γ-ray, the LAT measures its arrival time, direction, and energy. The effective collecting area is $\sim$6500 cm^2 at 1 GeV (for the Pass 7 event selection used here; see below), the field of view is quite large (>2 sr), and the observing efficiency is very high, limited primarily by interruptions of data taking during the passage of *Fermi* through the South Atlantic Anomaly (SAA; $\sim$13%) and trigger dead time fraction ($\sim$9%). The per-photon angular resolution is strongly dependent on energy; the 68% containment radius is about 0°.8 at 1 GeV (averaged over the acceptance of the LAT) and varies with energy approximately as $E^{-0.8}$, asymptoting at $\sim$0°.2 at high energies. The tracking section of the LAT has 36 layers of silicon strip detectors to record the tracks of charged particles, interleaved with 16 layers of tungsten foil (12 thin layers, 0.03 radiation length, at the top or *Front* of the instrument, followed by 4 thick layers, 0.18 radiation length, in the *Back* section) to promote γ-ray pair conversion. Beneath the tracker is a calorimeter comprised of an eight-layer array of CsI crystals (1.08 radiation length per layer) to determine the γ-ray energy. The tracker is surrounded by segmented charged-particle anticoincidence detectors (plastic scintillators with photomultiplier tubes) to reject cosmic-ray background events. More information about the LAT and the performance of the LAT is presented in Atwood et al. (2009) and the in-flight calibration of the LAT is described in Abdo et al. (2009h) and A. A. Abdo et al. (2012b, in preparation).

The data analyzed here for the 2FGL catalog were taken during the period 2008 August 4 (15:43 UTC)–2010 August 1 (01:17 UTC). During most of this time *Fermi* was operated in sky-scanning survey mode (viewing direction rocking north and south of the zenith on alternate orbits). Time intervals flagged as "bad" (a very small fraction) were excluded. Furthermore, a few minutes were excised around four bright gamma-ray bursts (GRB 080916C: 243216749–243217979, GRB 090510: 263607771–263625987, GRB 090902B: 273582299–273586600, GRB 090926A: 275631598–275632048 in order to avoid having these bright transients distort the analysis of the more persistent catalog sources near these directions[88]). We are preparing a separate catalog of LAT GRBs.

Previous analysis of the *Fermi*-LAT data relied on criteria for selecting probable γ-ray events from all the instrument triggers as determined before launch or modified versions of these selections (called Pass 6_V3 Diffuse[89]). Experience with the data allowed us to develop an improved event selection process with lower instrumental background at energies above 10 GeV and higher effective area at energies below 200 MeV.
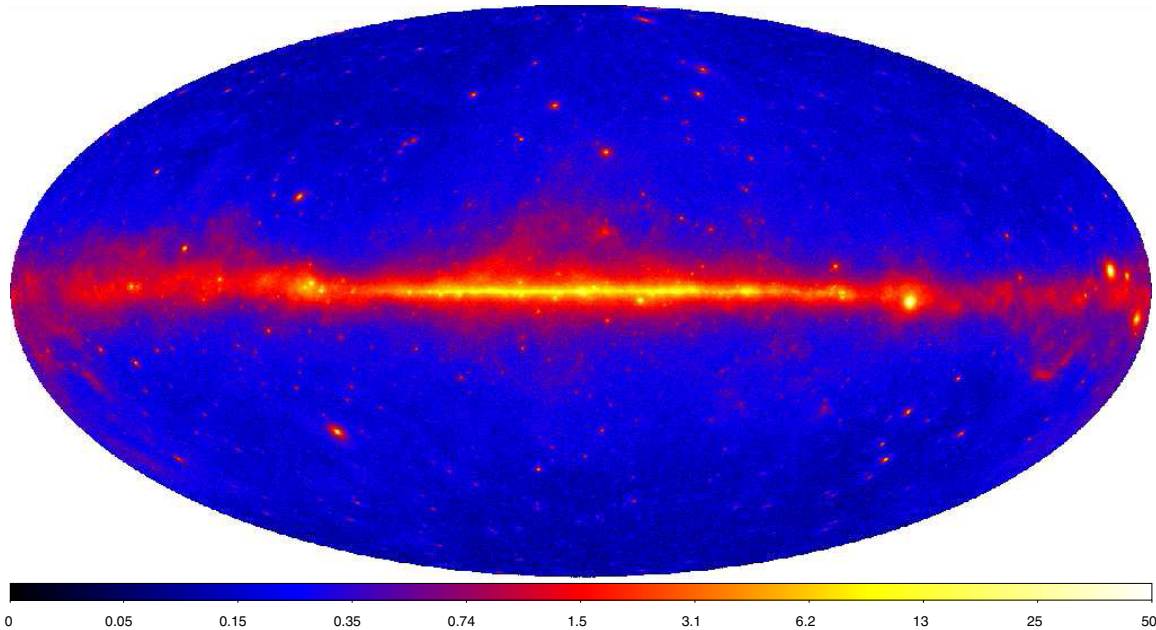
Figure 1. Sky map of the energy flux derived from the LAT data for the time range analyzed in this paper, Aitoff projection in Galactic coordinates. The image shows γ-ray energy flux for energies between 100 MeV and 10 GeV, in units of 10^{-7} erg cm^{-2} s^{-1} sr^{-1}.

These Pass 7_V6 (P7_V6) Source[90] class event selections are accompanied by a corresponding revised set of IRFs (A. A. Abdo et al. 2012b, in preparation), including an energy-dependent PSF calibrated using known celestial point sources. The model for the diffuse gamma-ray background was fit using P7_V6 Clean event selections and IRFs (see Section 2.2). The Clean event selection has lower residual background intensity than P7_V6 Source at the cost of decreased effective area, a tradeoff that is worthwhile for studies of diffuse γ-ray emission. The IRFs tabulate the effective area, PSF, and energy dispersions as functions of energy and inclination angle with respect to the LAT z-axis. The IRFs are also tabulated as a function of the location of the γ-ray conversion in the LAT; *Front* conversions occur in the top 12 tracking layers. The tungsten foils are thinnest in this region and the PSF is narrower than for the *Back* section, which has four layers of relatively thick conversion foils. The 2FGL catalog is therefore derived from a new data set rather than simply an extension of the 1FGL data set.

During the 1FGL time interval (up to 2009 July 4) the standard rocking angle for survey-mode observations was $35°$. During much of 2009 July and August it was set to $39°$. Then on 2009 September 2 the standard rocking angle was increased to $50°$ in order to lower the temperature of the spacecraft batteries and thus extend their lifetime. Time intervals during which the rocking angle of the LAT was greater than $52°$ were excluded. The more conservative 1FGL limit of $43°$ had to be raised to accommodate the larger standard rocking angle.

For the 2FGL analysis we apply a more conservative cut on the zenith angles of the γ-rays, $100°$ instead of the $105°$ used for the 1FGL catalog. This compensates for the increased contamination from atmospheric γ-rays from Earth's limb due to the larger rocking angle. Another motivation for the tighter cut is that the new Pass 7 event selections used for the 2FGL analysis have much greater effective area at low energies than those used for the 1FGL analysis. Because the PSF broadens

with decreasing energy, a more conservative limit on zenith angle is warranted in any case.

The energy flux map of Figure 1 summarizes the data set used for this analysis. The corresponding exposure is relatively uniform, owing to the large field of view and the rocking-scanning pattern of the sky survey. With the new rocking angle set to $50°$ the exposure is minimum at the celestial equator, maximum at the north celestial pole and the contrast (maximum to minimum exposure ratio) is 1.75 (Figure 2). The exposure with rocking angle $35°$ (Figure 2 of Abdo et al. 2009d) was least at the south celestial pole, with a contrast of 1.33. The north/south asymmetry is due to loss of exposure during passages of *Fermi* through the SAA. Figure 3 shows that the original rocking scheme resulted in a very uniform exposure over the sky. The new rocking scheme is less uniform, although it still covers the entire sky to an adequate depth. The exposure map for 2FGL is about halfway between the $35°$ and $50°$ maps. It peaks toward the north celestial pole and is rather uniform over the south celestial hemisphere, with a contrast of 1.37. Note that the average etendue of the telescope is only slightly reduced, from 1.51 m^2 sr (at 1 GeV) in the first 11 months to 1.43 m^2 sr over the last 11 months. The reduction is due to the part of the field of view rejected by the newer zenith angle selection.

2.2. Model for the Diffuse Gamma-Ray Background

The γ-ray emission produced by the Galaxy originating from the interaction of cosmic-ray electrons and protons with interstellar nucleons and photons is modeled with the same method as for the 1FGL catalog. We fit a linear combination of gas column densities, an inverse Compton (IC) intensity map, and isotropic intensity to the LAT data using the P7_V6 Clean data set. To account for the non-uniform cosmic-ray flux in the Galaxy, the gas column densities are distributed within galactocentric annuli. More details on the various radio and infrared surveys used to generate the maps for the different annuli are given at the Web site of the *Fermi* Science Support
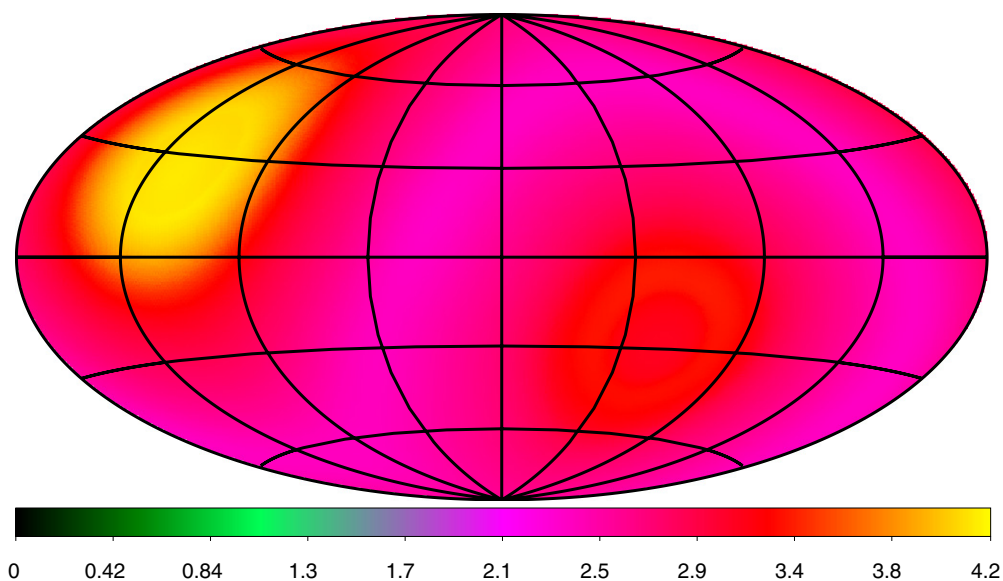
Figure 2. Exposure of the LAT for the period 2009 September to 2010 July when the rocking angle was 50°, Aitoff projection in Galactic coordinates. The units are equivalent on-axis exposure at 1 GeV in Ms.

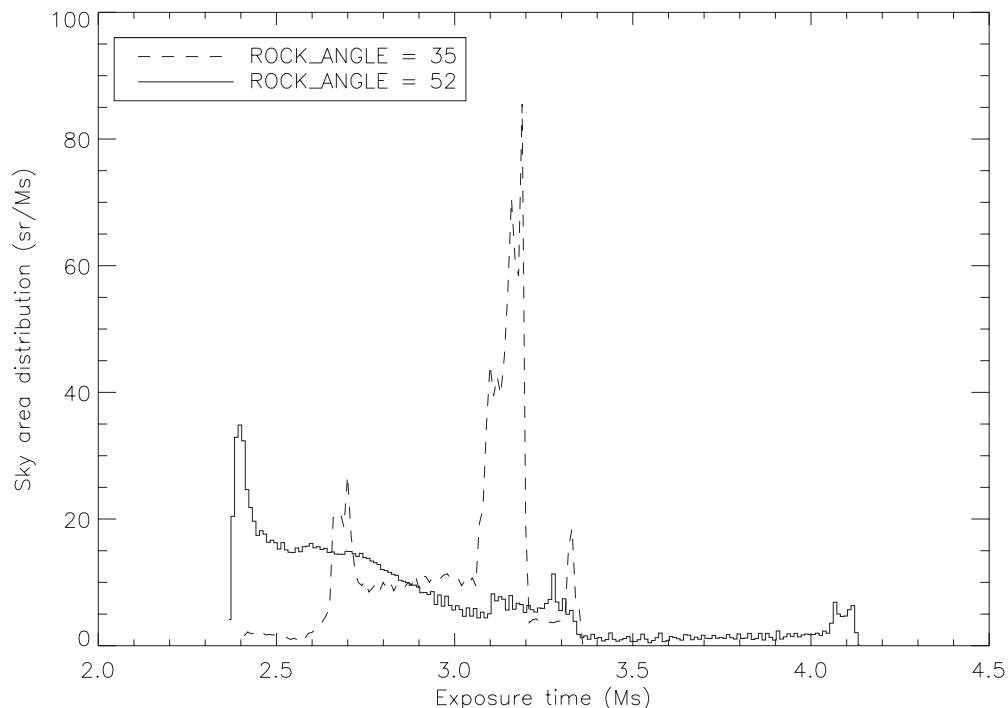(A color version of this figure is available in the online journal.)

Figure 3. Distribution of the equivalent on-axis exposure of the LAT at 1 GeV. The curves show the area of the sky exposed at that depth. The dashed curve is for the first 11 months (1FGL: 2008 August to 2009 June) when the rocking angle was 35°, and the full curve is for the period when the rocking angle was 50° (2009 September to 2010 July, also 11 months).

Center.[91] IC γ-rays from cosmic-ray electrons interacting on optical, infrared, and cosmic microwave background photons are modeled with GALPROP (Strong et al. 2007). In each energy band, the gas emissivities and IC normalization were left free to vary.

For this study we have improved the modeling of the diffuse emission in several ways. With more than twice the γ-ray statistics, we were better able to discriminate between the template maps described above and we were also able to increase the number of energy bins from 10 to 14, spanning

63 MeV to 40 GeV. Below 63 MeV, the combined effects of a low effective area and increased Earth limb contamination owing to the increased breadth of the PSF prevent study of the diffuse emission. Above 40 GeV the statistics are too low to discriminate between the large number of templates that comprise the model. The quality of the determination of the linear coefficients (interpreted as the γ-ray emissivities for the gas) was also improved at high energies by using the P7_V6 Clean data set, which has lower residual charged-particle backgrounds at high energies than P6_V3 Diffuse. For energies below 63 MeV or above 40 GeV, the diffuse emission model was derived by extrapolating the measured emissivities according to

---

[91] http://fermi.gsfc.nasa.gov/ssc/data/access/lat/BackgroundModels.html

Table 1
Additional Components in the Diffuse Emission Model

Designation	Center (l, b)	Approx. Dim. $(l \times b)$	$\Omega/4\pi$	Fraction of Total Intensity	Fraction of Intensity within Patch
First quadrant and inner	$25°, 0°$	$40° \times 30°$	1.9%	1.0%	13.4%
Fourth quadrant	$-35°, 9°$	$40° \times 30°$	2.4%	0.3%	3.8%
Lobe north	$0°, 25°$	$50° \times 40°$	3.9%	0.4%	6.9%
Lobe south	$0°, -30°$	$50° \times 40°$	3.7%	0.4%	14.1%

Notes. Description of the additional components added in the Galactic diffuse model. The centers and extents are in Galactic coordinates. The extents are approximate because the shapes are irregular. Ω is the solid angle. To evaluate the fractional intensities, we integrated the intensity above 130 MeV for the First and Fourth quadrant patches and above 1.6 GeV for the Lobe patches.

a fit of the emissivities in terms of bremsstrahlung and pion decay components.

The spatial resolution of the model was improved from $0°.5$ to $0°.125$, which is the sampling of most of the CO survey (Dame et al. 2001). The higher resolution in the fitting procedure helps discriminate H_2, H I, dark gas, and smoother distributions like IC. For the actual fitting, for computational considerations we sampled the maps with $0°.25$ resolution to derive the emissivities and used the full resolution to reconstruct the model from the deduced emissivities. The final resolution of the model is then $0°.125$. Given sufficient statistics this is crucial to discriminate point-like sources and molecular clouds at the PSF scale.

This procedure revealed regions with photon excesses not correlated with gas or templates defined by observations at other wavelengths. We found what appear to be two distinct origins for the excesses, depending on energy. For both cases we introduce ad hoc "patches" in the diffuse emission model to account for their contributions. The patches are regions of spatially uniform intensity whose shapes reproduce the shape of the excesses. The intensity of the emission associated with each patch is fitted for each energy band together with the other templates. The shapes of the patches were chosen to approximately encompass regions with an excess of photons of the order of 20% compared to the model outside the Galactic plane. Two of the regions have a hard spectrum and are lobe-shaped north and south from the Galactic center. This emission was also observed and studied in detail by Su et al. (2010). Table 1 summarizes the patches and their contributions to the model. Images showing the locations and extents of the patches are available from the *Fermi* Science Support Center at the URL cited above. These regions do not correspond to fluctuations in the diffuse emission model. We do not see large regions where the model exceeds the observed intensity, and we did not need to use "negative" patches. Four main regions were identified in the first and fourth quadrants, and north and south of the Galactic center. We added an extra inner patch to the first quadrant region where the intensity was greater than in the rest of the patch. The spectra of the patches were determined in the same way as for the other templates by extracting their intensities from fits in each energy bin.

At lower energies, below a few GeV, an excess of photons seems to be associated with the giant radio loop Loop I. The North Polar Spur is clearly visible in the LAT data and can be roughly modeled with the 408 MHz radio map of Haslam et al. (1981) as well as a large rounded shape filling the Loop. At low energies distinguishing between γ-rays originating from Loop I and from larger distances is very difficult near the Galactic plane. It is possible that the scaling of the model map for the Galactic IC emission as well as the fitted emissivities of inner Galaxy gas rings are artificially increased in the fitting procedure to

account for γ-rays produced locally. While keeping the overall residual fairly flat, this may bias the diffuse emission spectrum and derived spectra and significances of faint sources in a large region of about 100° wide in longitude and 30° in latitude centered in the Galactic center. Independent of this effect, other regions are probably inadequately modeled, for example, the Cygnus region, the Carina tangent, and the Orion molecular cloud; see Section 3.9.

The spatial grid of the model now has a bin centered at latitude zero. Previously the Galactic ridge was split between two bins with the consequence of flattening the modeled ridge and possibly inducing the detection of spurious sources in the Galactic ridge.

We also created a template for the emission from the Earth limb that is not completely removed from the P7_V6 Source and Clean data sets at energies below 200 MeV. These are γ-rays that are in the broad tails of the PSF and so pass the selection cut on zenith angle (see Section 2.1). For the template we used the residuals in the 50–68 MeV energy range and assumed that the spatial shape is independent of energy. The very soft spectrum was derived by adding this template to the model. The template is specific to the data set analyzed here because the residual Earth limb emission depends on the orientation of the LAT.

The isotropic component was derived for the P7_V6 Source data set by fitting the data for the whole sky using the Galactic diffuse emission modeled as above. By construction the isotropic component includes the contribution of residual (misclassified) cosmic rays for the P7_V6 Source event analysis class. Treating the residual charged particles as effectively an isotropic component of the γ-ray sky brightness rests on the assumption that the acceptance for residual cosmic rays behaves similarly as for γ-rays; in particular we assume that the relative contributions of the *Front* and *Back* events to the isotropic intensity are according to their relative effective areas. This approximation is necessary in the *gtlike* analysis described in Section 3.2. The actual residual background rates for *Front* and *Back* events do not in fact scale precisely with the (γ-ray) effective areas, with the most notable difference being in the low energy range <400 MeV for which the background "leakage" in the *Back* section of the tracker is appreciably greater than for the *Front* section. This has the effect of decreasing the flux measurements at low energies (below ~200 MeV) and hardening the spectra, with the greatest effects for low-significance, soft sources. On average the spectral indices for PL spectral fits are hardened by less than half of the typical uncertainty in the measured spectral index.

The models for the Galactic diffuse emission and the isotropic background spectrum, along with more detailed descriptions of

their derivation, are available from the *Fermi* Science Support Center.

3. CONSTRUCTION OF THE CATALOG

The procedure used to construct the 2FGL catalog has a number of improvements relative to what was done for the 1FGL catalog. In this section we review the procedure, with an emphasis on what is being done differently.

As for the 1FGL catalog, the basic analysis steps are source detection, localization (position refinement), and significance estimation. Once the final source list was determined, by applying a significance threshold, we evaluated the flux in five bands and the flux history (light curve of the integrated flux) for each source.

Also as for the 1FGL analysis, the source detection step was applied only to the data from the full 24 month time interval of the data set. We did not search for transient sources that may have been bright for only a small fraction of the two-year interval. See Section 5.2.11 for a discussion of transient LAT sources reported in Astronomer's Telegrams. Analysis of 2FGL catalog source variability is found in Section 3.6.

The 2FGL catalog is primarily a catalog of point (spatially unresolved) sources detected by the LAT in the 24 month interval. As discussed below, the analysis and catalog also include a number of LAT sources that are known to be spatially extended. These sources are defined specially in the analysis (see Section 3.4) but are considered members of the 2FGL catalog.

3.1. Detection and Localization

Detection of point sources involves iterating through three steps: (1) identification of potential point sources, denoted as "seeds," that have not already been selected in a previous iteration; (2) a full all-sky optimization of a model of the γ-ray sky (diffuse emission plus sources) including the new seeds to refine their estimated positions and evaluate their significances; and (3) creation of a "residual test statistic (TS) map." The TS is evaluated as TS $= 2(\log \mathcal{L}(\text{source}) - \log \mathcal{L}(\text{nosource}))$, where $\mathcal{L}$ represents the likelihood of the data given the model with or without a source present at a given position on the sky. In each case the likelihood is assumed to have been maximized with respect to the adjustable parameters of the model (Mattox et al. 1996).

We performed this analysis using the *pointlike* analysis system, for which the data are partitioned by whether the conversion occurred in the *Front* or *Back* sections of the tracker and binned in energy with four bins per decade from 100 MeV to 316 GeV. For each such partition, or band, the γ-rays are partitioned according to their HEALPix (Górski et al. 2005) indices, with the N_{side} parameter chosen such that the angular size of the partition is small compared with the PSF for that energy and conversion position. Detailed simulations, analytic studies, and adjustments of the bin size have shown that this does not lose precision compared with a fully unbinned procedure.

We discuss each step of the iteration in turn.

3.1.1. Determination of Seeds

We started with an initial model comprised of the 1FGL catalog of sources to which we added seeds from the wavelet-based methods, *mr_filter* (Starck & Pierre 1998) and *PGWave* (Damiani et al. 1997; Ciprini et al. 2007), and a minimal spanning tree-based algorithm (Campana et al. 2008) as described in 1FGL. For the 2FGL catalog analysis, we also included in the

model 12 spatially extended sources that have been detected by the LAT; see Section 3.4. In subsequent iterations, seeds may be added by the examination of the residual TS map, described below. Since source detection is an integral part of the iteration procedure, the efficiency of the initial seed-determination procedures is not critical.

3.1.2. All-sky Optimization

We define 1728 circular regions centered on points defined by a HEALPix tessellation with $N_{\text{side}} = 12$. All γ-ray data within a $5°$ radius of each of the points are fit to a model including the diffuse components described in Section 2.2 and all seeds within a radius of $10°$. Each region was optimized independently. The parameters included the normalization of each diffuse component and the spectral parameters of the point sources lying inside the boundaries of the HEALPix pixel that defined the region. Since neighboring regions are coupled, sharing data and sources, we repeated this step until the likelihoods were jointly optimized. For some regions along the Galactic plane, convergence required up to 10 iterations.

For point sources identified as pulsars by LAT phase analysis (A. A. Abdo et al. 2012c, in preparation; Abdo et al. 2010s), the spectra were fit to a PL with an exponential cutoff; others were fitted to either a simple PL or log-normal (also called log-parabola); the latter was used if it substantially improved the overall likelihood. These functions are described in Section 3.3. Each seed was characterized by two versions of the likelihood TS (Mattox et al. 1996): one measuring the spectral-shape independent measure from independent fits of the fluxes in each energy band (TS$_{\text{band}}$), and another which is the result of a fit to the spectral model (TS$_{\text{model}}$). The former always will be larger than the latter: the difference is used to decide to switch from a PL to a log-parabola spectral shape. Seeds with TS$_{\text{band}} < 10$ are eliminated from further analysis. The rest are retained in the model for the *pointlike* optimization. After the optimization was complete, those with TS$_{\text{model}} > 10$ were passed on to the *gtlike* step described below, with the *pointlike* fit as a starting point.

3.1.3. Residual T S Map

After the analysis in the previous step converged, we performed a special analysis of the full sky to search for missing point sources. A HEALPix tessellation with $N_{\text{side}} = 512$ is used to define 3.1M points on a $0°.1$ grid. For each point, we added a new point source with a PL spectrum and fixed spectral index 2.0, to the model, and the likelihood was maximized as a function only of its flux. The resulting array of values of TS is plotted as a sky map.

Clusters were defined by proximity: a cluster is the set of all pixels that occupy adjacent positions. The analysis generated a list of all clusters of such pixels with TS > 10 on the map, used as seeds to be added for the next iteration of the all-sky analysis. We estimated the position of a presumed source from the centroid of the pixels, weighted by TS; this position was refined later if the seed survived the full analysis. Adding seeds from the map was done automatically for Galactic latitudes above $5°$; along the Galactic plane the data are not always well represented by either point sources or the model for diffuse Galactic emission, and we introduced new point sources only if they appeared to be well isolated under visual inspection. Figure 4 shows the final such map for a region along the Galactic ridge.

In total, 3499 candidate sources were passed to the significance and thresholding step of the analysis.
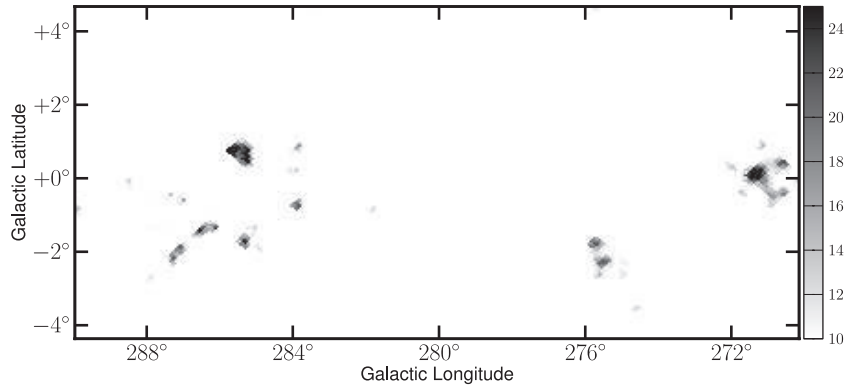
Figure 4. Representative map of the TS residuals along the Galactic ridge, corresponding to the final iteration. There are several clusters that could have generated seeds, but did not appear to be isolated point sources under visual inspection.

3.1.4. Localization

The processing that created the residual TS map used for source detection also performed local optimizations of the likelihood with respect to the position of each point source, using the spectral-shape independent definition of the likelihood, TS_{band}, described above, with the rest of the model fixed. The positional uncertainty for each source was estimated by examining the shape of the log likelihood function, fitting the distribution to the expected quadratic form in the angular deviations from the best-fit position. A measure of the quality of this fit is the mean square deviation of the log likelihood with respect to the fit on a circle of radius corresponding to two standard deviations. For the catalog we tabulated the elliptical parameters including the fit position and the fit quality. As in the case of the 1FGL catalog, we made two empirical corrections based on comparison with the known locations of high-confidence associated sources: multiplied by a 1.1 scale factor, and added $0°.005$ in quadrature to the 95% ellipse axes. This latter is comparable to the spacecraft alignment precision requirement of $10''$.

We searched for systematic biases in source positions, using comparisons with counterpart positions (Section 5). Two cases were considered: (1) sources near the Galactic plane, the positions of which might have been suspected to be biased by the strong gradient of the intensity of the Galactic diffuse emission and (2) weak sources near much stronger ones. We did not find significant biases in either case. In addition, in Appendix A we show that the sizes of the localization regions for weak sources are consistent with expectations, as is the weak dependence on the source spectrum.

3.2. Significance and Thresholding

To evaluate the fluxes and spectral parameters, and also significances, for the catalog we use the standard LAT analysis tool *gtlike* and associated LAT Science Tools[92] (version v9r23p0). The localization procedure (Section 3.1.4) provides spectra and significances as well, but we do not have as much experience with it so we prefer relying on the standard tools whenever possible. This stage of the analysis is similar in principle to what was done for the 1FGL catalog (Abdo et al. 2010f). It splits the sky into Regions of Interest (RoI) in order to make the log $\mathcal{L}$ (where $\mathcal{L}$ is the likelihood function) maximization tractable, varying typically half a dozen sources near the center of the RoI at the same time. (There were 933 RoIs for 2FGL.) This requires an

iterative scheme in order to inject the spectra of all sources in the outer parts of the RoI. It uses the same energy range (100 MeV to 100 GeV) and adjusts the source spectra with positions fixed to the result of Section 3.1.4. The same parameters are used to refit the diffuse emission model (described in Section 2.2) to each RoI: normalization and small corrective slope of the Galactic component and normalization of the isotropic component. We define the test statistic $TS = 2\Delta \log \mathcal{L}$ for quantifying how significantly a source emerges from the background. The iteration scheme was also identical, as well as the threshold at $TS > 25$ applied to all sources, corresponding to a significance of just over 4σ evaluated from the χ^2 distribution with 4 degrees of freedom (position and spectral parameters; Mattox et al. 1996). We note that we require the predicted number of events from a source to be at least 10 over the full energy range, rejecting clusters of a few high-energy events without any low-energy counterpart. The same constraint was enforced for the 1FGL analysis.

The analysis does have a number of important differences with respect to 1FGL.

1. The major change is that we switched from unbinned to binned likelihood (while still using *gtlike* or more precisely the *pyLikelihood* library in the Science Tools). The first reason for the change was to cap the computing time (which increases linearly with observing time in unbinned likelihood). The other important reason is that we discovered with simulations that the scale factors for the diffuse emission model terms returned by unbinned likelihood were significantly biased (overestimating the Galactic diffuse or isotropic diffuse intensity, whichever component was subdominant) whereas those returned by binned likelihood were not. In order to treat the *Front* and *Back* events in the analysis according to their separate PSFs we added the log $\mathcal{L}$ computed separately for *Front* and *Back* events. The energy binning was set to 10 bins per decade. RoIs are square for binned likelihood. We used the ARC projection with pixel size set to $0°.1$ for *Front* and $0°.2$ for *Back* events, in keeping with the high-energy PSF for each category. The sides of the RoIs were defined by adding $7°$ on each side to the diameter of the central part where all source parameters are free. We note that the binned likelihood scheme is more conservative: in simulations comparable to the catalog depth (with or without sources) the significances of detections with unbinned likelihood tended to be around 1σ greater. This has important consequences for the number of sources in 2FGL (see Section 4.2).

---

[92] See http://fermi.gsfc.nasa.gov/ssc/data/analysis/documentation/Cicerone/

2. We took advantage of the fact that the localization procedure (Section 3.1.4) also provides a spectral fit to all sources. We used it as the starting point for the procedure using *gtlike*, rather than starting with all sources set to 0.

3. We did not use exactly the result of the previous iteration to start the next one, but applied a damping factor δ (set to 0.1) to all parameters, defining the next starting point as $P_{n+1} = (1 - \delta)P_n + \delta P_{n-1}$. It is a significant change because in all RoIs the number of sources (outside the core of the RoI) which are considered but frozen is much larger than that of free sources. The damping procedure avoids overshooting and improves convergence.

4. Many bright sources are fitted with curved spectra instead of PL. This is described in Section 3.3. In addition to providing more detailed descriptions of those bright sources, it also improves the reliability of the procedure for neighboring sources. The reason is that it greatly reduces the spectral residuals, which otherwise might have been picked up by neighboring sources. That kind of transfer can be an issue at low energy where the PSF is very broad and cross-talk between sources in the likelihood analysis is strong.

5. We introduce the Earth limb component obtained in Section 2.2, without any adjustment or free parameter in the likelihood analysis.

Appendix B illustrates how well the full model (diffuse emission and individual sources) reproduces the γ-ray sky.

3.3. Spectral Shapes

The 1FGL catalog considered only PL spectra. This was simple and homogeneous, but not a good spectral representation of the bright sources, as could be easily seen from comparing the PL fits with the fluxes in bands (quantified by the Curvature_Index column in Abdo et al. 2010f). As the exposure accumulated, the discrepancies grew statistically larger to the point where it could affect the global fit in an RoI, altering the spectra of neighboring sources in order to get a better overall spectral fit. For two years of data we had to allow for spectra that deviate from PLs. However, increasing the number of free parameters means finding the true best fit is more difficult, so we chose spectral shapes with only one additional free parameter.

For the pulsars we chose exponentially cutoff PLs (hereafter PLExpCutoff), which are a good representation of pulsar spectra in general (Abdo et al. 2010s):

$$\frac{dN}{dE} = K \left(\frac{E}{E_0} \right)^{-\Gamma} \exp \left(-\frac{E - E_0}{E_c} \right). \qquad (1)$$

This is just the product of PL and an exponential. The parameters are K, Γ (as in the PL), and the cutoff energy E_c. E_0 is a reference energy that we are free to choose for each source. The value of E_0 started at 1 GeV but evolved separately for each source at each iteration as described below. All the known γ-ray pulsars with significant LAT pulsations were fitted with the PLExpCutoff representation.

Other bright sources (mainly active galactic nuclei, AGNs) are also not very well represented by PL spectra. Analysis of the bright blazars (Abdo et al. 2010q) indicated that a broken PL was the best spectral representation. This however would add two free parameters and therefore was not stable enough for moderately bright sources. We adopted instead a log-normal representation (that we call LogParabola) which adds only one parameter while decreasing more smoothly at high energy than

the PLExpCutoff form:

$$\frac{dN}{dE} = K \left(\frac{E}{E_0} \right)^{-\alpha - \beta \log(E/E_0)}. \qquad (2)$$

The parameters are K, α (spectral slope at E_0), and the curvature β, and E_0 is an arbitrary reference energy that evolves for each source along the iterations. Negative β (spectra curved upward) were allowed, although we did not get any.

In order to limit the number of free parameters, we did not fit every non-pulsar source as LogParabola, but only those in which the curvature was significant. In a procedure similar to that applied in the all-sky optimization for the source detection step (Section 3.1.2), we assessed that significance for a given source by $TS_{curve} = 2(\log \mathcal{L}(\text{LogParabola}) - \log \mathcal{L}(\text{PL}))$, where $\mathcal{L}$ represents the likelihood function, changing only the spectral representation of that source and refitting all free parameters in the RoI. Since PL is a special case of LogParabola ($\beta = 0$) and $\beta = 0$ is inside the allowed interval we expect that TS_{curve} is distributed as χ^2 with 1 degree of freedom. We switched to LogParabola if $TS_{curve} > 16$, corresponding to 4σ significance for the curvature. All PL sources were tested after each iteration, and we checked at the last iteration that TS_{curve} for LogParabola sources was still > 16 (if it was not, the source was downgraded to PL and the RoI was refit). TS_{curve} was computed for the LAT pulsars as well, but they were not downgraded to PL if $TS_{curve} < 16$.

The extended sources (Section 3.4) were handled on a case by case basis and fitted with either PLExpCutoff, LogParabola, or PL.

The pivot energy E_p (reported as `Pivot_Energy`) was computed as the energy at which the relative uncertainty on the differential flux K was minimal. This was done in the parabolic approximation using the covariance matrix between parameters. To improve the validity of the parabolic approximation, we changed the reference energy E_0 used for fitting to E_p after each iteration (with the same damping procedure as in Section 3.2). This ensured that at the end E_0 was close enough to E_p. The value of α (for LogParabola) depends on the reference energy, $\alpha(E_p) = \alpha(E_0) + 2\beta \log(E_p/E_0)$. The uncertainties on K and α at E_p were derived from the covariance matrix on the actual fitted parameters (relative to E_0). The other parameters do not depend on the choice of E_0.

In the catalog the differential flux K is reported as `Flux_Density` at the reference energy $E_0 = E_p$ (where it is best determined). The low-energy spectral index Γ (for PLExpCutoff) or the spectral slope $\alpha(E_p)$ (for LogParabola) is reported as Spectral_Index. The cutoff energy E_c is reported as `Cutoff`. The curvature β is reported as `beta`. For consistency with 1FGL and in order to allow statistical comparisons between the PL sources and the curved ones, we also report the spectral index of the best PL fit as `PowerLaw_Index` for all sources.

The fitted curvatures β sometimes tended to a large value, corresponding to very peaked spectra. There were cases (for example, suspected millisecond pulsars) when this kind of spectrum could be real. However, this occurred particularly in densely populated regions of the Galactic ridge, where the PSFs overlap and cross-talk between sources in the likelihood analysis is large at low energy. Even though one highly curved spectrum could lead to a better global fit for the RoI, it was not necessarily robust for that particular source, and in many cases we noted that the band fluxes (Section 3.5) did not agree with the very curved fits. In order to avoid extreme cases, we enforced the condition $\beta < 1$, corresponding to changing spectral slope by

2 log 10 = 4.6 over one decade. Whenever β reached 1 for a particular source, we fixed it to 1 and refitted in order to have a reasonable estimate of the errors on the other parameters. Sixty-four sources affected by this are flagged (see Section 3.10 for a description of the flags used in the catalog). A similar difficulty occurred for three faint pulsars in which the low-energy index Γ tended to be very hard. We limited the values to $\Gamma > 0$ and refitted with Γ fixed to 0 when it was reached. Those three pulsars were flagged in the same way. Note that fixing one parameter tends to result in underestimating the errors on the photon and energy fluxes of those sources.

3.4. Extended Sources

In the analysis for the 1FGL catalog it became clear that a small number of sources were not properly modeled by a point source, leading to multiple detections being associated with the same source, e.g., the Large Magellanic Cloud (LMC). For the present analysis, 12 sources that have been shown to be extended in the LAT data were included as extended sources. The spatial templates were based on dedicated analysis of each source region and have been normalized to contain the entire flux from the source (>99% of the flux for unlimited spatial distributions such as two-dimensional Gaussians, 2DG). The spectral form chosen for each source is the closest of those used in the catalog analysis (see Section 3.3) to the spectrum determined by the dedicated analysis.[93]

The extended sources include seven supernova remnants (SNRs), two pulsar wind nebulae (PWNe), the LMC and the Small Magellanic Cloud (SMC), and the radio galaxy Centaurus A. Notes of interest for each source are provided below.

1. *SMC (2DG, PLExpCutoff)*. We modeled the SMC using a 2DG function with a width $\sigma = 0°.9$. While this is the best-fitting simple geometric model, the morphology of the emission may be more complex (Abdo et al. 2010d).

2. *LMC (2 × 2DG, PLExpCutoff)*. This complex region, which accounted for five point sources in the 1FGL catalog, has been modeled as a combination of two 2DG profiles using the parameters specified in Table 3 of Abdo et al. (2010p). The first, with a width of $\sigma = 1°.2$, represents emission from the entire galaxy. The second, with a width of $\sigma = 0°.2$, corresponds to the γ-ray bright region near 30 Doradus. Although this model provides a reasonable first-order description of the γ-ray emission seen from the LMC, it is clear that this composite geometric model is not sufficient to fully describe the complex morphology of the source (Abdo et al. 2010p). There are five sources in the 2FGL catalog that may be due to excess LMC emission after the fit, though two have blazar associations.

3. *IC 443 (2DG, LogParabola)*. This SNR is modeled by a 2DG profile with a width of $\sigma = 0°.26$. The log-parabola spectral form most closely matches the spectrum found for this source in the dedicated analysis (Abdo et al. 2010o).

4. *Vela X (Disk, PL)*. We modeled Vela X using a simple disk with radius $r = 0°.88$ and a PL spectral form (Abdo et al. 2010k). Since the Vela pulsar is spatially coincident with the Vela X PWN and significantly brighter, the detailed analysis was performed using the off-pulse events. For the catalog analysis it was necessary to fix the spectral parameters for the PL to the values determined by the off-pulse analysis.

5. *Centaurus A (Map, PL)*. This large radio galaxy has γ-ray-emitting lobes that extend $\sim 10°$ across the sky. The template used for this source originated from the 22 GHz *Wilkinson Microwave Anisotropy Probe* image, and excludes a $1°$ region around the core (Abdo et al. 2010e), which is modeled separately as a point source in the catalog. The lobes are clearly resolved in the LAT.

6. *MSH 15−52 (Disk, PL)*. This PWN is spatially coincident with the bright γ-ray pulsar PSR B1509−58. The PWN was detected above 1 GeV, while the pulsar was detected only below 1 GeV by the LAT. We were able to investigate the PWN emission using events from all pulsar phases by excluding data below 1 GeV. That analysis showed that a uniform disk with radius $r = 0°.249$ best fits the LAT data (Abdo et al. 2010c). As with Vela X, the PL spectral parameters for this source were fixed during the catalog analysis.

7. *W28 (Disk, LogParabola)*. For W28, only the northern source at (R.A., decl.) = $(270°.34, −23°.44)$ showed evidence for extension. We modeled this source using a disk with radius $r = 0°.39$, the best-fit spatial model found by detailed analysis (Abdo et al. 2010j). As with IC 443, a log-parabola spectral form fits the LAT data best.

8. *W30 (Disk, LogParabola)*. The model for W30 uses a simple disk template centered at (R.A., decl.) = $(271°.40, −21°.63)$ with a radius $r = 0°.37$. For the catalog analysis, a log-parabola spectral model best fits the source spectrum.

9. *HESS J1825−137 (2DG, PL)*. This SNR is modeled with a 2DG profile with a width of $\sigma = 0°.56$, which we found fit the source emission better than a disk. We tested a PL spectrum both with and without an exponential cutoff and found that the data were best fit by a simple PL (Grondin et al. 2011).

10. *W44 (Ring, LogParabola)*. The template for the W44 SNR is an elliptical ring with axes $(a, b)_{inner} = 0°.22, 0°.14$, $(a, b)_{outer} = 0°.30, 0°.19$, and a position angle $\theta = 146°$ counterclockwise from north (Abdo et al. 2010n). Again, the best spectral model for the SNR is a log-parabola.

11. *W51C (Disk, LogParabola)*. W51C is well represented by an elliptical disk with axes $(a, b) = 0°.40, 0°.25$ and a position angle $\theta = 0°$ (Abdo et al. 2009b), using a log-parabola spectral form.

12. *Cygnus Loop (Ring, PLExpCutoff)*. This relatively large SNR accounted for four sources in the 1FGL catalog. It is best represented by a ring located at (R.A., decl.) = $(312°.75, 30°.85)$ with an outer radius of $r_{outer} = 1°.6$ and an inner radius of $r_{inner} = 0°.7$ (Katagiri et al. 2011).

Table 2 lists the source name, the spatial template description, the spectral form, and the reference for the dedicated analysis, where available. In the 2FGL catalog these sources are tabulated with the point sources, with the only distinction being that no position uncertainties are reported (see Section 3.1.4).

3.5. Flux Determination

The source photon fluxes are reported in the 2FGL catalog in the same five energy bands (100–300 MeV; 300 MeV to 1 GeV; 1–3 GeV; 3–10 GeV; 10–100 GeV) as in 1FGL. The fluxes were obtained by freezing the spectral index to that obtained in the fit over the full range and adjusting the normalization in each spectral band. For the curved spectra (Section 3.3) the spectral index in a band was set to the local spectral slope at the logarithmic mid-point of the band $\sqrt{E_n E_{n+1}}$, restricted to be in

---

[93] The templates and spectral models will be made available through the *Fermi* Science Support Center. See Appendix C.

Table 2
Extended Sources used in the 2FGL Analysis

2FGL Name	Extended Source	Spatial Form	Spectral Form	Reference
2FGL J0059.0−7242e	SMC	2D Gaussian	Exp cutoff PL	Abdo et al. (2010d)
2FGL J0526.6−6825e	LMC	2D Gaussian[a]	Exp cutoff PL	Abdo et al. (2010p)
2FGL J0617.2+2234e	IC 443	2D Gaussian	Log Parabola	Abdo et al. (2010o)
2FGL J0833.1−4511e	Vela X	Disk	Power law	Abdo et al. (2010k)
2FGL J1324.0−4330e	Centaurus A (lobes)	Contour map	Power law	Abdo et al. (2010e)
2FGL J1514.0−5915e	MSH 15−52	Disk	Power law	Abdo et al. (2010c)
2FGL J1801.3−2326e	W28	Disk	Log Parabola	Abdo et al. (2010j)
2FGL J1805.6−2136e	W30	Disk	Log Parabola	· · ·
2FGL J1824.5−1351e	HESS J1825−137	2D Gaussian	Power law	Grondin et al. (2011)
2FGL J1855.9+0121e	W44	Ring	Log Parabola	Abdo et al. (2010n)
2FGL J1923.2+1408e	W51C	Disk	Log Parabola	Abdo et al. (2009b)
2FGL J2051.0+3040e	Cygnus Loop	Ring	Exp cutoff PL	Katagiri et al. (2011)

Notes. Twelve 2FGL sources that have been modeled as extended sources. More detail regarding the parameters used in the analysis can be found in the text. The publications describing the detailed analysis for W30 are still in preparation.
[a] To fit the LMC we used a combination of two 2D Gaussian spatial templates.

the interval [0,5]. We used binned likelihood in all bands, but contrary to Section 3.2 we did not distinguish *Front* and *Back* events. The pixel sizes in each band were 0°.3, 0°.2, 0°.15, 0°.1, and 0°.1 decreasing in size with energy as the PSF improves.

The procedure for reporting either a measurement or an upper limit is the same as for the 1FGL catalog. For bands where the source was too weak to be detected, those with TS in the band $TS_i < 10$ or relative uncertainty on the flux $\Delta F_i/F_i > 0.5$, 2σ upper limits were calculated, F_i^{UL}. Two methods were used, the *profile* and *Bayesian* methods. In the first (Rolke et al. 2005), which is used when $1 < TS < 10$, the profile likelihood function, $\log \mathcal{L}(F_i)$, is assumed to be distributed as $\chi^2/2$ and the upper limit corresponds to the point where $\log \mathcal{L}(F_i)$ decreases by 2 from its maximum value. In the Bayesian method (Helene 1983), which is used when $TS < 1$, the limit is found by integrating $\mathcal{L}(F_i)$ from 0 up to the flux that encompasses 95% of the posterior probability. With the probability chosen in this way the upper limits calculated with each method are similar for sources with $TS = 1$. The 2σ upper limit is then reported in the flux column and the uncertainty is set to 0.

In the 1FGL catalog the photon flux between 1 and 100 GeV and the energy flux between 100 MeV and 100 GeV (F_{35} and S_{25} in Table 5; Abdo et al. 2010f) were estimated from the sum of band fluxes because the result of the fit over the full band was biased by the PL approximation and was inconsistent with the sum of band fluxes for the bright sources. In the 2FGL catalog analysis the curved spectral shapes are precise enough to overcome that limitation (Figure 5). The main advantage of the full spectral fit is that it is statistically more precise because it incorporates the (reasonable) constraint that the spectral shape should be smoothly varying with energy. Even using the newer data set (with larger effective area at low energy), the relative uncertainties in the lower energy bands tend to be very large. The relative uncertainty on the full photon flux between 100 MeV and 100 GeV (F_{25}, dominated by low energy) is much larger than that on F_{35} or S_{25} (23% versus 15% and 14%, respectively, for a $TS = 100$ source with spectral index 2.2) and strongly depends on spectral index (whereas that on F_{35} does not). So, we do not report the photon flux over the full band in 2FGL. We report F_{35} and S_{25}, as in 1FGL, but estimated from the fit over the full band. For comparison, the relative uncertainties on estimates of F_{35} and S_{25} from the sum of bands (as in 1FGL) are 20% for the same typical source. The procedure for reporting upper limits described above applies to F_{35} and S_{25} as well.
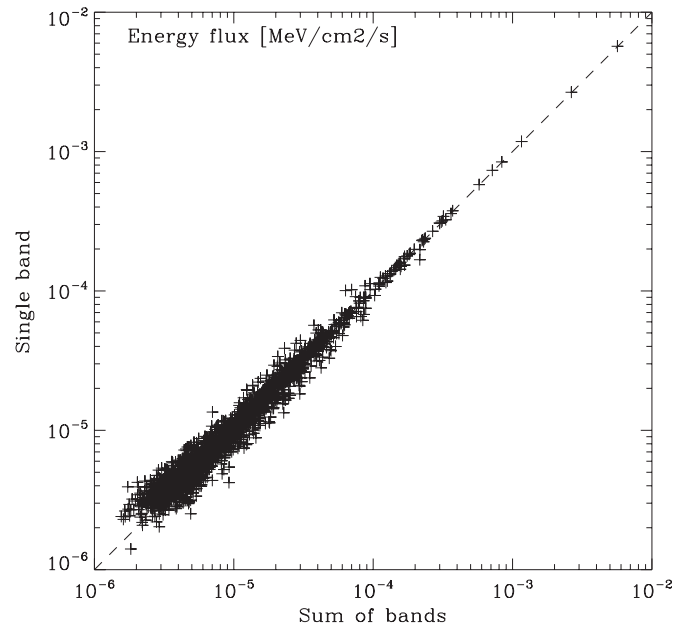

Figure 5. Comparison of estimates of the energy flux from 100 MeV to 100 GeV S_{25} from the sum of bands (abscissa) and the fit to the full band (ordinate). No obvious bias can be observed.

Five sources (four very hard and one very soft) have relative uncertainty on F_{35} larger than 0.5. The faintest of those five also has relative uncertainty on S_{25} larger than 0.5.

We show the photon and energy flux distributions for the 2FGL sources in two different ways in Figures 6 and 7. Figure 7 shows that the range of energy fluxes among the 2FGL sources is greater than three decades. Figure 20 of Abdo et al. (2010f) was the same plot as in Figure 6 but on the photon flux between 100 MeV and 100 GeV. The detection threshold on the photon flux over the full band depends sensitively on the spectral index of the source. Building a flux-limited sample on that quantity required raising the minimum flux to the detection threshold for soft sources and resulted in discarding most of the hard sources. The photon flux above 1 GeV (or the energy flux), which we show in these figures, is more appropriate to build a flux-limited sample because it discards few sources.

Figures 8–10 show examples of the band fluxes, with the best fit over the full range overlaid. From this kind of plot
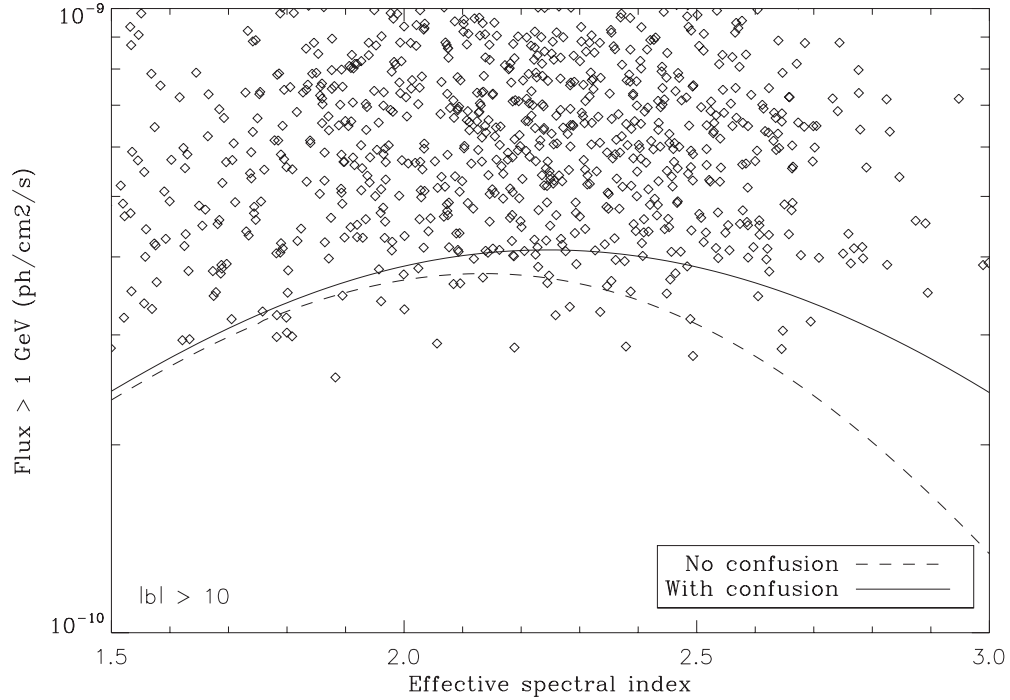
Figure 6. Distribution of sources in 2FGL excluding the Galactic plane in the spectral index–photon flux plane. The spectral index is the effective PowerLaw_Index (power-law fit even for curved sources). The photon flux is between 1 and 100 GeV (F_{35}). The low flux threshold is quite sharp around 4×10^{-10} photons cm^{-2} s^{-1}. The full line shows the expected threshold following App. A of Abdo et al. (2010f) accounting for the average confusion, and the dashed line for an isolated source.
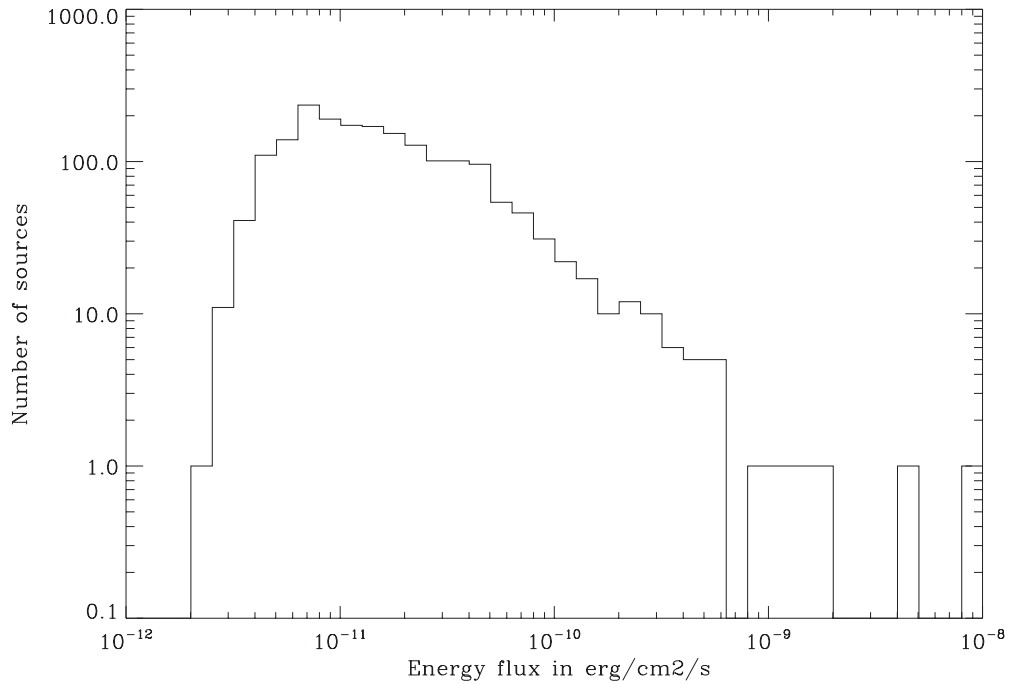

Figure 7. Distribution of all sources in 2FGL with respect to log(Energy flux). The low flux threshold is quite sharp around 5×10^{-12} erg cm^{-2} s^{-1}, indicating that the TS cut that is applied is not too far from a cut on the energy flux S_{25} over the full band (100 MeV to 100 GeV).

one may build a spectral fit quality indicator similar to the Curvature_Index of 1FGL:

$$C_{\text{syst}} = \sum_i \frac{\left(F_i - F_i^{\text{fit}}\right)^2}{\sigma_i^2 + \left(f_i^{\text{rel}} F_i^{\text{fit}}\right)^2}, \qquad (3)$$

where i runs over all bands and F_i^{fit} is the flux predicted in that band from the spectral fit to the full band. f_i^{rel} reflects the systematic uncertainty on effective area (Section 3.7). They

were set to 0.1, 0.05, 0.05, 0.08, and 0.1 in our five bands. Since, in 2FGL, curvature is accounted for in the spectral shape, the interpretation of that quantity is now whether the proposed spectral shape agrees well with the band fluxes or not. We did not report that in the table, but we set a flag (Flag 10 of Table 3) whenever $C_{\text{syst}} > 16.3$, corresponding to a probability of 10^{-3} assuming a χ^2 distribution with 3 degrees of freedom (5–2, since the majority of sources are fitted with PL spectra which have two free parameters). Thirty-three sources are flagged in this way,
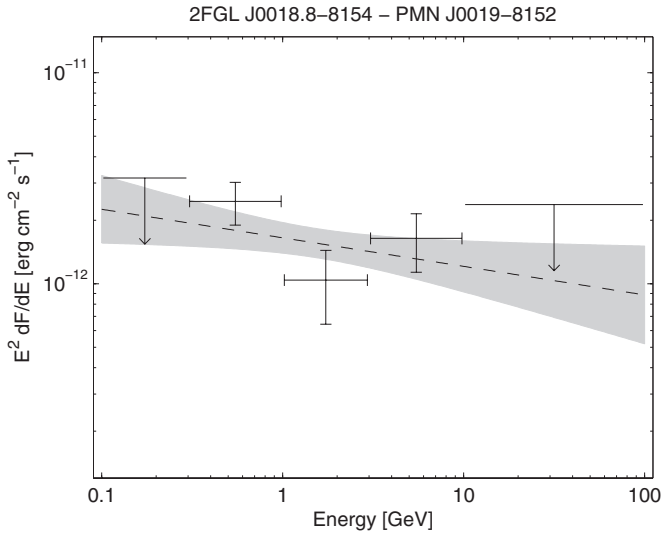
2FGL J0018.8–8154 – PMN J0019–8152

Figure 8. Spectrum of a faint AGN, as an example of a power-law spectrum. The fit over the full band (dashed line) is overlaid over the five band fluxes converted to νF_ν units. The gray shaded area (butterfly) shows the formal 1σ statistical error on log(differential flux) as a function of energy, obtained using the covariance matrix involving the parameters of that particular source. The upper limits (here the lowest-energy and highest-energy bands) are 2σ.
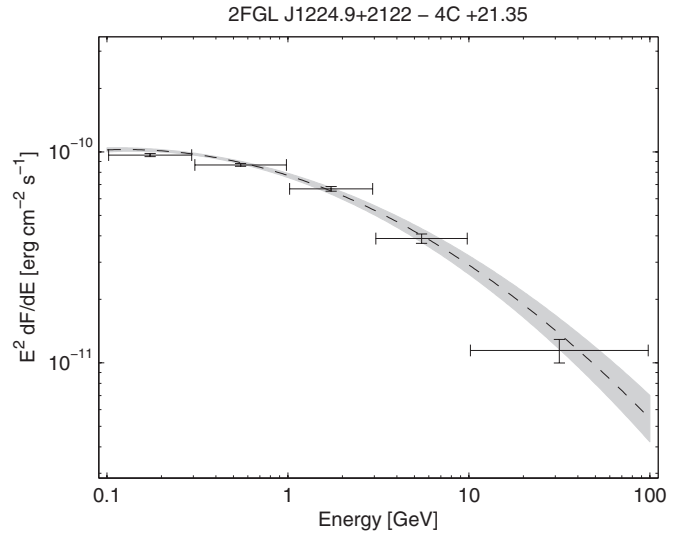
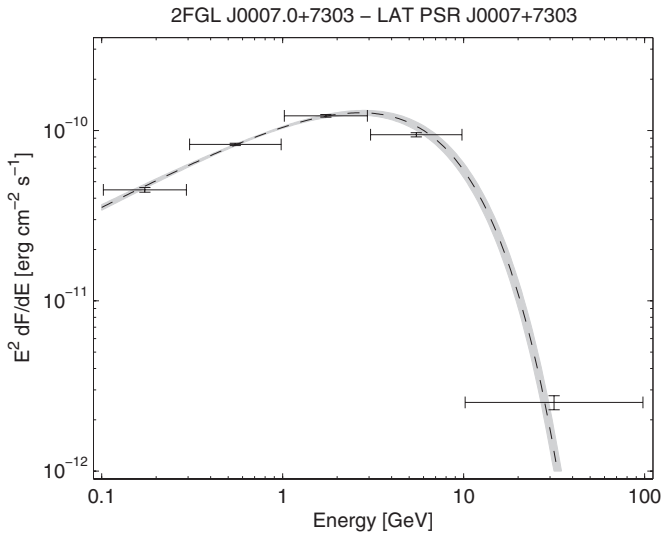2FGL J0007.0+7303 – LAT PSR J0007+7303

Figure 9. Spectrum of the pulsar in CTA1, as an example of an exponentially cutoff spectrum. See Figure 8 for details.

including the two brightest pulsars (Geminga and Vela) whose spectrum does not decrease as fast as a simple PLExpCutoff.

A few percent error in the effective area calibration as a function of energy may result in an incorrect report of significant curvature for very bright sources. There is no obvious rigorous way to enter systematic uncertainties in the $\mathrm{TS_{curve}}$ calculation (Section 3.3). In order to do that approximately, we note that $\mathrm{TS_{curve}}$ is an improved estimator of how much the spectrum deviates from a PL. The analog of $\mathrm{TS_{curve}}$ in 1FGL was $C_{\mathrm{nosyst}}^{\mathrm{PL}}$, applying Equation (3) to the PL fit with no f_i^{rel} term ($\mathrm{TS_{curve}}$ is a purely statistical quantity). We can compare $C_{\mathrm{nosyst}}^{\mathrm{PL}}$ with the same quantity $C_{\mathrm{syst}}^{\mathrm{PL}}$ obtained with the f_i^{rel} term (`Curvature_Index` of 1FGL). Their ratio is a measure of how much the systematic uncertainties reduced `Curvature_Index`. We can then apply that same ratio to $\mathrm{TS_{curve}}$ and we report in the catalog $\mathtt{Signif\_Curve} = \sqrt{\mathrm{TS_{curve}}\,C_{\mathrm{syst}}^{\mathrm{PL}}/C_{\mathrm{nosyst}}^{\mathrm{PL}}}$, converting to σ units.

2FGL J1224.9+2122 – 4C +21.35

Figure 10. Spectrum of the bright AGN 4C +21.35, as an example of a LogParabola spectrum. See Figure 8 for details.

We consider that sources with `Signif_Curve` >4 are significantly curved. The consequence of introducing the systematic uncertainties is that 40 sources in the catalog have a LogParabola spectrum because $\mathrm{TS_{curve}} > 16$ (Section 3.3) even though `Signif_Curve` <4. We do not claim that the curvature is real for those sources, even though it is statistically significant.

3.6. Variability

Temporal variability is relatively common in γ-ray sources and provides a powerful tool to associate them definitively with objects known at other wavelengths and to study the physical processes powering them. We present a light curve for each source in the catalog, produced by dividing the data into approximately monthly time bins and applying the likelihood analysis procedure to each. The details of the light curve analysis and how the results are presented are summarized below.

1. There are 24 time bins, starting at the beginning of the data set, approximately 54682.66 MJD (Section 2.1). The first 23 bins have durations of 30.37 days; the final has a duration of 27.88 days. The first 11 time bins correspond exactly to those of 1FGL.
2. The parameters describing the spectral shapes of the sources in the RoI are fixed in the light curve calculation. Only the normalizations of the source of interest, the diffuse backgrounds, and the bright and nearby catalog sources (see Section 3.2) are allowed to vary. We use binned likelihood, but do not distinguish *Front* and *Back* events. The pixel size is set to $0°.2$.
3. For each time bin, the photon flux over the full energy range (100 MeV to 100 GeV), F_i, its error, ΔF_i, and the detection significance, TS_i, are presented in the catalog. With the spectral shape of each source frozen in the light curve analysis, the relative uncertainty on F_{25} is the same as that of F_{35} and S_{25}, and it is reasonable to present the photon flux over the full energy range in this case.
4. For time bins where the source is too weak to be detected, those with $\mathrm{TS}_i < 10$ or $\Delta F_i/F_i > 0.5$, 95% upper limits F_i^{UL} are calculated following the same method as in Section 3.5. A fraction of those have flux exactly equal to 0, because the Poisson likelihood framework that we use does not accept negative flux values.

Table 3
Definitions of the Analysis Flags

Flag[a]	Meaning
1	Source with TS > 35 which went to TS < 25 when changing the diffuse model (Section 3.7). Note that sources with TS < 35 are not flagged with this bit because normal statistical fluctuations can push them to TS < 25.
2	Moved beyond its 95% error ellipse when changing the diffuse model.
3	Flux (>1 GeV) or energy flux (>100 MeV) changed by more than 3σ when changing the diffuse model. Requires also that the flux change by more than 35% (to not flag strong sources).
4	Source-to-background ratio less than 20% in highest band in which TS > 25. Background is integrated over πr_{68}^2 or 1 deg^2, whichever is smaller.
5	Closer than θ_{ref} from a brighter neighbor. θ_{ref} is defined in highest band in which source TS > 25, or the band with highest TS if all are <25. θ_{ref} is set to 2°.17 (FWHM) below 300 MeV, 1°.38 between 300 MeV and 1 GeV, 0°.87 between 1 GeV and 3 GeV, 0°.67 between 3 and 10 GeV and 0°.45 above 10 GeV ($2\,r_{68}$).
6	On top of an interstellar gas clump or small-scale defect in the model of diffuse emission; equivalent to the "c" designator in the source name (Section 3.9).
7	Not used.
8	Inconsistent position determination (Section 3.1.4); best position from optimization outside the 1σ (39% in 2D) contour from the TS map.
9	Elliptical quality >4 in *pointlike* (i.e., TS contour does not look elliptical).
10	Spectral fit quality >16.3 (Equation (3)).
11	Possibly due to the Sun (Section 3.6).
12	Highly curved spectrum; LogParabola β fixed to 1 or PLExpCutoff Spectral_Index fixed to 0 (see Section 3.3).

Note. [a] In the FITS version the values are encoded as individual bits in a single column, with Flag n having value $2^{(n-1)}$. For information about the FITS version of the table see Table 12 in Appendix C.

5. In the case of an upper limit, the best-fit flux value is given in the catalog, and the error is replaced by $0.5(F_i^{UL} - F_i)$. This allows bands with upper limits to be treated consistently with the other bands while preserving enough information to extract the upper limits. The FITS version of the catalog[94] has a flag column to indicate when an entry in a flux history is an upper limit. Please note that this is a different convention to that used to report flux upper limits for the energy bands (Section 3.5). See Appendix C for more information.

6. A total of 340 sources have only upper limits on monthly timescales. These sources have an average integrated significance over the full two-year data set of 5.3σ. At the opposite extreme, 94 sources are detected significantly in every one of the time periods.

To test for variability in each source we construct a variability index from the value of the likelihood in the null hypothesis, that the source flux is constant across the full two-year period, and the value under the alternate hypothesis where the flux in each bin is optimized:

$$\mathrm{TS_{var}} = 2[\log \mathcal{L}(\{F_i\}) - \log \mathcal{L}(F_{Const})]$$
$$= 2\sum_i [\log \mathcal{L}_i(F_i) - \log \mathcal{L}_i(F_{Const})] = 2\sum_i V_i^2, \quad (4)$$

where the log likelihood for the full time period, $\log \mathcal{L}(\{F_i\})$, can be expressed as a sum of terms for the individual time bands, $\log \mathcal{L}_i$. If the null hypothesis is correct $\mathrm{TS_{var}}$ is distributed as χ^2 with 23 degrees of freedom, and a value of $\mathrm{TS_{var}} > 41.6$ is used to identify variable sources at a 99% confidence level. For most sources the value for F_{Const} is close to the value derived from
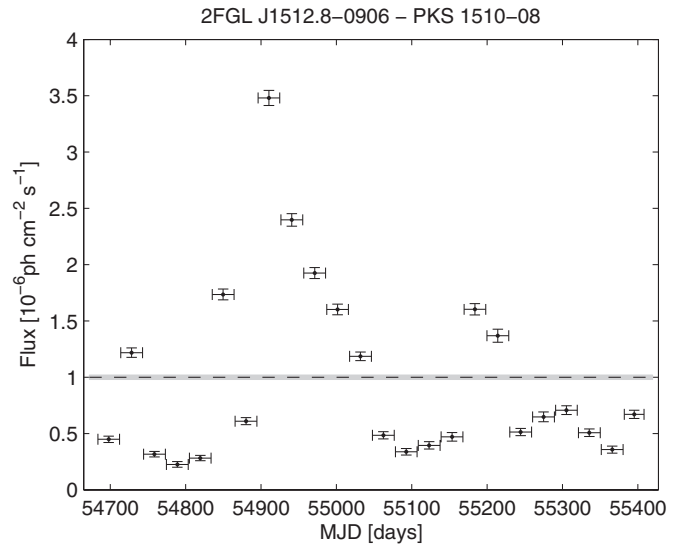
Figure 11. Light curve for the bright blazar PKS 1510−089 in the full energy range (100 MeV to 100 GeV). The dashed line depicts the average flux from the analysis of the full 24 month data set.

the likelihood analysis of the full time period, although strong variability in nearby background sources can cause to them to differ in some cases. The light curve for PKS 1510−089, a bright blazar, is shown in Figure 11. This source is easily flagged as variable, with $\mathrm{TS_{var}} = 6406$.

Upper limits calculated through the profile method are handled naturally in the variability index procedure described above, but those calculated using the Bayesian method would have to be included in an ad hoc manner. Instead, when calculating the variability index, the results of the profile method are used for all upper limits.
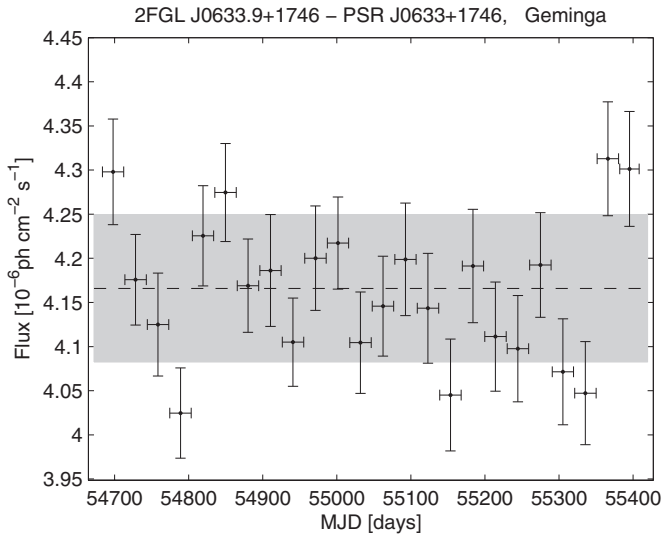
Figure 12. Light curve for the bright pulsar Geminga (100 MeV to 100 GeV). The gray band depicts the size of the 2% systematic correction applied to the calculation of the variability index. The error bars on the flux points show the statistical errors only.
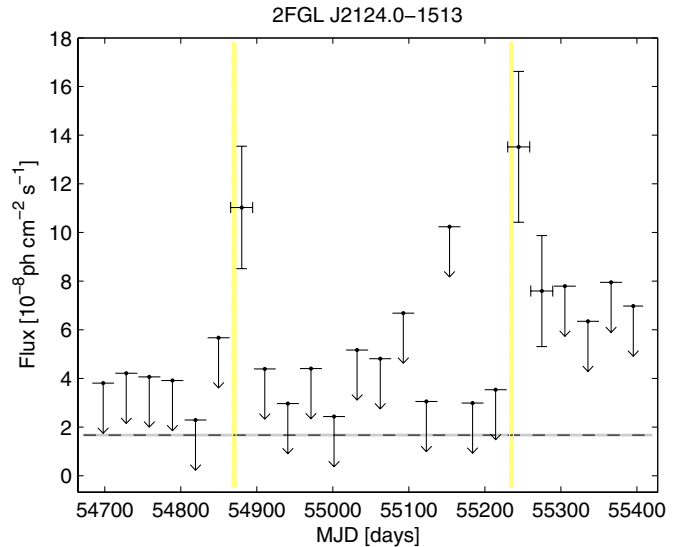

Figure 13. Light curve for the unassociated source 2FGL J2124.0−1513 (100 MeV to 100 GeV). Time periods in which the Sun is closer than 2°.5 to the source are marked with yellow vertical bands. In this case, a large fraction of the detection significance is accumulated during these periods, and the source is flagged as suspicious in the catalog.

(A color version of this figure is available in the online journal.)

As in 1FGL, the brightest pulsars detected by the LAT are flagged as being variable with this procedure. This apparent variability is caused by systematic errors in the calculation of the source exposure, resulting from small inaccuracies in the dependence of the IRFs on the source viewing angle, coupled with changes in the observing profile as the orbit of the spacecraft precesses. We introduce a correction factor to account for these errors and fix the size of this correction such that the bright pulsars are steady. Specifically, we scale each V_i^2 in the summation of TS_{var} by a factor which combines the error on the flux each time bin in quadrature with a fixed fraction of the overall flux,

$$TS_{var} = 2 \sum_i \frac{\Delta F_i^2}{\Delta F_i^2 + f^2 F_{Const}^2} V_i^2.$$

A value of $f = 0.02$, i.e., a 2% systematic correction factor, was found sufficient such that only PSR J1741−2054 remains (marginally) above threshold among the LAT pulsars, excluding the Crab which was recently discovered to have a highly variable nebular component at LAT energies (Tavani et al. 2011; Abdo et al. 2011c). This is smaller than the 3% correction required in 1FGL, the improvement resulting from the higher-fidelity IRFs used in this work. This systematic error component is included in the flux errors reported in the catalog FITS file. Figure 12 shows the light curve for the pulsar Geminga (PSR J0633+1746), one of the brightest non-variable sources in 2FGL.

The Sun is a bright, extended source of γ-rays, both from cosmic-ray interactions in its outer atmosphere and from IC scattering of cosmic-ray electrons on the solar radiation field, which produces an extended γ-ray halo around the Sun (Abdo et al. 2011b). For sources close to the ecliptic, solar conjunctions can lead to significant enhancements of the flux detected during the time periods when the Sun is closer than approximately 2°.5 to the source. Sources for which a large fraction of the total detection significance comes during such periods are flagged as suspicious in the catalog. The light curve for such a source, 2FGL J2124.0−1513, is shown in Figure 13. The Moon is comparably bright to the Sun in γ-rays (A. A. Abdo et al. 2012a, in preparation) and lunar conjunctions also potentially

affect the fluxes measured from LAT sources, but the higher apparent speed of the Moon and parallax from the motion of the spacecraft mean that such close conjunctions are brief, and the precession of the orbit of the Moon means that for any given source conjunctions are less frequent than the ~28 day period of the orbit. In addition, the γ-ray emission of the Moon does not include a bright, extended IC component (A. A. Abdo et al. 2012a, in preparation). Hence, we do not attempt to identify sources which may be affected by the Moon nor to flag time periods where lunar conjunctions occur.

Light curves for all 2FGL sources are available from the *Fermi* Science Support Center.

3.7. Limitations and Systematic Uncertainties

A limitation for the catalog analysis is source confusion. (The related issue of systematics for localization is discussed in Section 3.1.4.) Confusion is of course strong in the inner Galaxy, where the source density is very high, but it is also a significant issue elsewhere. The average distance between sources outside the Galactic plane is 2°.8 (it was 3° in 1FGL), to be compared with a per-photon containment radius $r_{68} = 0°.8$ at 1 GeV where the sensitivity is best. The ratio between these numbers is not large enough that confusion can be neglected. As for the 1FGL catalog analysis (Abdo et al. 2010f) we study source confusion by evaluating the distribution of distances between each source and its nearest neighbor (D_n) in the area of the sky where the source density is approximately uniform, i.e., outside the Galactic plane. This is shown in Figure 14, to be compared with Figure 9 of Abdo et al. (2010f) which also details the expected distribution. The histogram still falls off toward $D_n = 0$, but follows the expected distribution down to 1° or so instead of 1°.5 in 1FGL. We estimate that some 43 sources within 1° of another one were missed because of confusion (to be compared with the 1319 sources observed at $|b| > 10°$). This means that the fraction of missed sources decreased from 7.7% in the 1FGL analysis to 3.3% for 2FGL. This attests to the progress made in the detection process (Section 3.1).
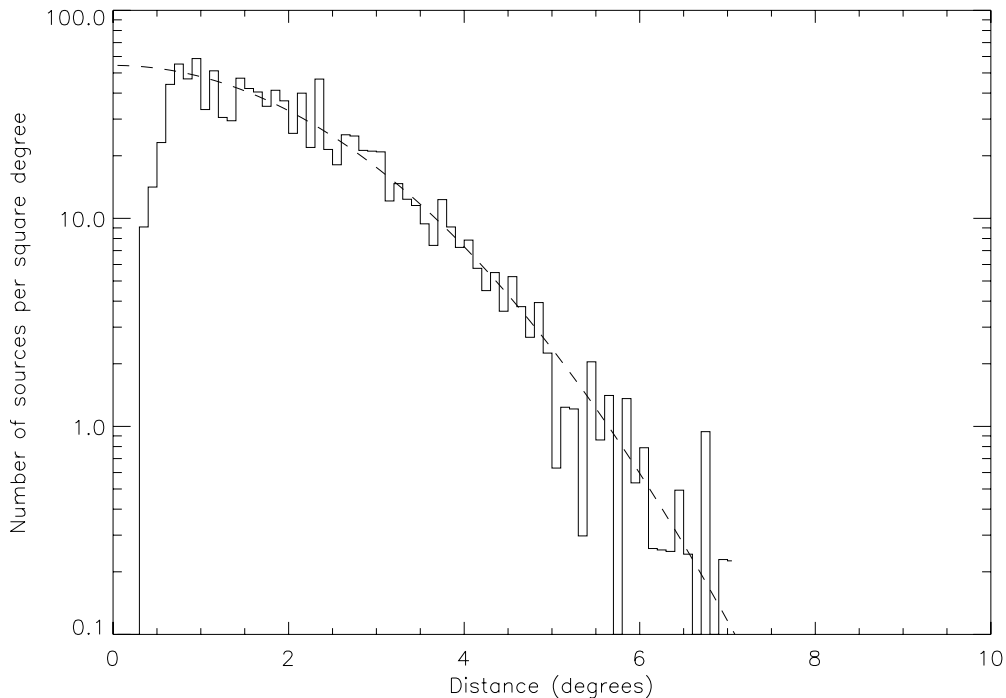
Figure 14. Distribution of the distances D_n to the nearest neighbors of all detected sources at $|b| > 10°$. The number of entries is divided by $2\pi D_n \Delta D_n$ in which ΔD_n is the distance bin, in order to eliminate the two-dimensional geometry. The overlaid curve is the expected Gaussian distribution for a uniform distribution of sources with no confusion.

An important issue for the evaluation of spectra is the systematic uncertainties of the effective area of the instrument. Compared to the 1FGL IRFs (P6_V3), the current P7_V6 response functions have somewhat reduced systematic uncertainties. The current estimate of the remaining systematic uncertainty is 10% at 100 MeV, decreasing to 5% at 560 MeV and increasing to 10% at 10 GeV and above (A. A. Abdo et al. 2012b, in preparation). This uncertainty applies uniformly to all sources. Our relative errors (comparing one source to another or the same source as a function of time) are much smaller, as indicated in Section 3.6.

The model of diffuse emission is the other important source of uncertainties. Contrary to the effective area, it does not affect all sources equally: its effects are smaller outside the Galactic plane where the diffuse emission is fainter and varying on larger angular scales. It is also less of a concern in the high-energy bands (>3 GeV) where the core of the PSF is narrow enough that the sources dominate the background under the PSF. But it is a serious concern inside the Galactic plane in the low-energy bands (<1 GeV) and particularly inside the Galactic ridge ($|l| < 60°$) where the diffuse emission is strongest and very structured, following the molecular cloud distribution. It is not easy to assess precisely how large the uncertainties are, because they relate to uncertainties in the distributions of interstellar gas, the interstellar radiation field, and cosmic rays, which depend in detail on position on the sky. We discuss the Galactic ridge more specifically in Section 3.9.

For an automatic assessment we have tried re-extracting the source locations and fluxes assuming the same diffuse model that we used for 1FGL, and also the same event selection as in 1FGL but with improved calibration (P6_v11). The results show that the systematic uncertainty more or less follows the statistical one (i.e., it is larger for fainter sources in relative terms) and is of the same order. More precisely, the dispersions of flux and spectral index are 0.8σ at $|b| > 10°$, and 1.3σ at

$|b| < 10°$. We have not increased the errors accordingly because this older model does not fit the data as well as the newer one. From that point of view we may expect this estimate to be an upper limit. On the other hand, both models rely on nearly the same set of H I and CO maps of the gas in the interstellar medium, which we know are an imperfect representation of the mass. That is, potentially large systematic uncertainties are not accounted for by the comparison. So, we present the figures as qualitative estimates. We also use the same comparison to flag outliers as suspect (Section 3.10).

Finally, we note that handling *Front* and *Back* events separately for the significance and spectral-shape computation (Section 3.2) introduces another approximation. Because the free parameters are the same for both categories of events, this amounts to assuming that the isotropic diffuse emission is the same for *Front* and *Back* events. This is actually not true because it contains internal background that is larger for *Back* events (see Section 2). This effect is significant only below 400 MeV (Section 2.2), and so the consequence is an underestimate of the low-energy flux, which results in a systematic hardening of the measured PL spectral index but which is nearly always less than its statistical uncertainty. Thus, in terms of the absolute change in spectral index, the effects are greatest for soft sources.

3.8. Point Sources and Extended Sources

Except for the diffuse emission and the 12 sources explicitly considered as spatially extended, all sources in the catalog are assumed to be point-like. Just as the modeling of the diffuse emission can affect the properties of point sources (as discussed in the previous section), the treatment of known or unknown extended sources can similarly influence the analysis of nearby point sources. This influence can be felt in three ways.

1. The modeling of an extended source is limited by the detailed knowledge of the γ-ray emissivity of the source

16

as a function of position on the sky. As noted in Section 3.4, the modeling for the catalog was done using largely geometric functions. The true distribution can have residual excesses that the catalog analysis then treats as point sources. Examples are the sources near the LMC: 2FGL J0451.8−7011, 2FGL J0455.8−6920, 2FGL J0532.5−7223, 2FGL J0533.3−6651, and 2FGL J0601.1−7037. Although some of these may be unrelated to the LMC itself (two have blazar associations), some may be residuals from the modeling. Sources close to any of the extended sources should be treated warily in detailed analysis of such regions.

2. Some known or likely extended sources are not among the 12 that were modeled for the catalog analysis, having been recognized and measured only after the catalog analysis was largely complete. In such cases, the catalog analysis finds one or more point sources at or near the possible extended source. Two clear examples are SNRs. RX J1713.7−3946 is represented in the catalog by 2FGL J1712.4−3941, but recent analysis has shown this SNR to be an extended GeV source (Abdo et al. 2011d). In Table 11, RX J0852.0−4622 shows four associated 2FGL sources: J0848.5−4535, J0851.7−4635, J0853.5−4711, and J0855.4−4625. All of these are likely part of the spatially extended SNR (Tanaka et al. 2011). Other clusters of sources in Table 11 may indicate yet-unresolved extended objects. As longer exposures with the LAT collect more of the highest-energy photons with the best angular resolution, additional spatial structure will be revealed in the data.

3. A spectral bias can be introduced if an extended source is analyzed as if it were a point source. In such cases the calculated spectrum is likely to be softer than the true spectrum. At higher energies where the LAT PSF is closer to the size of the extended source, the extension will cause such photons to be lost.

3.9. Sources Toward Local Interstellar Clouds and the Galactic Ridge

The interstellar part of the model for diffuse emission of the Galaxy has greatly improved since the 1FGL catalog analysis, in particular in angular resolution (Section 2.2). However, the use of large-scale rings in the Milky Way and of a single ring in the solar neighborhood (containing most of the gas-related diffuse emission off the Galactic plane) does not allow for small-scale variations in the gas and dust properties used to derive the target mass for cosmic rays, or in the cosmic-ray spectrum itself. The optical depth correction applied in deriving column densities from the H I 21 cm line observations also is necessarily based on the approximation that the gas has a uniform spin temperature across the Galaxy. As a result, extended and structured excesses of γ radiation are present above the diffuse model. The renormalization of the diffuse model within each RoI lessens, but cannot always remove the impact of the diffuse excesses. Point sources detected in the regions of the excesses can be formally very significant but are necessarily suspect (see Figure 15).

One particularly difficult region is the local arm tangent in Cygnus. The region $75° \leqslant l \leqslant 85°$, $|b| \leqslant 15°$ contains 18 2FGL sources, 13 without firm identifications. Of these 13, we find that eight sources with detection significances ranging up to 13σ have properties that are especially sensitive to the diffuse emission model (see Section 3.10, in particular Flags 1–4 in Table 3). The diffuse emission in Cygnus has recently been
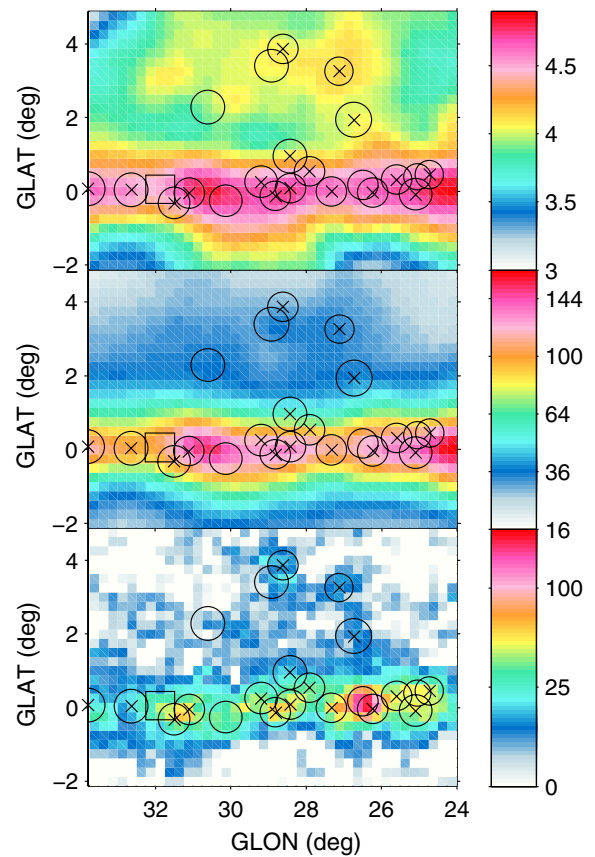

Figure 15. From top to bottom: the CO contribution to the interstellar photon counts, the total interstellar photon counts, and the photon residual counts above the model for diffuse γ-ray emission, all in the 1–11 GeV energy band. The circles mark the effective 50% containment radii of the 2FGL sources for the 1–10 GeV band. The "c" sources are crossed. The square notes an identified source. The photon residual map has been smoothed for display with a $\sigma = 0°.125$ Gaussian. The 2FGL "c" sources seen above the Galactic plane, with TS ranging from 26 to 75, follow an extended and clumpy excess of interstellar emission.

(A color version of this figure is available in the online journal.)

the subject of a detailed study (Ackermann et al. 2012b) and evidence suggests that some of the excess diffuse emission is due to an extended cocoon of unusually hard-spectrum cosmic rays (Ackermann et al. 2011a).

We have used a dust reddening map to trace substantial amounts of dark gas in addition to the atomic and molecular gas seen in H I and CO emission lines (Grenier et al. 2005; Ade et al. 2011a). This made essential improvements over wide regions from low to medium latitudes, but inaccuracies in the infrared color corrections used to build the reddening map (Schlegel et al. 1998) can cause diffuse residuals toward bright H II regions or stellar clusters by artificially lowering the gas column densities measured in their directions (see Figures 10 and 11 of Abdo et al. 2010f). There are fewer such artifacts in 2FGL than in 1FGL, but examples can be found in Orion, Taurus, and near the source LS I +61 303; see also Figure 16. Another known limitation of the diffuse model relates to the optical thickness of the CO lines and the saturation of the CO intensity toward very dense clouds. Since stellar clusters are born in the clouds, both CO saturation and dust temperature corrections may cooperate to underpredict the gas mass in dense molecular clouds. Self-absorption of the H I lines also leads to underpredicted column densities in the dense atomic phase. These limitations are particularly relevant
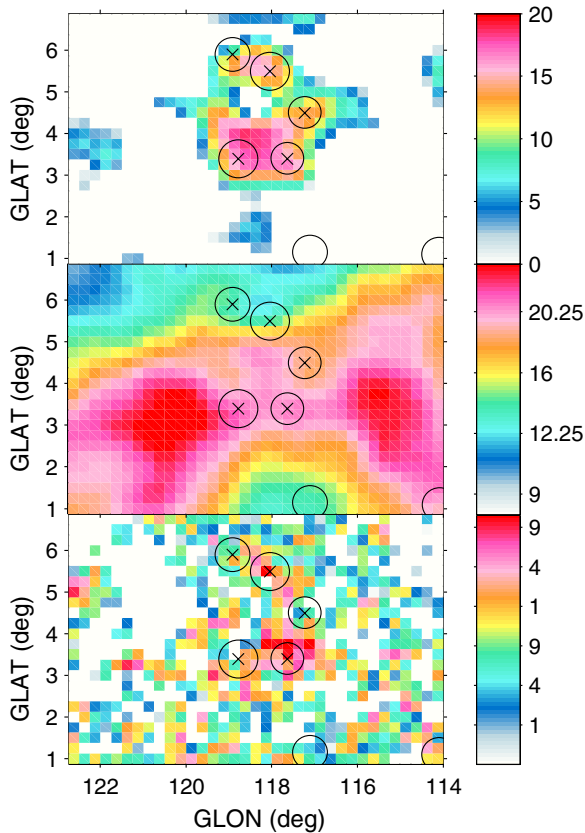
Figure 16. From top to bottom: the absolute value of the dust negative residual photon counts incorporated in the diffuse model, the total interstellar photon counts, and the photon residual counts above the diffuse model, all in the 1–11 GeV energy band. The circles mark the effective 50% containment radii of the 2FGL sources for the 1–10 GeV band. The "c" sources are crossed. The photon residual map has been smoothed for display with a $\sigma = 0°.125$ Gaussian. The 2FGL "c" sources are distributed along the rim of a large H ɪɪ region where the dust temperature correction led to an overestimate of the dust column densities in the ionized gas. The negative dust residuals have artificially reduced the diffuse γ-ray intensity in these directions.

(A color version of this figure is available in the online journal.)

at low latitudes, in the inner Galaxy or toward the tangent directions of the Galactic spiral arms.

We have inspected all the 2FGL sources to search for potential problems with the underlying diffuse model. It is unlikely that sources with very high TS can be diffuse excesses. Based on the examination of the sources toward Cygnus, Orion, and other nearby clouds, as well as the 1FGL sources with the "c" designation that are not confirmed in 2FGL, we tentatively consider that sources with TS $\gtrsim$ 200, 130, or 80 are unlikely to be diffuse features depending on the intensity of the diffuse background (respectively, when the photon count per pixel N_{bkgd}, integrated from 589 MeV to 11.4 GeV in the diffuse model cube, without the isotropic contribution, is $N_{\mathrm{bkgd}} > 100$, $60 \leqslant N_{\mathrm{bkgd}} \leqslant 100$, or $N_{\mathrm{bkgd}} < 60$).

Given the large change in the width of the PSF across the LAT energy band, we computed the effective 50% containment radius for each source from its best-fit spectrum. We overlaid these on predicted photon count maps from the Galactic diffuse model, both for the total emission and for the individual gas components in each phase, in seven energy bands (the five energy bands of the catalog, plus the integral 0.5–10 GeV and 1–10 GeV bands). We also compared photon residual maps (data minus model) in the same energy bands against the predicted count maps

for the individual gas components. We also took into account the TS values reached in the five catalog energy bands and the spectral index of each source. Off the Galactic plane, we flagged (Flag 6 of Table 3) unassociated sources coinciding with dust temperature or dense CO defects, or concurrent with extended residuals that followed interstellar features (as in Figure 15). Sources with TS larger than the background-dependent threshold quoted above or with a spectral index $\Gamma < 2$ were not flagged. In the Galactic plane (i.e., at $|b| \leqslant 2°$ for $|l| \leqslant 70°$, or $|b| \leqslant 3°$ at higher longitudes), we flagged two types of sources: (1) unassociated sources with overlapping 50% containment radii above 500 MeV, unless their TS exceeded the background-dependent threshold or their spectral index were <2; (2) low-significance unassociated sources with TS $\leqslant 80$ for $N_{\mathrm{bkgd}} \geqslant 160$, unless their spectral indices were <2. This strategy ensured that most of the Galactic ridge sources, which are closely packed together to make up for the extended photon residuals along the plane, are flagged, but it leaves all the identified and associated, intense, and hard sources out of the systematic ridge flag we had used in 1FGL. Every source was then manually checked with the same set of maps as for the work at higher latitude.

We have added the designator "c" to the names of the flagged sources to indicate that they are to be considered as potentially confused with interstellar emission. Their position, emission characteristics, or even existence may not be reliable. The "c" designator applies to 162 sources in the 2FGL catalog.

3.10. Analysis Flags

As in 1FGL we identified a number of conditions that can shed doubt on a source. They are described in Table 3. In the FITS version of the catalog, these flags are summarized in a single integer column (Flags). Each condition is indicated by one bit among the 16 bits forming Flags. The bit is raised (set to 1) in the dubious case, so that sources without any warning sign have Flags = 0.

Flags 1–9 have similar intent as in 1FGL, but differ in detail.

1. In Flag 4, we reduced the threshold on source to background ratio to 20%, because the diffuse model has improved.
2. The distances triggering Flag 5 have changed because the PSF knowledge has improved. The core of the PSF at low energy is actually better than the P6V3 estimate used in 1FGL, so the critical distance is lower at low energy. On the other hand, the measured in-flight PSF at high energy is much broader than the P6V3 estimate (Abdo et al. 2009h), so the critical distance is about twice as great as for the 1FGL analysis above 10 GeV.
3. We do not use *gtfindsrc* in 2FGL because it is based on unbinned likelihood. Therefore Flag 7 is not used.
4. Flag 8 compares the best position obtained from direct optimization with the contours extracted from the TS maps.
5. The threshold for Flag 9 on elliptical quality was decreased to 4. The improved localization procedure allowed being a little more stringent here.

Flags 10–12 are new. Figure 17 shows the distribution on the sky of flagged 2FGL sources.

4. THE 2FGL CATALOG

The basic description of the 2FGL catalog is in Section 4.1, including a listing of the main table contents and some of the primary properties of the sources in the catalog. We present a
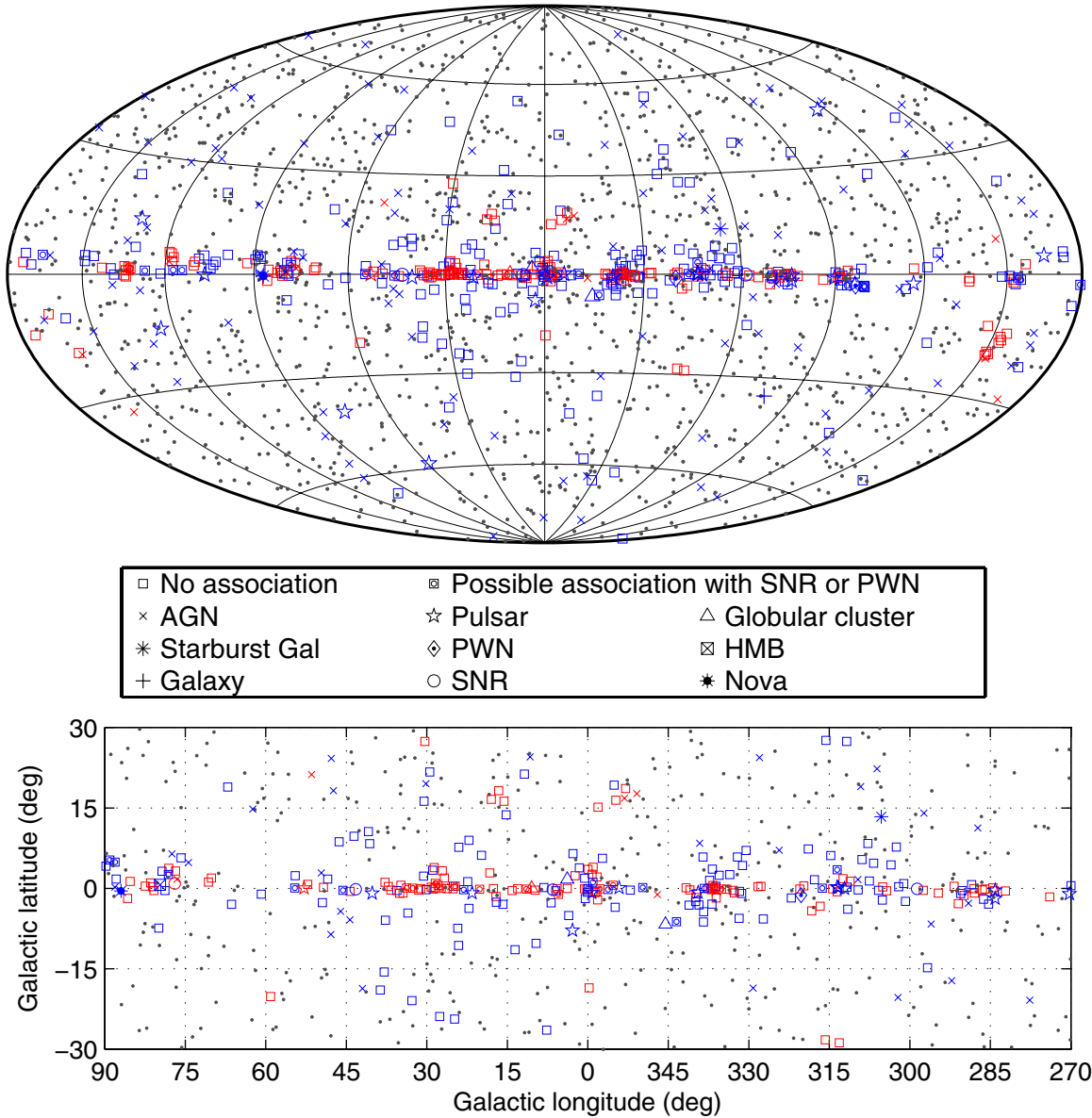
Figure 17. Full sky map (top) and blow-up of the inner Galactic region (bottom) showing flagged sources by source class. Sources potentially confused with diffuse emission, i.e., those with a "c" designator in their names (and for which Flag 6 is set) are shown in red; those with any other flag set are shown in blue. Sources with no flag set are shown as small dots.

detailed comparison of the 2FGL catalog with the 1FGL catalog in Section 4.2.

4.1. Catalog Description

Table 4 is the catalog, with information for each of the 1873 sources; see Table 5 for descriptions of the columns. The source designation is 2FGL JHHMM.m+DDMM where 2 indicates that this is the second LAT catalog, FGL represents *Fermi* Gamma-ray LAT. Sources close to the Galactic ridge and some nearby interstellar cloud complexes are assigned names of the form 2FGL JHHMM.m+DDMMc, where the c indicates that caution should be used in interpreting or analyzing these sources. Errors in the model of interstellar diffuse emission, or an unusually high density of sources, are likely to affect the measured properties or even existence of these 162 sources (see Section 3.9). In addition a set of analysis flags has been defined to indicate sources with unusual or potentially problematic characteristics

(see Section 3.9). The "c" designator is encoded as one of these flags. An additional 315 sources have one or more of the other analysis flags set. The 12 sources that were modeled as extended for 2FGL (Section 3.4) are singled out by an e at the end of their names.

The designations of the classes that we use to categorize the 2FGL sources are listed in Table 6 along with the numbers of sources assigned to each class. We distinguish between associated and identified sources, with associations depending primarily on close positional correspondence (see Section 5.2) and identifications requiring measurement of correlated variability at other wavelengths or characterization of the 2FGL source by its angular extent (see Section 5.1). In the cases of multiple associations with a 2FGL source, we adopt the single association that is statistically most likely to be true if it is above the confidence threshold (see Section 5.2); the one exception is the Crab pulsar and PWN, which are listed as being associated with the same 2FGL source (see Section 5.1). Sources associated

Table 4
LAT Two-year Catalog

Name 2FGL	R.A.	Decl.	l	b	θ_1	θ_2	ϕ	σ	F_{35}	ΔF_{35}	S_{25}	ΔS_{25}	Γ_{25}	$\Delta\Gamma_{25}$	Mod	Var	Flags	γ-Ray Assoc.	TeV	Class	ID or Assoc.	Ref.
J0000.9−0748	0.234	−7.815	88.829	−67.281	0.195	0.167	48	5.9	0.5	0.1	6.8	1.2	2.39	0.14	PL	...	...	1FGL J0000.9−0745	...	bzb	PMN J0001−0746	...
J0001.7−4159	0.439	−41.996	334.076	−71.997	0.122	0.114	62	5.9	0.5	0.1	5.3	1.1	2.14	0.19	PL	T	...	1FGL J0001.9−4158	...	agu	1RXS J000135.5-41551	...
J0002.7+6220	0.680	62.340	117.312	0.001	0.093	0.089	9	13.7	2.9	0.3	25.2	2.5	2.50	0.13	LP	...	...	1FGL J0003.1+6227	...	...	...	...
J0004.2+2208	1.056	22.137	108.732	−39.430	0.194	0.137	63	5.4	0.4	0.1	6.3	1.2	2.49	0.15	PL	...	...	1FGL J0004.3+2207	...	...	...	...
J0004.7−4736	1.180	−47.612	323.890	−67.571	0.112	0.096	14	12.6	0.9	0.1	13.1	1.3	2.45	0.09	PL	T	...	1FGL J0004.7−4737	...	bzq	PKS 0002−478	...
J0006.1+3821	1.525	38.350	113.245	−23.667	0.144	0.123	71	12.2	1.0	0.1	16.1	1.5	2.60	0.08	PL	...	...	1FGL J0005.7+3815	...	bzq	S4 0003+38	...
J0007.0+7303	1.774	73.055	119.665	10.465	0.010	0.010	−33	189.5	65.7	0.9	429.6	5.5	1.45	0.02	EC	...	...	1FGL J0007.0+7303 0FGL J0007.4+7303 EGR J0008+7308 1AGL J0006+7311	...	PSR	LAT PSR J0007+7303	...
J0007.7+6825c	1.925	68.423	118.911	5.894	0.173	0.170	64	6.2	1.0	0.2	17.5	2.7	2.61	0.10	PL	...	6,10	1FGL J0005.1+6829	...	...	...	...
J0007.8+4713	1.974	47.230	115.304	−14.996	0.062	0.053	29	17.6	2.1	0.2	23.7	2.1	2.10	0.06	PL	...	...	...	...	bzb	MG4 J000800+4712	...
J0008.7−2344	2.196	−23.736	49.986	−79.795	0.189	0.161	−9	4.1	0.3	0.1	4.7	1.8	1.62	0.25	PL	...	...	...	...	bzb	RBS 0016	...
J0009.0+0632	2.262	6.542	104.453	−54.801	0.129	0.123	−10	5.7	0.5	0.1	6.7	1.3	2.40	0.16	PL	...	...	1FGL J0008.9+0635	...	bzb	CRATES J0009+0628	...

Notes. R.A. and decl. are celestial coordinates in J2000 epoch, l and b are Galactic coordinates, in degrees; θ_1 and θ_2 are the semimajor and semiminor axes of the 95% confidence source location region; ϕ is the position angle in degrees east of north; F_{35} and ΔF_{35} are photon flux 1 GeV–100 GeV in units of 10^{-9} cm^{-2} s^{-1}; S_{25} and ΔS_{25} are the energy flux 100 MeV–100 GeV in units of 10^{-12} erg cm^{-2} s^{-1}; Γ_{25} and $\Delta\Gamma_{25}$ are the photon power-law index and uncertainty for a power-law fit; Mod is the spectral model used (PL for power-law, EC for exponential cutoff, and LP for log parabolic); Var is the variability flag (see the text); Flags are the analysis flags (see the text); γ-ray Assoc. lists associations with other catalogs of GeV γ-ray sources; TeV indicates an association with a point-like or small angular size TeV source (P) or extended TeV source; Class designates the astrophysical class of the associated source (see the text); ID or Assoc. lists the primary name of the associated source or identified counterpart; Ref. cross references LAT collaboration publications.

(This table is available in its entirety in a machine-readable form in the online journal. A portion is shown here for guidance regarding its form and content.)

Table 5
LAT Second Catalog Description

Column	Description
Name	2FGL JHHMM.m+DDMM[c/e], constructed according to IAU Specifications for Nomenclature; m is decimal minutes of R.A.; in the name R.A. and decl. are truncated at 0.1 decimal minutes and 1′, respectively; c indicates that based on the region of the sky the source is considered to be potentially confused with Galactic diffuse emission; e indicates a source that was modeled as spatially extended (see Section 3.4).
R.A.	Right Ascension, J2000, deg, 3 decimal places.
Decl.	Declination, J2000, deg, 3 decimal places.
l	Galactic Longitude, deg, 3 decimal places.
b	Galactic Latitude, deg, 3 decimal places.
θ_1	Semimajor radius of 95% confidence region, deg, 3 decimal places.
θ_2	Semiminor radius of 95% confidence region, deg, 3 decimal places.
ϕ	Position angle of 95% confidence region, deg east of north, 0 decimal place.
σ	Significance derived from likelihood test statistic for 100 MeV–100 GeV analysis, 1 decimal place.
F_{35}	Photon flux for 1 GeV–100 GeV, 10^{-9} photons cm^{-2} s^{-1}, summed over 3 bands, 1 decimal place.
ΔF_{35}	1σ uncertainty on F_{35}, same units and precision.
S_{25}	Energy flux for 100 MeV–100 GeV, 10^{-12} erg cm^{-2} s^{-1}, from power-law fit, 1 decimal place.
ΔS_{25}	1σ uncertainty on S_{25}, same units and precision.
Γ	Photon number power-law index, 100 MeV–100 GeV, 2 decimal places.
$\Delta\Gamma$	1σ uncertainty of photon number power-law index, 100 MeV–100 GeV, 2 decimal places.
Mod.	PL indicates power-law fit to the energy spectrum; LP indicates log-parabola fit to the energy spectrum; EC indicates power law with exponential cutoff fit to the energy spectrum.
Var.	T indicates <1% chance of being a steady source; see the note in the text.
Flags	See Table 3 for definitions of the flag numbers.
γ-Ray Assoc.	Positional associations with 0FGL, 1FGL, 3EG, EGR, or 1AGL sources.
TeV	Positional association with a TeVCat source, P for angular size <20′, E for extended.
Class	Like "ID" in 3EG catalog, but with more detail (see Table 6). Capital letters indicate firm identifications; lower-case letters indicate associations.
ID or Assoc.	Designator of identified or associated source.
Ref.	Reference to associated paper(s).

Table 6
LAT 2FGL Source Classes

Description	Identified		Associated	
	Designator	Number	Designator	Number
Pulsar, identified by pulsations	PSR	83	. . .	. . .
Pulsar, no pulsations seen in LAT yet	. . .	. . .	psr	25
Pulsar wind nebula	PWN	3	pwn	0
Supernova remnant	SNR	6	snr	4
Supernova remnant/pulsar wind nebula	. . .	. . .	†	58
Globular cluster	GLC	0	glc	11
High-mass binary	HMB	4	hmb	0
Nova	NOV	1	nov	0
BL Lac object type of blazar	BZB	7	bzb	429
FSRQ type of blazar	BZQ	17	bzq	353
Non-blazar active galaxy	AGN	1	agn	10
Radio galaxy	RDG	2	rdg	10
Seyfert galaxy	SEY	1	sey	5
Active galaxy of uncertain type	AGU	0	agu	257
Normal galaxy (or part)	GAL	2	gal	4
Starburst galaxy	SBG	0	sbg	4
Class uncertain	. . .	. . .	. . .	1
Unassociated	. . .	. . .	. . .	575
Total	. . .	127	. . .	1746

Notes. The designation "†" indicates potential association with SNR or PWN (see Table 11). Designations shown in capital letters are firm identifications; lower case letters indicate associations. In the case of AGNs, many of the associations have high confidence (Ackermann et al. 2011b). Among the pulsars, those with names beginning with LAT were discovered with the LAT. In the FITS version of the 2FGL catalog, the "†" designator is replaced with "spp"; see Appendix C.

with SNRs are often also associated with PWNe and pulsars, and the SNRs themselves are often not point-like. We do not attempt to distinguish among the possible classifications and instead list plausible associations of each class for unidentified

2FGL sources found to be positionally associated with SNRs (see Section 5.2.7).

The photon flux for 1–100 GeV (F_{35}; the subscript ij indicates the energy range as 10^i–10^j MeV) and the energy flux for

Table 7
Second LAT Catalog: Fluxes in Bands

Name 2FGL	100 MeV–300 MeV			300 MeV–1 GeV			1 GeV–3 GeV			3 GeV–10 GeV			10 GeV–100 GeV		
	F_1[a]	ΔF_1[a]	$\sqrt{TS_1}$	F_2[a]	ΔF_2[a]	$\sqrt{TS_2}$	F_3[b]	ΔF_3[b]	$\sqrt{TS_3}$	F_4[c]	ΔF_4[c]	$\sqrt{TS_4}$	F_5[c]	ΔF_5[c]	$\sqrt{TS_5}$
J0000.9−0748	1.4	0.0	1.5	0.3	0.1	5.3	0.5	0.0	2.5	2.0	0.0	2.5	0.7	0.0	2.0
J0001.7−4159	1.5	0.0	2.2	0.2	0.0	2.8	0.5	0.0	2.6	1.6	0.6	5.2	0.9	0.0	0.0
J0002.7+6220	1.9	0.7	3.5	1.3	0.2	9.2	2.6	0.4	8.7	4.1	1.1	5.2	0.5	0.0	0.0
J0004.2+2208	1.6	0.0	2.0	0.3	0.1	4.8	0.4	0.0	1.6	1.3	0.6	3.7	0.5	0.0	0.0
J0004.7−4736	2.2	0.4	5.8	0.4	0.1	7.7	0.9	0.2	7.9	1.3	0.6	4.1	0.6	0.0	0.0
J0006.1+3821	2.7	0.5	5.9	0.5	0.1	7.0	0.9	0.2	6.2	2.3	0.0	2.8	0.6	0.0	0.0
J0007.0+7303	17.9	0.6	37.6	11.6	0.2	96.0	49.9	0.9	122.7	149.9	4.2	91.3	12.5	1.2	27.1
J0007.7+6825c	2.8	0.0	0.6	1.1	0.2	6.1	0.9	0.3	3.2	1.3	0.0	0.0	1.0	0.0	1.9
J0007.8+4713	2.7	0.4	6.6	0.6	0.1	8.4	1.5	0.2	9.5	4.9	1.0	9.3	1.2	0.5	5.2
J0008.7−2344	0.5	0.0	0.0	0.1	0.0	0.1	0.6	0.0	3.2	1.4	0.0	1.6	1.8	0.0	3.8
J0009.0+0632	2.1	0.0	2.8	0.3	0.0	2.4	0.3	0.1	3.2	1.4	0.6	3.7	0.7	0.0	1.8
J0009.1+5030	0.9	0.0	0.3	0.4	0.1	6.0	1.5	0.2	9.6	5.9	1.1	10.6	1.9	0.6	7.0
J0009.9−3206	0.7	0.0	0.1	0.3	0.0	3.1	0.5	0.1	5.0	1.7	0.0	1.6	0.9	0.0	1.7
J0010.5+6556c	2.7	0.0	2.8	1.2	0.2	7.0	1.8	0.0	3.0	3.2	0.0	1.5	0.7	0.0	0.5
J0011.3+0054	1.3	0.0	0.8	0.3	0.1	4.9	0.5	0.1	4.4	1.9	0.0	2.0	0.6	0.0	0.0

Notes.
[a] In units of 10^{-8} photons cm^{-2} s^{-1}.
[b] In units of 10^{-9} photons cm^{-2} s^{-1}.
[c] In units of 10^{-10} photons cm^{-2} s^{-1}.

(This table is available in its entirety in a machine-readable form in the online journal. A portion is shown here for guidance regarding its form and content.)

100 MeV to 100 GeV in Table 4 are evaluated from the fit to the full band (see Section 3.5), rather than sums of band fluxes as in 1FGL. We do not present the integrated photon flux for 100 MeV to 100 GeV (see Section 3.5). Table 7 presents the fluxes in individual bands as defined in Section 3.5.

Figure 18 illustrates where the different classes of sources are located in the sky. Figure 19 shows where the broad classes of sources appear in the curvature–variability plane. This is similar to Figure 8 of Abdo et al. (2010f) although the two indicators were improved. Most "other" curved non-variable sources are tentatively associated with SNRs. The two "pulsars" above the variability threshold are the Crab and PSR J1142+01. The Crab mixes the pulsar and the nebula, and we know the variability is due to the nebula (Abdo et al. 2011c). PSR J1142+01 is a newly discovered millisecond pulsar with no known LAT pulsations.

4.2. Comparison with 1FGL

The 1FGL catalog (Abdo et al. 2010f) lists 1451 sources detected during the first 11 months of operation by the LAT. Associations between 2FGL and 1FGL sources are based on the following relation:

$$\Delta \leqslant d_x = \sqrt{\theta_{x_{1FGL}}^2 + \theta_{x_{2FGL}}^2}, \qquad (5)$$

where (Δ) is the angular distance between the sources and d_x is defined in terms of the semimajor axis of the $x\%$ confidence error ellipse for the position of each source, e.g., the 95% confidence error for the automatic source association procedure (Section 5.2). In total, 1099 2FGL sources were automatically associated with entries in the 1FGL catalog. At the level of overlapping 95% source location confidence contours the 2FGL catalog contains 774 (out of 1873) new γ-ray sources, while 352 sources previously listed in 1FGL do not have a counterpart in the 2FGL catalog.

The Galactic latitude distributions of the 2FGL sources, the 1FGL sources, and of the sources in common between the 1FGL and 2FGL catalogs, shown in Figure 20, indicate both

that most of the new 2FGL sources and most of the missing 1FGL sources are concentrated along the Galactic plane where the Galactic diffuse emission is most intense and improvements in the model for the diffuse emission since the 1FGL analysis would be expected to have the most influence (Section 2.2).

As described in Section 3.3, in the 2FGL analysis the spectral fits are made using PL, PL with an exponential cutoff, or log-parabola models. Of the 1099 1FGL sources associated with 2FGL sources, 274 of the brightest were fitted with a curved spectral functional form. For each 2FGL source we also evaluated the spectral index (Γ) of the best PL fit (Section 4.1) and this enables a comparison of the spectral characteristics of the 1FGL and 2FGL sources. Figure 21 shows the distributions of the spectral indices of all of the sources in the 1FGL and 2FGL catalogs. The two distributions are very similar, with an average $\Gamma_{1FGL} = 2.23 \pm 0.01$ and an average $\Gamma_{2FGL} = 2.21 \pm 0.01$. However, the peaks of the two distributions are not exactly coincident; also, the skewness of the 2FGL distribution is positive while it is negative for 1FGL. Figure 22 shows the distribution of the difference $\Gamma_{2FGL}-\Gamma_{1FGL}$ for the 1099 sources in common between the catalogs. The average of the distribution is -0.07 ± 0.01, with the 2FGL sources slightly harder than the 1FGL ones. This small difference in the spectral index distribution could be related to slightly difference uncertainties in the effective area between P7_V6 and P6_V3.

The distributions of the source significances reported in Figure 23 show that for the 2FGL catalog the significance peaks between 4σ and 5σ while for 1FGL the distribution shows a plateau between 4σ and 6σ; this indicates that 2FGL is more complete than 1FGL. Also, the distribution of the significance of the sources that are in common between 1FGL and 2FGL shows that most of the 1FGL sources that were not recovered in the 2FGL catalog had significance less than 7σ. In the remainder of this section we describe the variety of reasons that the additional 352 1FGL sources do not appear in the 2FGL catalog.

Table 8 lists 347 of the 1FGL sources that do not have a corresponding source in 2FGL. The five other 1FGL sources that do not appear in 2FGL were not included in the table
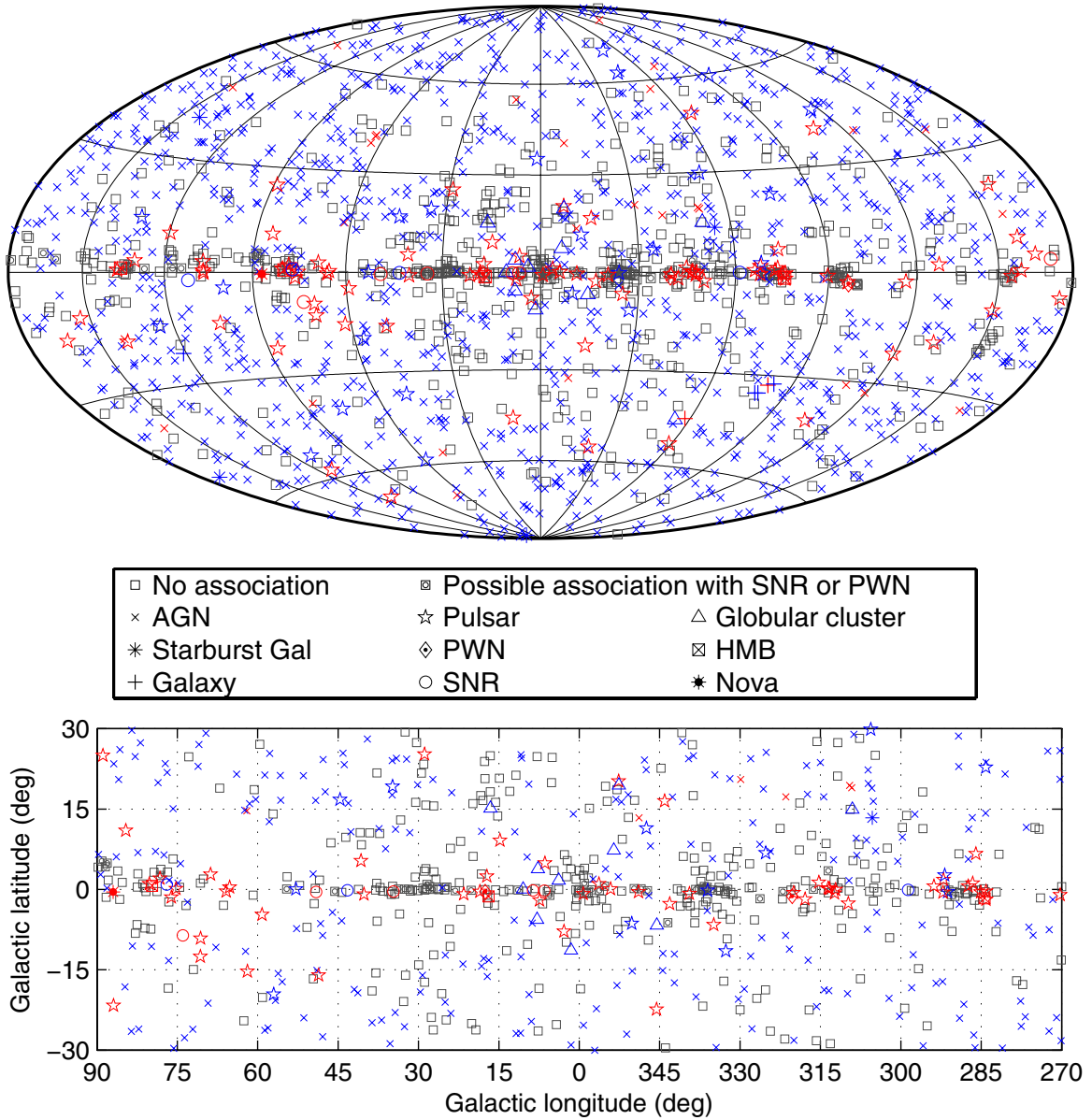
Figure 18. Full sky map (top) and blow-up of the inner Galactic region (bottom) showing sources by source class (see Table 6). Identified sources are shown with a red symbol, associated sources in blue.

because they were already replaced by an extended-source template in the 2FGL analysis. These sources are 1FGL J0523.3−6855 (2FGL J0526.6−6825e, LMC); 1FGL J1801.3−2322c (0FGL J1801.6−2327, 2FGL J1801.3−2326e, W28); 1FGL J1805.2−2137c (2FGL J1805.6−2136e, W30); 1FGL J1856.1+0122 (2FGL J1855.9+0121e, G034.7−00.4, W44); and 1FGL J1922.9+1411 (2FGL J1923.2+1408e, G049.2−00.7, W51C).

Some 1FGL sources near extended 2FGL sources remain in Table 8. An additional four 1FGL sources, 1FGL J0459.7−6921, 1FGL J0518.6−7222, 1FGL J0531.3−6716, and 1FGL J0538.9−6914, were also found in the LMC field, now replaced by an extended source in the 2FGL catalog analysis (J0526.6−6825e). Furthermore, the four 1FGL sources 1FGL J2046.4+3041, 1FGL J2049.1+3142, 1FGL J2055.2+3144, and 1FGL J2057.4+3057 distributed along the Cygnus Loop (G74.0−8.5), one of the most famous and well-studied SNRs, were replaced by an extended-source template in the 2FGL analysis (2FGL J2051.0+3040e), and so

are not confirmed in the 2FGL catalog. The extended source 2FGL J1824.5−1351e (HESS J1825−137) replaces two 1FGL sources: 1FGL J1821.1−1425c and 1FGL J1825.7−1410.

About 250 of the 347 sources are located on the Galactic plane or in other regions of bright, structured diffuse emission (see Figure 24). Of these, 88 have the "c" designation in the 1FGL name, which indicates that these sources were already recognized as possible spurious detections. Another 21 1FGL sources were flagged according to the definitions reported in Table 4 of Abdo et al. (2010f). These sources were also already noted as problematic. In the 1FGL catalog only 67 of the 347 sources have an association with a possible counterpart, mostly AGNs, while another 10 sources were associated with already known 0FGL (Abdo et al. 2009d) or 1AGL (Pittori et al. 2009) γ-ray sources.

In addition to the introduction of spatially extended sources in 2FGL, there are many possible causes for 1FGL sources to be absent from the 2FGL list. Among these are variability; different event selection used for the analysis (Pass 6 for 1FGL and Pass
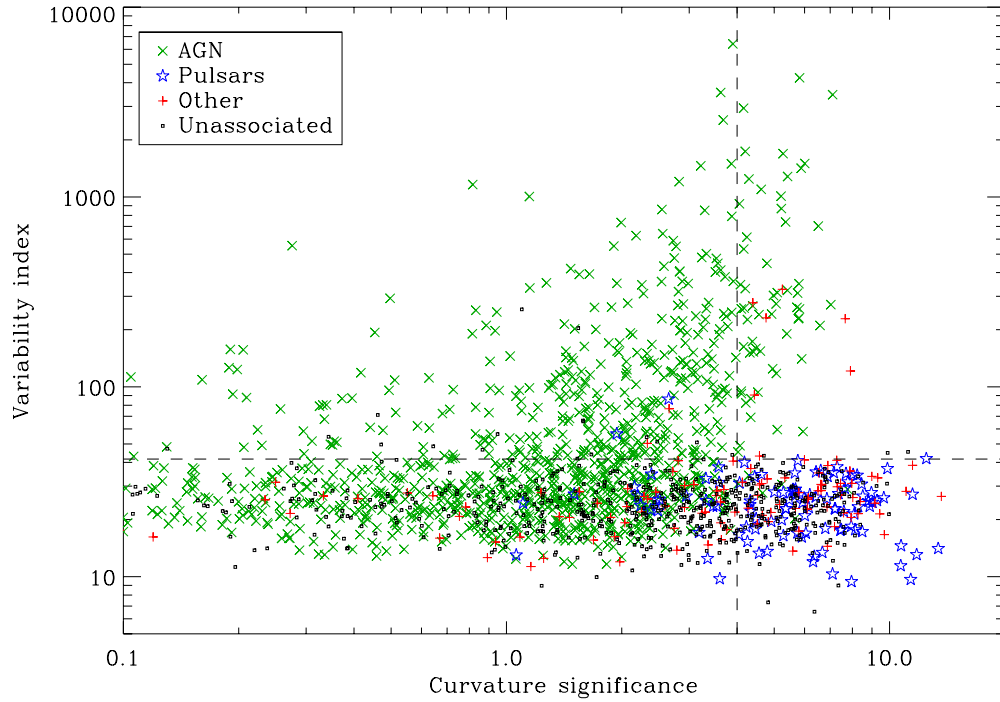
Figure 19. Variability index ($\mathrm{TS_{var}}$ in Section 3.6) plotted as a function of the curvature significance (`Signif_Curve` in Section 3.5) for different broad classes of sources. "AGN" here means any class starting with "ag" or "bz" in Table 6. The horizontal dashed line is set to 41.6, above which sources are likely variable. The vertical dashed line is set to 4.0, above which curved spectra are used.
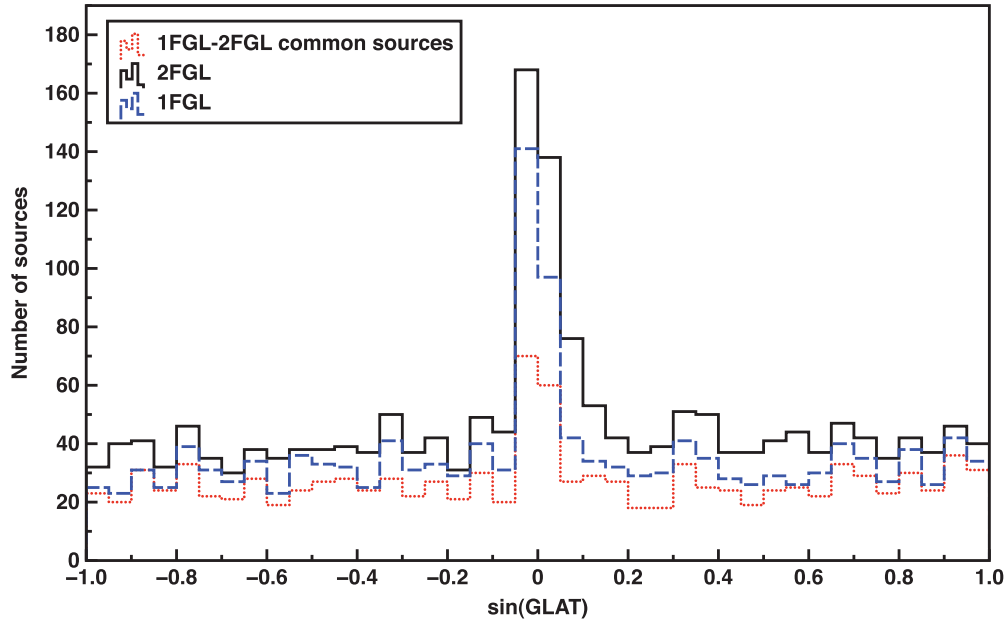
(A color version of this figure is available in the online journal.)

Figure 20. Distributions of the Galactic latitude of the 1FGL and 2FGL sources and of the sources in common between the 1FGL and 2FGL catalogs.

(A color version of this figure is available in the online journal.)

7 for 2FGL); different IRFs; different Galactic diffuse emission models; different analysis procedures (unbinned likelihood analysis for 1FGL and binned likelihood analysis for 2FGL); statistical threshold effects; and 1FGL sources resolved into two or more 2FGL sources. In the last columns of Table 8 we assigned to each source one or more flags corresponding to a possible cause. In many cases, no one reason can be singled out.

The numbers of associated sources between the 1FGL and 2FGL catalogs do depend on the criterion used to define spatial coincidence (Equation (5)). The number of 2FGL–1FGL

associated sources increases to 1151 if we use $\Delta < d_{99.9}$.[95] The 52 additional associations (see Table 8 and Figure 25) represent about the 5% of the 1451 1FGL sources, as expected when passing from d_{95} to $d_{99.9}$. Also, in 2FGL we used a better in-flight representation of the PSF that is broader than the PSF used in 1FGL at energies $E > 1$ GeV where, in general, most of the sources are detected. Furthermore, the new and improved model

---

[95] Assuming a Rayleigh distribution for the source angular separations, $d_{99.9}$ is evaluated using $\theta_{99.9} = 1.52\,\theta_{95}$.
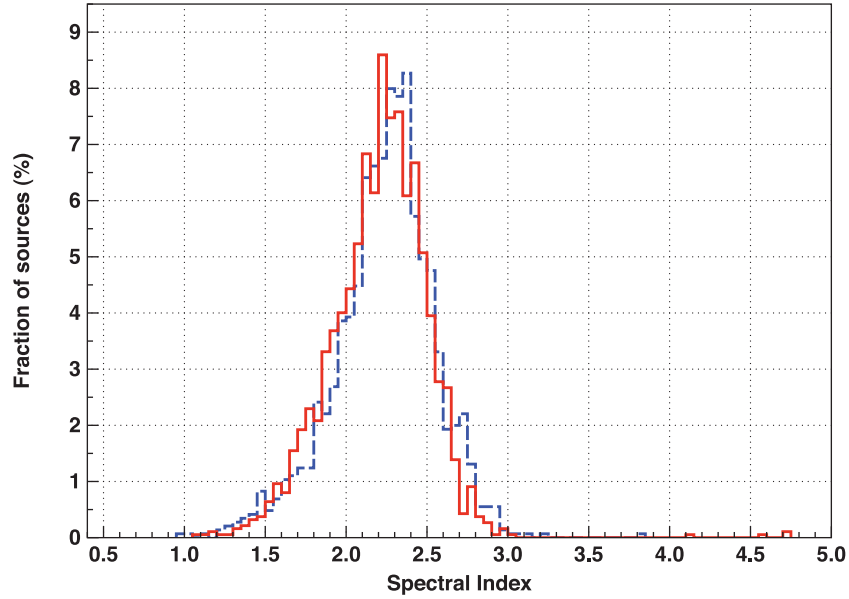
Figure 21. Distributions of the spectral index for the 1FGL (1451 sources, dashed line) and for the 2FGL (1873 sources, solid line) catalogs.

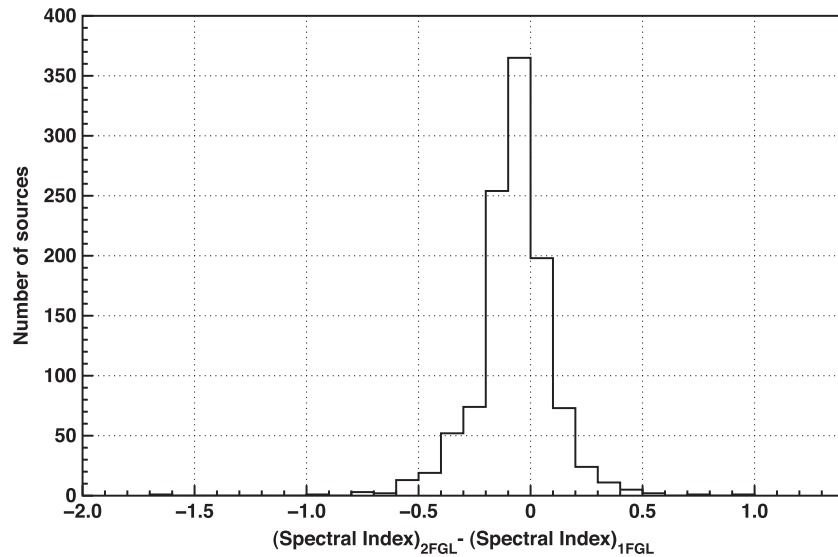(A color version of this figure is available in the online journal.)

Figure 22. Distribution of the difference $\Gamma_{2FGL} - \Gamma_{1FGL}$ for the 1099 sources in common between the 1FGL and 2FGL catalogs.

of the Galactic diffuse emission used to build the 2FGL catalog together with the expected increase of the signal-to-noise ratio due to the use of 24 months data, allowed us to obtain a better localization of the sources at positions that might be outside the 95% confidence error regions previously reported in 1FGL. Indeed, most of the 52 additional associations concern sources located along the Galactic plane and in regions like Orion and Ophiuchus, while only about 10 were associated in regions with low diffuse emission.

Also, in the 1FGL catalog the positions of sources associated with the LAT-detected pulsars and X-ray binaries are the high-precision positions of the identified sources. (These sources can be easily recognized because they have null values in the localization parameters reported in the 1FGL catalog). Not all of these associations appear in the 2FGL catalog because they cannot be associated using d_{95}, but some are listed in Table 8 because they can be associated using $d_{99.9}$. These sources are 1FGL J2032.4+4057 (Cyg X−3); 1FGL J1836.2+5925 (LAT PSR

J1836+5925); and 1FGL J1124.6−5916 (PSR J1124−5916). However, 1FGL J1741.8−2101 (LAT PSR J1741−2054), 1FGL J1614.0−2230 (PSR J1614−2230), and 1FGL J1747.2−2958 (PSR J1747−2958) are still not associated, and for these sources we report the nearest 2FGL source (see, e.g., Figure 26). The last missing source in this category is 1FGL J1023.0−5746 (LAT PSR J1023−5746). It was resolved into two 2FGL sources, 2FGL J1022.7−5741 and 2FGL J1023.5−5749. Although both are located very close to the pulsar position, they cannot be formally associated using $d_{99.9}$.

Several other 1FGL sources were also split into more than one candidate source seed ("S" in the Flags column of Table 8). In some cases only one of the two seeds reached a TS > 25 and so was included in the 2FGL list (see Figure 27). Another example of splitting is 1FGL J1642.5+3947 that was tentatively associated with the blazar 3C 345 in Abdo et al. (2010r, ; 1LAC) paper. This source has no 2FGL counterpart, because it is now resolved into two sources: 2FGL J1642.9+3949 associated with
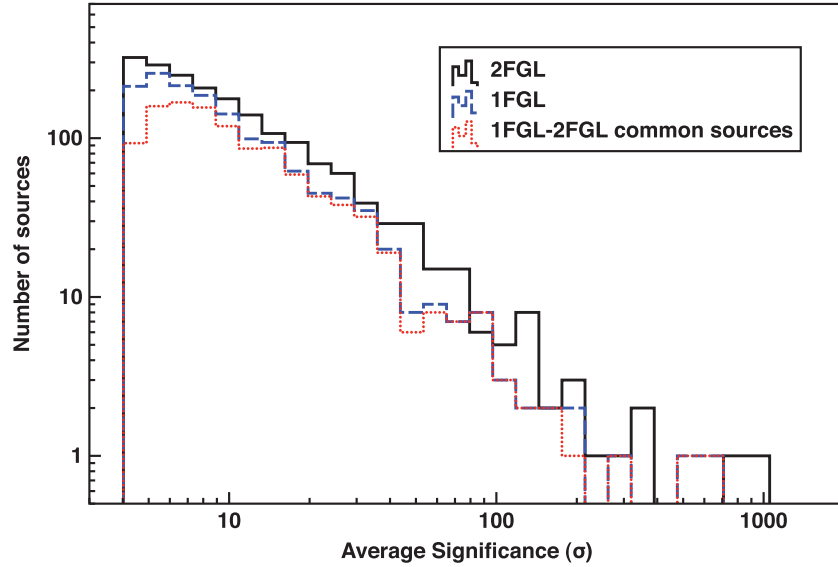
Figure 23. Distributions of the significances of the sources in the 1FGL and 2FGL catalogs and of the sources in common between the catalogs. The distribution of the significance for the 1FGL–2FGL common sources is based on the values reported in the 1FGL catalog.

(A color version of this figure is available in the online journal.)

Table 8
List of 1FGL Sources Not in the 2FGL Catalog

1FGL	1FGL Assoc.[a]	l[a] (deg)	b[a] (deg)	θ_{95}[a] (deg)	σ[a]	Γ_{25}[a]	Var[a] ($p > 90\%$)	2FGL[b] ($\Delta < d_{99.9}$)	2FGL[c] ($d_{99.9} < \Delta < 1°$)	Δ[d] (deg)	$\Delta / d_{99.9}$	2FGL[e] Seed	Flags[f]
J0000.8+6600c	. . .	117.812	3.635	0.112	9.8	2.60	. . .	. . .	J2359.6+6543c	0.298	1.241	. . .	S
J0006.9+4652	. . .	115.082	−15.311	0.194	10.2	2.55	T	. . .	J0007.8+4713	0.381	1.249	T	S
J0008.3+1452	. . .	107.655	−46.708	0.144	4.7	2.00	. . .	. . .	. . .	. . .	. . .	T	C
J0013.7−5022	BZB J0014−5022	317.624	−65.666	0.151	4.4	2.23	. . .	. . .	. . .	. . .	. . .	T	C
J0016.6+1706	. . .	111.135	−44.964	0.197	4.7	2.57	. . .	. . .	. . .	. . .	. . .	. . .	NC
J0019.3+2017	PKS 0017+200	112.787	−41.944	0.203	5.9	2.38	. . .	. . .	. . .	. . .	. . .	T	C
J0028.9−7028	. . .	305.664	−46.535	0.172	6.3	2.19	. . .	J0029.2−7043	. . .	0.253	0.704	T	C
J0038.6+2048	. . .	118.912	−41.969	0.146	4.6	1.63	. . .	. . .	. . .	. . .	. . .	. . .	NC
J0041.9+2318	PKS 0039+230	120.104	−39.515	0.221	5.0	2.52	. . .	. . .	. . .	. . .	. . .	T	C
J0059.6+1904	. . .	125.615	−43.751	0.091	5.8	2.39	. . .	. . .	. . .	. . .	. . .	. . .	BC
J0110.0−4023	. . .	287.889	−76.190	0.085	4.2	1.34	. . .	. . .	. . .	. . .	. . .	T	C
J0122.2+5200	. . .	127.740	−10.571	0.168	4.1	2.18	. . .	. . .	. . .	. . .	. . .	T	C
J0136.3−2220	. . .	190.201	−78.746	0.113	4.6	1.60	. . .	. . .	. . .	. . .	. . .	. . .	BC
J0147.4+1547	. . .	142.143	−44.981	0.119	4.9	1.81	. . .	. . .	. . .	. . .	. . .	T	C
J0202.1+0849	RX J0202.4+0849	150.851	−50.172	0.120	4.5	1.97	. . .	. . .	. . .	. . .	. . .	T	C

Notes.

[a] All the values reported in these columns are from the 1FGL catalog (Abdo et al. 2010f).

[b] Name of the 2FGL source associated with the 1FGL one using $d_{99.9}$.

[c] Closest 2FGL source having a distance $d_{99.9} < \Delta < 1°$ from the position of the 1FGL source. The 2FGL name is also reported if the 1FGL source and one or more seeds have overlapping $\theta_{99.9}$ error regions but cannot be associated with any seed on the basis of the criterium $\Delta < d_{99.9}$.

[d] The angular separation (Δ) between the 1FGL source and the 2FGL sources associated using $d_{99.9}$ or the closest 2FGL source.

[e] T: the 1FGL source and one of the 2FGL list of initial seeds have an angular separation $<d_{99.9}$.

[f] C: confirmed 1FGL sources. LMC, Orion, Carina, and Ophiuchus indicate that the source is in a region of the sky with high diffuse emission and high density of close sources; NC = not confirmed 1FGL sources (see the text); BC = 1FGL sources confirmed by the 11 month binned likelihood analysis; S: the 1FGL source was split/resolved in one or more seeds; O: overlapping $\theta_{99.9}$ error regions with one or more seeds; V: variable source visible only in the first 11 months; Sun: the source was detected when the Sun was at an angular distance $<1°$ and the light curve shows just a flare in the time bin relative to the passage of the Sun close to the position of the source.

(This table is available in its entirety in a machine-readable form in the online journal. A portion is shown here for guidance regarding its form and content.)

3C 345 and 2FGL J1640.7+3945 associated with NRAO 512. Other 1FGL sources have overlapping $\theta_{99.9}$ source location uncertainty regions with one or more 2FGL sources or seeds and have the "O" flag in Table 8 (see Figure 28).

Another major reason for sources to disappear between 1FGL and 2FGL is a change in the calculated significance. As described in Section 3.1.3, the 2FGL catalog was built starting from 3499 seeds with TS > 10 in the *pointlike* analysis. The final *gtlike* analysis, which did not change the positions of the seeds, resulted in the 1873 sources with TS > 25 that make up the 2FGL catalog. Among the other seeds that did not reach the threshold, 104 can be associated with 1FGL sources (using $\Delta < d_{99.9}$). These sources, marked with a "C" in the flags column of the table, can be considered to be confirmed sources whose
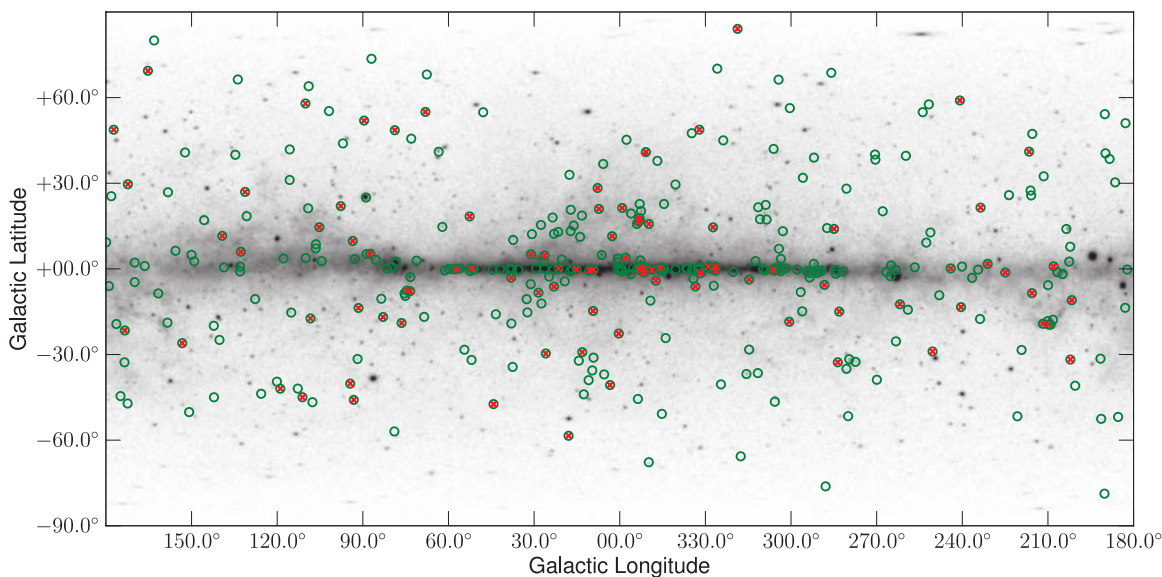
Figure 24. All-sky map for energies >1 GeV indicating the positions of the 1FGL sources that are not in the 2FGL catalog (green circles). The red crosses indicate the sources having the flag "NC" in Table 8.

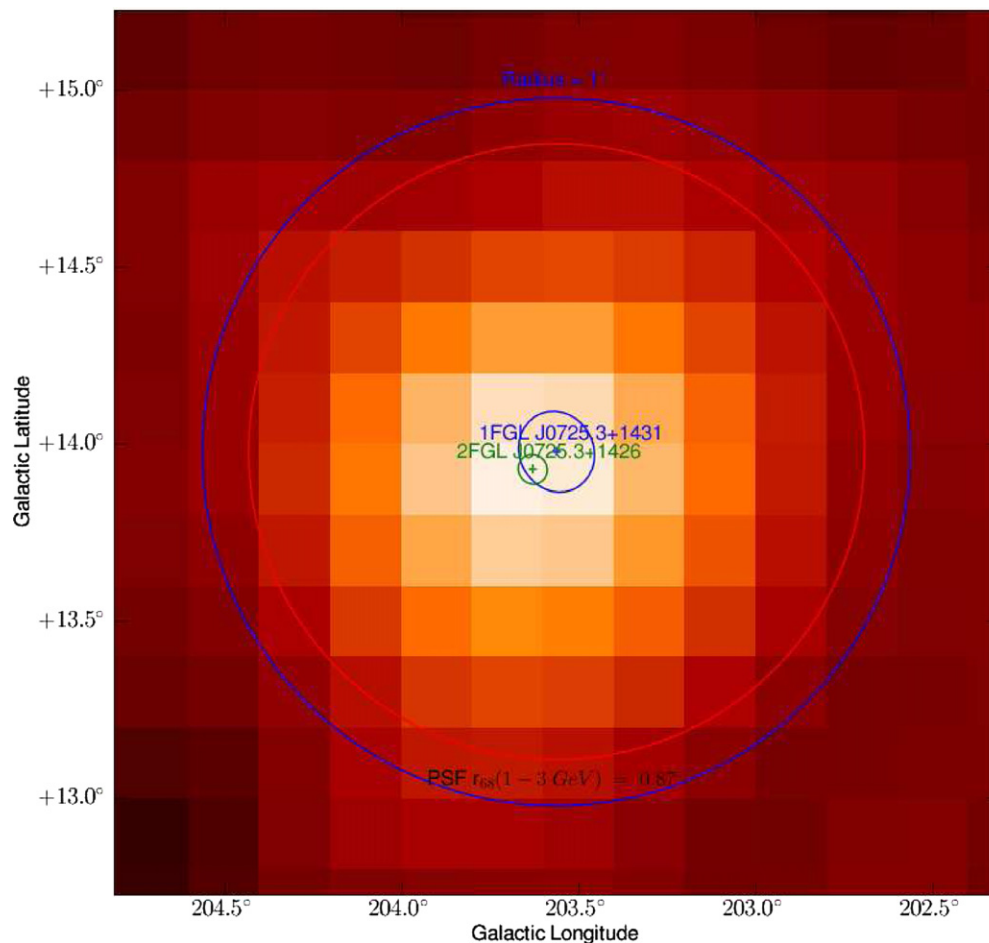(A color version of this figure is available in the online journal.)

Figure 25. Typical example of a 1FGL source associated with a 2FGL source using $d_{99.9}$. The $E > 1$ GeV counts map (1 pixel = 0°.2) was smoothed using a Gaussian kernel ($\sigma = 3$ pixels). The ellipses represent the 99.9% confidence error regions.

(A color version of this figure is available in the online journal.)
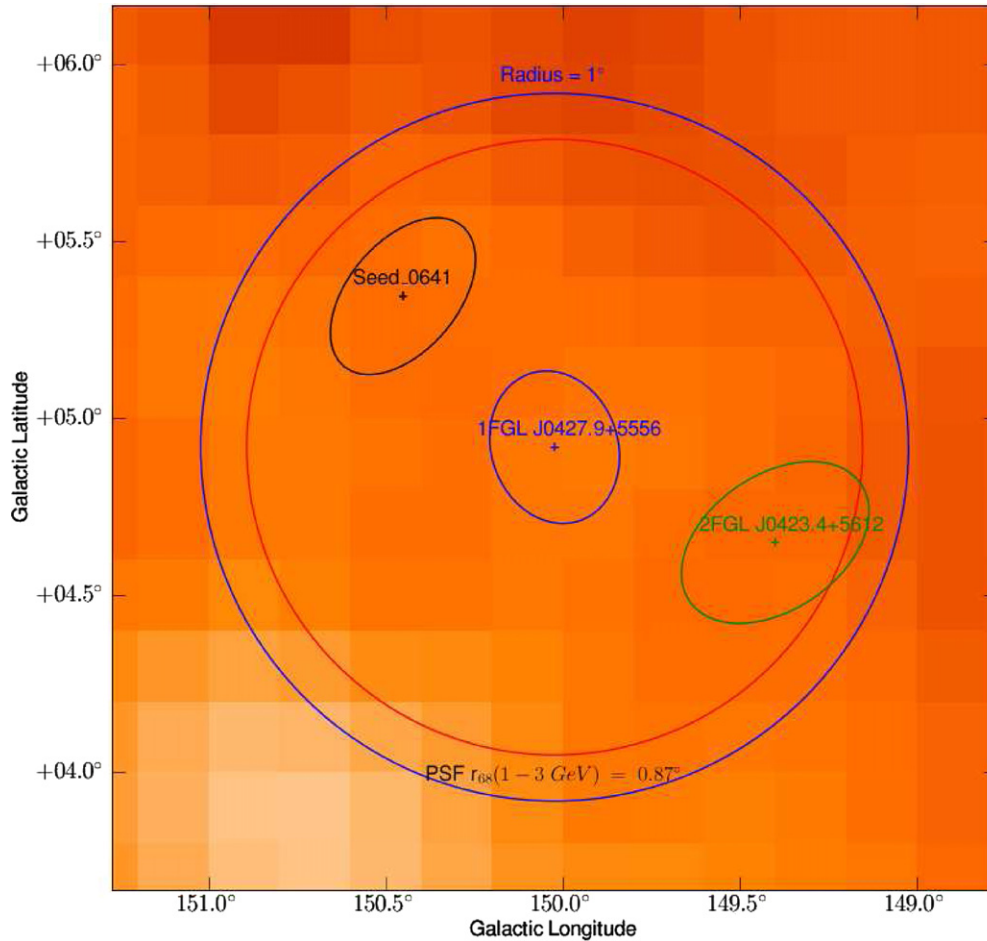
Figure 26. Typical example of a 1FGL and a 2FGL source having an angular separation greater than $d_{99.9}$ but less than $1°$. In this particular case there is also a seed (candidate source considered in the 2FGL analysis) separated by less than $1°$ from the 1FGL source. The $E > 1$ GeV counts map (1 pixel = $0°.2$) was smoothed using a Gaussian kernel ($\sigma = 3$ pixels). The ellipses represent the 99.9% confidence error regions.

(A color version of this figure is available in the online journal.)

significance dropped below the threshold, either as a result of time variability, change in the diffuse model, or the shift from unbinned to binned likelihood in the catalog analysis procedure.

In order to quantify the effect of changing *gtlike* from unbinned to binned mode, we performed a new binned analysis of the original 11 month data set, using the P6V3 Diffuse IRFs and the same Galactic diffuse emission model as used for the 1FGL analysis. The analysis also started using the same 1499 seeds that were used as input to the 1FGL run (see Abdo et al. 2010f). This analysis confirmed with TS > 25 1138 sources of the 1451 sources that were in the 1FGL catalog. Among these confirmed sources are 168 1FGL sources that are not present in 2FGL, but were still detected at TS> 25 using the binned analysis for the 11 month data set. In Table 8 the sources confirmed by the binned analysis but not included among the 3499 seeds have the flag "BC." In the 1FGL catalog, only five of the "BC" sources were found to be variable with probabilities $p > 90\%$ (see the "Var" column in Table 8). Since the shift from unbinned to binned analysis has been excluded as a cause for these, their disappearance must be attributed to time variability or, more likely, to change in the diffuse emission model.

The 102 sources that were no longer detected in either the binned likelihood re-analysis of the 11 month data set nor in any of the other all-sky analyses performed using data collected between 11 and 24 months are considered not confirmed 1FGL sources ("NC" in the Flags column of Table 8). Among these sources, nine were bright during just the first months of the mission and are reported with the flag V (variable) in Table 8. They are all associated with AGNs, mostly blazars. An example is 1FGL J1122.9−6415, associated with PMN J1123−6417 and included in the 0FGL list (Abdo et al. 2009d), which after a flare in 2008 September was not significantly detected again until 2011 May (D'Ammando 2011).

Four "NC" 1FGL sources have angular distances less than $1°$ from the ecliptic ("Sun" in the Flags column of Table 8). Their light curves, which are similar to that shown in Figure 13, show significant detections of the sources only during the passage of the Sun. For the other 89 "NC" sources their non-associations with the 2FGL sources can be ascribed to a combination of different effects that cannot be easily disentangled.

Most of these sources are located close to regions of enhanced diffuse emission (see Figure 24) and about 20 of them were already flagged as sources influenced by the diffuse emission in the 1FGL catalog. Also, the fact that these sources were not confirmed in the binned analysis of the 11 month data can be related to statistical fluctuation in the number of the sources detected close to the significance threshold. Figure 29 shows the distribution of the source significances, as reported in 1FGL, for the 89 non-confirmed 1FGL sources and for the 1099 1FGL sources present in the 2FGL catalog. Most of the non-confirmed
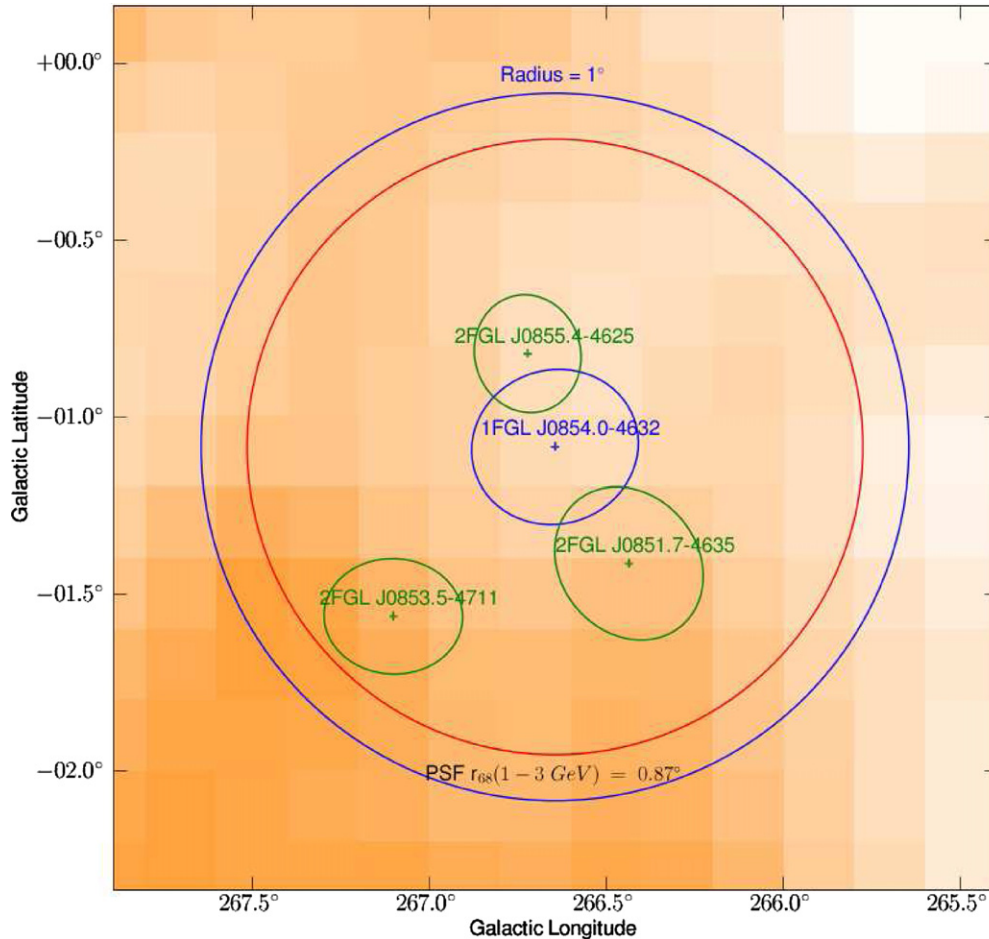
Figure 27. Typical example of a 1FGL source that was split in two 2FGL sources. The $E > 1$ GeV counts map (1 pixel = $0\overset{\circ}{.}2$) was smoothed using a Gaussian kernel ($\sigma = 3$ pixels). The ellipses represent the 99.9% confidence error regions.

(A color version of this figure is available in the online journal.)

sources have significances less than 6σ, which is very close to the threshold ($\sim 4\sigma$) adopted in 1FGL and 2FGL catalogs. These sources are intrinsically faint and for several of them the energy flux reported in the 1FGL catalog is just an upper limit. Furthermore, the significance values returned by the unbinned likelihood analysis by definition should be intrinsically higher than those returned by the binned analysis. Thus, most of the 89 sources were above the threshold in the original unbinned 1FGL analysis, but not in the binned analysis.

5. SOURCE ASSOCIATION AND IDENTIFICATION

5.1. Firm Identifications

As with the LAT Bright Source List (Abdo et al. 2009d) and 1FGL catalog (Abdo et al. 2010f), we retain the distinction between associations and firm identifications. Although many associations, particularly those for AGNs, have very high probability of being true, a firm identification, shown in the catalog by capitals in the Class column in Table 6, is based on one of three criteria.

1. *Periodic variability*. Pulsars are the larger class in this category. All PSR labels indicate that pulsed γ-rays have been seen from the source with a probability of the periodicity occurring by chance of less than 10^{-6}. A similar chance probability requirement applies to the other set of periodic sources, the high-mass binaries (HMBs). Four of

these are included in the catalog: LS I +61 303 (Abdo et al. 2009c), LS 5039 (Abdo et al. 2009e), Cygnus X-3 (Abdo et al. 2009f), and 1FGL J1018.6−5856 (Corbet et al. 2011).

2. *Spatial morphology*. Spatially extended sources whose morphology can be related to the extent seen at other wavelengths include SNR, PWNe, and galaxies, as described in Section 3.4. The Centaurus A lobes and core are both marked as identified, because they are part of the same extended source, although the core itself does not show spatial extent. As noted in Section 3.8, additional extended sources are being found but are not listed in the catalog as firm identifications, because they were analyzed as point sources for this work. Although individual molecular clouds could in principle be included in this list, the catalog construction incorporates most known clouds into the diffuse model, and so no sources of this type are identified in the catalog.

3. *Correlated variability*. Variable sources, primarily AGNs, whose γ-ray variations can be matched to variability seen at one or more other wavelengths, are considered to be firm identifications. Although some cases are well documented, such correlated variability is not always easily defined. We conservatively require data in more than two energy bands for comparison. Finding a blazar to have a high X-ray flux at the same time as a γ-ray flare, for example, does not qualify if there is no long-term history for the X-ray emission. We include those sources whose variability properties are documented either in papers or with Astronomer's
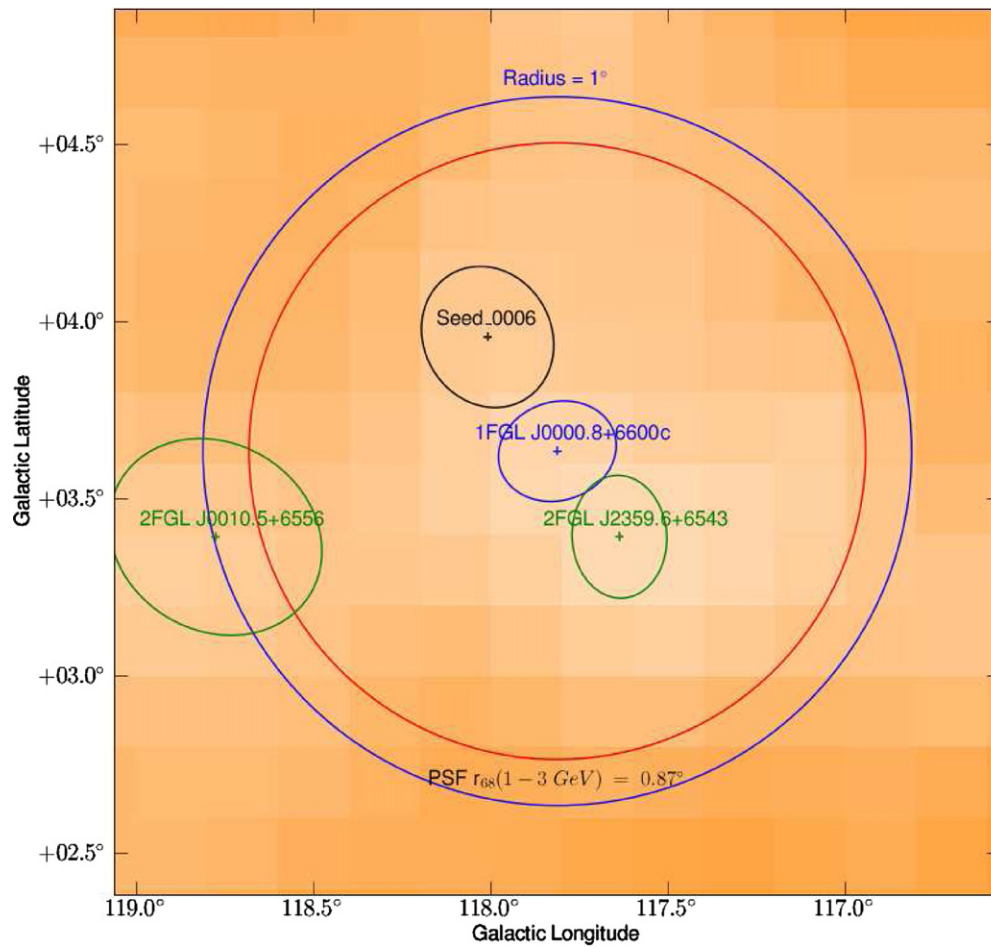
Figure 28. Typical example of a 1FGL source and a 2FGL source having overlapped 99.9% confidence error regions. In this particular case there is also a seed (candidate source considered in the 2FGL analysis) very close to the 1FGL source and we cannot exclude the possibility that the 1FGL source was split into two seeds. The $E > 1$ GeV counts map (1 pixel = $0°.2$) was smoothed using a Gaussian kernel ($\sigma = 3$ pixels). The ellipses represent the 99.9% confidence error regions.

(A color version of this figure is available in the online journal.)
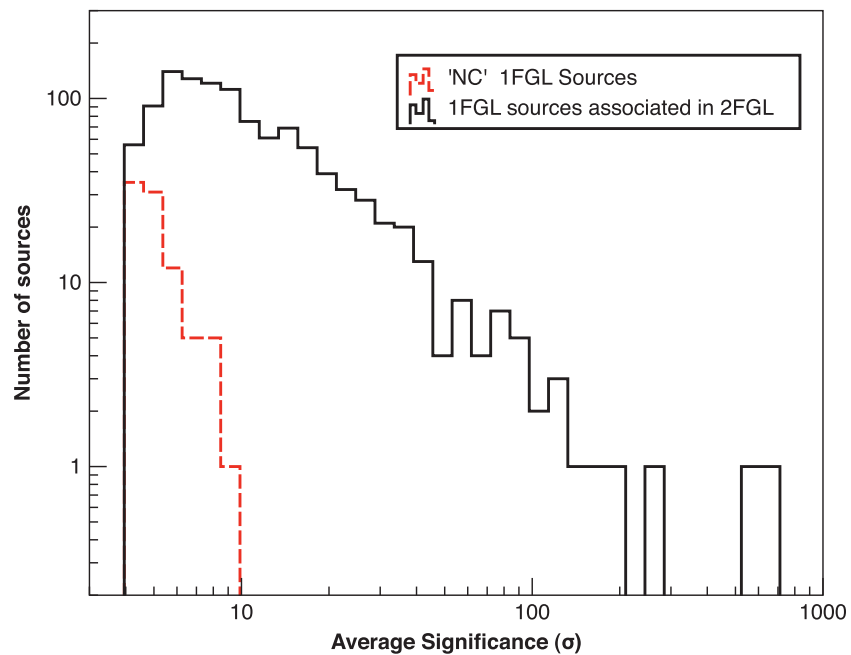

Figure 29. Distribution of the significances of the unconfirmed 1FGL sources and of the 1FGL sources associated with sources in the 2FGL catalog.

(A color version of this figure is available in the online journal.)

Table 9
Catalogs Used for the Automatic Source Association

Name	Objects	P_{prior}	N_{ass}	N_{false}	$\langle \hat{N}_{false} \rangle$	Ref.
High $\dot{E}/d^2$ pulsars	213	0.037	29	0.9	1.0	2
Other normal pulsars	1657	0.011	12	0.6	0.7	2
Millisecond pulsars	137	0.014	45	0.3	0.4	2
Pulsar wind nebulae	69	0.009	25	0.5	0.6	1
High-mass X-ray binaries	114	0.003	2	0.1	0.2	3
Low-mass X-ray binaries	187	0.007	3	0.3	0.3	4
Point-like SNR	157	0.019	6	0.7	0.3	5
Extended SNR[†]	274	n.a.	92	n.a.	39.7	5
O stars	378	0.005	1	0.2	0.2	6
WR stars	226	0.005	0	0	0.2	7
LBV stars	35	0.001	1	<0.1	0.2	8
Open clusters	2140	0.005	0	0	0.2	9
Globular clusters	160	0.028	11	0.5	0.6	10
Dwarf galaxies[†]	14	n.a.	7	n.a.	3.4	1
Nearby galaxies	276	0.014	5	0.4	0.4	11
IRAS bright galaxies	82	0.021	6	0.2	0.2	12
BZCAT (Blazars)	3060	0.341	691	7.4	6.9	13
BL Lac object	1371	0.170	278	2.8	2.6	14
AGN	10066	0.009	8	0.3	0.4	14
QSO	129853	0.196	197	6.7	6.7	14
Seyfert galaxies	27651	0.028	29	2.0	1.9	14
Radio loud Seyfert galaxies	29	0.001	4	<0.1	<0.1	1
CGRaBS	1625	0.258	352	3.8	4.1	15
CRATES	11499	0.341	634	17.7	17.8	16
VLBA Calibrator Source List	5776	0.258	623	11.8	12.0	17
ATCA 20 GHz southern sky survey	5890	0.296	335	10.3	10.6	18
TeV point-like source catalog*	61	n.a.	47	n.a.	0.6	19
TeV extended source catalog[†]	57	n.a.	48	n.a.	20.1	19
First AGILE catalog*	47	n.a.	57	n.a.	21.1	20
Third EGRET catalog*	271	n.a.	116	n.a.	31.0	21
EGR catalog*	189	n.a.	69	n.a.	11.4	22
0FGL list*	205	n.a.	185	n.a.	5.1	23
1FGL catalog*	1451	n.a.	1099	n.a.	18.1	24
LAT pulsars	87	n.a.	80	n.a.	1.4	1
LAT identified	44	n.a.	43	n.a.	0.7	1

References. (1) Collaboration internal; (2) Manchester et al. 2005; (3)Liu et al. 2006; (4) Liu et al. 2007; (5) Green 2009; (6) Maíz-Apellániz et al. 2004; (7) van der Hucht 2001; (8) Clark et al. 2005; (9) Dias et al. 2002; (10) Harris 1996; (11) Schmidt et al. 1993; (12) Sanders et al. 2003; (13) Massaro et al. 2009; (14) Véron-Cetty & Véron 2010; (15) Healey et al. 2008; (16) Healey et al. 2007; (17) http://www.vlba.nrao.edu/astro/calib/vlbaCalib.txt; (18) Murphy et al. 2010; (19) http://tevcat.uchicago.edu/; (20) Pittori et al. 2009; (21) Hartman et al. 1999; (22) Casandjian & Grenier 2008; (23) Abdo et al. 2009d; (24) Abdo et al. 2010f.

Telegrams. This list does not represent the result of a systematic study. Ongoing work will undoubtedly enlarge this list. The one Galactic source identified in this way is nova V407 Cygni (Abdo et al. 2010m).

We include one exception to these rules. The Crab PWN is listed as a firm identification even though it does not meet any of these criteria. The well-defined energy spectrum distinct from the Crab pulsar spectrum and matching spectra seen at both lower and higher energies provides a unique form of identification (Abdo et al. 2010i).

In total, we firmly identify 127 out of the 1873 2FGL sources. Among those, 83 are pulsars, 28 are AGNs, 6 are SNRs, 4 are HMBs, 3 are PWNe, 2 are normal galaxies, and one is a nova (Table 6).

5.2. Automated Source Associations

Our approach for automated source association closely follows that used for the 1FGL catalog, and details of the method are provided in Abdo et al. (2010f). In summary, we use a Bayesian approach that trades the positional coincidence of possible counterparts with 2FGL sources against the expected number of chance coincidences to estimate the probability that a specific counterpart association is indeed real (i.e., a physical association). As for 1FGL, we retain counterparts as associations if they reach a posterior probability of at least 80%.

We apply this method to a set of counterpart catalogs for which we calibrate the prior source association probabilities using Monte Carlo simulations of fake 2FGL catalogs. In comparison to 1FGL, for which we made 100 independent simulations for each catalog, we adapted the number of simulations (between 100 and 1000) so that the relative accuracy in the expected false association rate is determined to better than 5% for each catalog. This improved the precision of our probability computations for catalogs that have only few associations with 2FGL sources. The prior probabilities adopted for each catalog are listed in Table 9.

Another improvement with respect to 1FGL concerns the estimation of the local counterpart densities ρ_k. For 1FGL, we

estimated these densities from the number of objects in the counterpart catalog within a radius of 4° around the location of the 1FGL source of interest. For counterpart catalogs containing strong density variations on smaller scales (e.g., O stars, Wolf-Rayet (W–R) stars, and luminous blue variable (LBV) stars) this choice led to an underestimate of the actual source densities in these regions, which in turn resulted in overestimations of the association probabilities (see discussion in Abdo et al. 2010f). For 2FGL we estimate the source densities in each counterpart catalog using an all-sky map which we implemented as a HEALPix grid with resolution $N_{side} = 512$, corresponding to an angular resolution of about 6′, with the objects of each counterpart catalog binned in this grid. We removed sparseness of the binning and attenuated the statistical fluctuations by applying a spherical Gaussian smoothing kernel with width adjusted adaptively so that at least three sources contributed to the density estimate at each grid location.

For certain counterpart catalogs the Bayesian method could not be applied since either (1) the location uncertainty of the counterpart is larger than the location uncertainty of the 2FGL source (these catalogs are indicated by * in Table 9) or (2) the counterpart is an extended source (these catalogs are indicated by † in Table 9). In the first case, we consider as potential associations all objects for which the separation from the 2FGL source is less than the quadratic sum of the 95% confidence error radii. (For elliptical error regions we take the semimajor axis as the error radius.) In the second case, we assume that the counterparts have circular extensions and consider all objects as associations for which the extension circle overlaps with the 95% confidence error radius of the 2FGL source, with the semimajor axis of the 2FGL source location ellipse again taken as the error radius.

The list of catalogs used in the automatic association is summarized in Table 9, organized into four categories: (1) catalogs of known or plausible γ-ray-emitting source classes, (2) catalogs of surveys at other frequencies, (3) catalogs of GeV sources, and (4) catalogs of identified γ-ray sources. The first category allows us to assign 2FGL sources to object classes, while the second category reveals multiwavelength counterparts that may suggest the possible nature of the associated 2FGL source. The third category allows assessment of former GeV detections of 2FGL sources, and the fourth category keeps track of all firm identifications (cf. Section 5.1). For this last category we claim associations based on the spatial overlap of the true counterpart position with the 2FGL 99.9% confidence error ellipse.

With respect to 1FGL, we updated all catalogs for which more comprehensive compilations became available. We now use the 13th edition of the Veron catalog (Véron-Cetty & Véron 2010), version 20 of BZCAT[96] (Massaro et al. 2009), and version 1.40 of ATNF (Manchester et al. 2005) that we augmented with 158 recently detected pulsars that are not yet in the ATNF database, the 2010 December revision of the Globular Cluster database (Harris 1996) that we augmented with three recently detected clusters, version 3.1 of the Open Cluster catalog (Dias et al. 2002), the 2010 December 5 version of the VLBA Calibrator Source List,[97] and the most recent version of the TeVCat catalog.[98] We also added new counterpart catalogs: the Australia Telescope 20 GHz Survey (Murphy et al. 2010) and the IRAS

Revised Bright Galaxy Sample (Sanders et al. 2003), from which we selected all sources with 100 μm fluxes brighter than 50 Jy. The latter catalog replaces the starburst catalog used for 1FGL.

Following the philosophy for 1FGL, we split our pulsar catalog into normal pulsars and millisecond pulsars (MSPs) by requiring $\log \dot{P} + 19.5 + 2.5 \times \log P < 0$ for the latter. Because globular clusters are classified by a separate catalog and the LAT is unable to spatially resolve individual MSPs in globular clusters, we removed all globular cluster MSPs from the pulsar catalog. We furthermore collect normal pulsars with $\dot{E}/d^2 > 5 \times 10^{32}$ erg kpc^{-2} s^{-1} into a separate counterpart catalog to specifically select energetic and nearby pulsars that are more likely potential γ-ray sources. The value separating these classes corresponds to the lowest $\dot{E}/d^2$ found among all LAT identified pulsars. We also split off point-like SNRs from the Green catalog (Green 2009) by selecting all objects with diameters <20′. In parallel, we use the full Green catalog for finding matches with potentially extended SNRs. Furthermore, we divided the TeVCat catalog into point-like and extended sources by selecting for the latter all sources with extension radius > 0.

We also searched for associations using the Atlas of Radio/X-ray associations with optical objects (Flesch 2010) from which we selected those objects that have stellar, radio, and X-ray associations (Cl = SRX), the Planck Early Release Catalogs (Ade et al. 2011b), the fourth IBIS catalog (Bird et al. 2010), and the *Swift*-BAT 58-Month Survey (Baumgartner et al. 2010), yet as these did not reveal any new reliable and plausible counterpart that has not already been found in one of the other catalogs, we did not include these catalogs in our final results.

5.2.1. Automated Association Summary

The results of the automated association procedure for each of the external catalogs are summarized in Table 9. For each catalog we quote the name (Column 1), the number of objects in the catalog (Column 2), the prior probability assigned by our calibration procedure (Column 3), and the number N_{ass} of associations that have been found between 2FGL sources and counterpart objects (Column 4). Note that a given 2FGL source may have counterparts in multiple catalogs, and a given object in a counterpart catalog may have multiple associated 2FGL sources (which may arise if the object is spatially extended or if it has a large location uncertainty). Consequently, the sum of the N_{ass} column considerably exceeds the total number of associated 2FGL sources. Using the posterior probabilities P_{ik} that we derive by the Bayesian method for all associations i in a counterpart catalog k, we compute the expected number of false associations using $N_{false} = \sum_{P_{ik}} (1 - P_{ik})$ (Column 5). To validate that these estimates are accurate (and thus that our prior probability calibration was precise), we alternatively estimate the number of false associations $\langle \hat{N}_{false} \rangle$ using Monte Carlo simulations of 100 fake 2FGL catalogs (Column 6); we refer to Abdo et al. (2010f) for a detailed description of the simulation procedure. For all catalogs we find $N_{false} \simeq \langle \hat{N}_{false} \rangle$ which confirms that the posterior probabilities computed by the automatic association procedure are accurate.

In total, we find that 1141 of the 1873 sources in the 2FGL catalog (61%) have been associated with a least one non-GeV γ-ray counterpart by the automated procedure. Among those, 123 sources (11%) are firmly identified objects, 790 (69%) are associated with at least one object of known type, and 228 (20%) have counterparts only in the multiwavelength catalogs. For the remaining 732 sources in the 2FGL catalog that have no

non-GeV γ-ray counterpart, 322 sources (44%) are associated with former GeV detections, and 410 sources (56%) are new GeV sources.

Among the 2FGL sources that are not firmly identified, 940 (92%) have been associated using the Bayesian method at the 80% confidence level, while 78 (8%) have been associated based on overlap of the error regions or source extents and have lower confidence (catalogs based on spatial overlap are indicated by † in Table 9). From simulations we expect that 43 of the 940 sources (5%) that were associated with the Bayesian method are chance coincidences. Among the 78 sources that were associated based on overlap, the expected number of chance coincidences amounts to 55 (71%), demonstrating that these associations are considerably less reliable. Due to this large false positive rate, we do not claim any associations based on overlap in our final catalog. We record, however, any spatial overlap with a TeV source in the FITS file version of the catalog, and use a special flag in our catalog (TEVCAT_FLAG), distinguishing point-like (P) from extended (E) TeV counterparts (see Appendix C). We furthermore list all unidentified 2FGL sources that are spatially overlapping with SNRs in Table 11. Finally, 2FGL sources spatially overlapping with the LMC that are not associated with any object in one of the other counterpart catalogs are indicated as *LMC field*.

5.2.2. Active Galactic Nucleus Associations

AGNs, and in particular blazars, are the most prominent class of associated sources in 2FGL. In total, our automatic association procedure finds 917 2FGL sources that are associated with AGNs, of which 894 are blazars, 9 are radio galaxies, 5 are Seyfert galaxies, and 9 are other AGNs. Among the five Seyfert galaxies, four are narrow-line Seyfert 1 galaxies that have been established as a new class of γ-ray active AGNs (Abdo et al. 2009g). The fifth object is NGC 6814, which is associated with 2FGL J1942.5−1024. Note, however, that we expect up to ∼2 false positives among the Seyfert galaxy associations (cf. Table 9); hence, we cannot draw any firm conclusions about the possibility that normal Seyfert galaxies are indeed GeV γ-ray sources based on this single association.

AGNs observed by the LAT are also sources of radio (and X-ray) emission, and we find a clear trend that AGNs associated with 2FGL sources have larger radio fluxes than the average object in the counterpart catalogs. This trend, which was exploited already for the association of blazars in the EGRET catalog (Sowards-Emmerd et al. 2003), is illustrated in Figure 30, where we compare the distribution of the 8.4 GHz radio fluxes of all sources in the CRATES catalog to that for objects associated with 2FGL sources. Obviously, the average radio flux of CRATES sources associated with 2FGL sources is about one order of magnitude larger than the overall average for the CRATES catalog. Similar differences are observed for other radio catalogs.

In our dedicated effort to study the AGN population in the 2FGL catalog, which we publish in an accompanying paper (2LAC; Ackermann et al. 2011b), we make use of this property to enhance the sample of associated 2FGL sources. Briefly, instead of including all objects from the counterpart catalog in the estimation of the local counterpart densities ρ_k, we count only those objects with radio (or X-ray) flux equal or larger than the flux S of the counterpart under consideration, i.e., $\rho_k(>S)$. Using this procedure, the chance coincidence probabilities are considerably reduced, and consequently, the posterior association probabilities are increased (see also Sowards-Emmerd
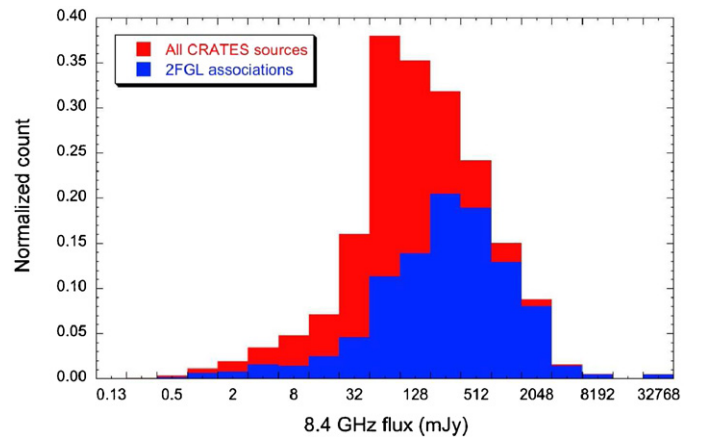

Figure 30. Normalized histograms of the 8.4 GHz radio flux of CRATES sources (red: all sources, blue: objects associated with 2FGL sources).

(A color version of this figure is available in the online journal.)

et al. 2003). We apply this procedure to a number of fairly uniform surveys of radio sources (CRATES, NVSS, SUMSS, PMN, ATCA 20 GHz, FRBA, GAPS, CLASS, and VCS) and to the ROSAT All-Sky Survey of X-ray sources, for which we assume the counterpart density $\rho_k(>S)$ to be position independent. In this case $\rho_k(>S)$ is then determined from the log N−log S distribution of objects in the catalog divided by the survey area, where N is the total number of sources with flux $>S$.

The 2LAC association procedure increases the number of AGN associations by 173, resulting in a total of 1090 2FGL sources that we associate with known AGNs; note that the 2LAC catalog lists two associated AGNs for the 27 2FGL sources for which more than one plausible association was found. The total number of 2FGL sources associated with a least one non-GeV γ-ray counterpart is thus 1314 (70% of all 2FGL sources). Among the AGN associations we find 1064 blazars, of which 432 are BL Lac objects (+38 with respect to the automatic association procedure), 370 are FSRQ (+24), and 262 are of unknown type (+108). The procedure also reveals two additional radio galaxies (For A associated with 2FGL J0322.4−3717 and PKS 0943−76 associated with 2FGL J0942.8−7558), and one additional Seyfert galaxy (ESO 323−77 associated with 2FGL J1306.9−4028). For the final AGN associations presented in the 2FGL catalog, we adopt the results of the 2LAC procedure combined with the results of the automatic association pipeline (see also Table 6).

Comparing to 1FGL (Abdo et al. 2010f), where out of 1451 sources 573 (40%) were found to be associated with blazars, 802 (43%) out of 1873 sources are associated with blazars in 2FGL, a relative increase which is readily explained by the particular effort that has been undertaken to maximize the number of blazar associations (Ackermann et al. 2011b). Neglecting the 2LAC blazar associations, the fraction of 2FGL sources associated with blazars would have been 40%, identical to what was found for 1FGL. On the other hand, the proportion of active galaxies of uncertain type (designated by "agu" in Table 4) has increased considerably: while 92 (6%) 1FGL sources were classified "agu," 262 (14%) 2FGL sources are now in this category, more than doubling the proportion of this source class. This increase can be explained by the extensive use of radio and X-ray surveys in the 2LAC association procedure that provides a greater number of blazar candidates that deserve dedicated follow-up observations to assess their natures. We also note

that in the 2FGL catalog we have two new extragalactic source classes with respect to 1FGL: radio galaxies ("rdg") and Seyfert galaxies ("sey"). Both were counted in the "non-blazar active galaxy" class (designated by "agn") in 1FGL, and 28 (1.9%) 1FGL sources were associated with that class. Adding the "rgd" and "sey" designators to the "agn" for 2FGL amounts to 27 (1.4%) associations, a number that is comparable to that found for 1FGL.

5.2.3. Normal Galaxies

Normal galaxies are now established as a class of high-energy γ-ray emitters (Abdo et al. 2010h), and we associate seven 2FGL sources with such objects. Of those, we consider the SMC (2FGL J0059.0−7242) and the LMC (2FGL J0526.6−6825) as identified owing to their spatial extensions in the LAT data. From the remaining five, four are classified as starburst galaxies: M82 (2FGL 0955.9+6936), NGC 253 (2FGL J0047.0−2516), NGC 4945 (2FGL J1305.8−4925), and NGC 1068 (2FGL J0242.5+0006). The fifth is the Andromeda galaxy M31 (2FGL J0042.5+4114).

Except for M31, all of the associated 2FGL γ-ray sources in this class were already present in 1FGL, yet the two starburst galaxies NGC 4945 and NGC 1068 were not associated as such as they were not included in our very limited counterpart catalog used at that time (Abdo et al. 2010f). For 2FGL, we included a catalog of infrared bright galaxies in the automatic association procedure (see Section 5.2) because starburst galaxies are prominent emitters in this waveband. Furthermore, we have found that the γ-ray fluxes of Local Group and starburst galaxies correlate well with star formation rates (Abdo et al. 2010h), which in turn correlate with infrared luminosity. Hence by selecting infrared bright galaxies from the IRAS Revised Bright Galaxy Sample (Sanders et al. 2003) we have added a catalog to our procedure that contains normal galaxies that are potential γ-ray emitters.

Three 2FGL sources lie within the extended-source template for the LMC (2FGL J0451.8−7011, 2FGL J0455.8−6920, and 2FGL J0533.3−6651; see Section 3.4). Their physical association with the LMC is not certain, but they are classified here as being part of the LMC and as mentioned in Section 5.2.1 are indicated in Table 4 as belonging to *LMC field*.

5.2.4. Pulsars

As of this writing, 87 pulsars have been firmly identified by the LAT through the detection of γ-ray pulsations. Four of these pulsars did not pass TS > 25 in the catalog analysis, and therefore they were excluded from the 2FGL catalog. These pulsars are PSR J1513−5908 (aka PSR B1509−58), PSR J1531−5610, PSR J1801−2451, and PSR J1939+2134. Of the remaining 83, 80 were formally associated by the automatic association procedure. The remaining three are found to be close to 2FGL sources, but their angular separation Δ from these sources exceeds their effective 99.9% location error radius $\theta_{99.9}$.[99] We find the following.

1. PSR J1023−5746 near 2FGL J1022.7−5741 ($\theta_{99.9} = 4'.2$, $\Delta = 5'.0$). 2FGL J1022.7−5741, which is in the Westerlund 2 field, lies only $10'$ from 2FGL J1023.5−5749c, so possibly the determination of its localization and/or localization uncertainty has been affected by this nearby source.

---

[99] The effective error radius is the size of the error ellipse at the position angle toward the counterpart. We estimate the 99.9% confidence radius by multiplying the 95% confidence radius by 1.52.

2. PSR J1357−6429 near 2FGL J1356.0−6436 ($\theta_{99.9} = 9'.1$, $\Delta = 9'.5$). 2FGL J1356.0−6436 is a relatively isolated source, but we note a possible association with the PWN HESS J1356−645 (Lemoine-Goumard et al. 2011).
3. PSR J1747−2958 near 2FGL J1747.1−3000 ($\theta_{99.9} = 2'.9$, $\Delta = 3'.2$). 2FGL J1747.1−3000 is located near the Galactic center, and the localization of the source may be affected by systematic uncertainties in the diffuse Galactic emission model.

In addition to the identified pulsars, four 2FGL sources are associated with radio pulsars:

1. 2FGL J1112.5−6105: PSR J1112−6103
2. 2FGL J1632.4−4820c: PSR J1632−4818
3. 2FGL J1717.5−5802: PSR J1717−5800 (?)
4. 2FGL J1928.8+1740c: PSR J1928+1746 (?).

PSR J1717−5800 has $\dot{E} = 2.3 \times 10^{32}$, 10 times lower than for any known γ-ray pulsar. The other three have $\dot{E} > 10^{34}$ erg s^{-1} and the LAT team phase folds γ-rays from their positions using radio rotation ephemerides as described by Smith et al. (2008). Gamma-ray pulsations have not been detected for these pulsars. We mark two of the associations as questionable (?) because the corresponding 2FGL sources have spectra that are considerably softer (spectral index ∼2.5) than typically observed for γ-ray pulsars (Abdo et al. 2010s).

The automatic association procedure also finds 21 2FGL sources to be associated with MSPs. Nineteen of those have unassociated counterparts in the 1FGL catalog and have been discovered in radio pulsar searches of unassociated 1FGL sources (e.g., Ransom et al. 2011; Cognard et al. 2011; Keith et al. 2011; Hessels et al. 2011). Rotation ephemerides accurate enough to allow phase folding γ-rays from the directions of the newly discovered radio pulsars can require a year of radio observations to disentangle, e.g., binary orbital motion from annual parallax. As the ephemerides become available many of the unassociated 1FGL sources may reveal γ-ray pulsations, as has already occurred for several. Two 2FGL sources associated with MSPs have no 1FGL counterparts:

1. 2FGL J1023.6 + 0040: PSR J1023+0038
2. 2FGL J1125.0−5821: PSR J1125−5825 (Bates et al. 2011).

Tam et al. (2010) reported the LAT detection of γ-ray emission toward PSR J1023+0038, the only known rotation powered MSP in a quiescent low-mass X-ray binary (LMXB). The spectrum of 2FGL J1023.6 + 0040 is rather soft (spectral index ∼2.5) for an MSP, but the system is sufficiently special that this does not necessarily rule out the association (see discussion in Tam et al. 2010).

5.2.5. Pulsar Wind Nebulae

Formally, we find 69 2FGL sources to be associated with PWNe, but except for three, all of them are also associated with known pulsars. Among those are three sources for which a dedicated analysis allowed us to identify both the pulsar and the PWN; they are summarized in Table 10, and the 2FGL catalog contains both the pulsar and the PWN as separate associated sources. For the other 63 2FGL sources, the observed pulsations firmly identify the pulsars as the primary source of the observed γ-rays, although some minor contribution from a PWN cannot be excluded.

More interesting are the three PWN associations for which no pulsar has so far been identified. These are the following:

Table 10
Identified PSR and PWN

Pulsar		Pulsar Wind Nebula		Ref.
PSR	2FGL	PWN	2FGL	
J0835−4510 (Vela)	J0835.3−4510	Vela X	J0833.1−4511e	1
J1509−5850	J1509.6−5850	MSH 15−52	J1514.0−5915e	2
J1826−1256	J1826.1−1256	HESS J1825−137	J1824.5−1351e	3

References. (1) Abdo et al. 2010k; (2) Abdo et al. 2010c; (3) Grondin et al. 2011.

1. 2FGL J1112.1−6040: G291.0−0.1
2. 2FGL J1640.5−4633: G338.3−0.0
3. 2FGL J1745.6−2858: G359.98−0.05 (?).

We mark the last association as questionable because this source is located in the immediate vicinity of the Galactic center where we know that the accuracy of our model of the diffuse Galactic emission is intrinsically limited, and because the large density of potential counterparts makes a reliable source association difficult.

In the 1FGL catalog we reported six sources associated with PWNe that were also not associated with known pulsars. Among those, two are among the three objects mentioned above (G338.3−0.0 and G359.98−0.05), one has turned out in fact to be a pulsar (2FGL J1135.3−6054), two are still unassociated 2FGL sources, but no longer associated with PWNe (2FGL J1552.8−5609 and 2FGL J1635.4−4717c), and one no longer has a corresponding source in 2FGL (G0.13−0.11, see Section 4.2).

5.2.6. Globular Clusters

Eleven 2FGL sources are associated with globular clusters. Among those, nine have been published previously: 47 Tuc (Abdo et al. 2009a), NGC 6266, NGC 6388, Terzan 5, NGC 6440, NGC 6626, NGC 6652 (Abdo et al. 2010f), Omega Cen (Abdo et al. 2010a), and M 80 (Tam et al. 2011b). In addition, we find two new associations:

1. *2FGL J1727.1−0704: IC 1257*. With an average significance of 4.1 this source is near the detection threshold. It is fitted using a PL with a spectral index of 2.2 ± 0.1, yet a 3.5σ curvature significance may indicate that the spectrum is in fact curved.
2. *2FGL J1808.6−1950c: 2MS-GC01*. This source has already been detected as 1FGL J1808.5−1954c, but the globular cluster catalog used for the association of 1FGL sources did not contain 2MS-GC01, and consequently the source remained unassociated. 2FGL J1808.6−1950c has an apparently curved spectrum (3.9σ significance) that is comparable to that of other globular clusters.

Tam et al. (2011b) have furthermore reported the detections of Liller 1, NGC 6139, NGC 6624, and NGC 6752 using LAT data. None of these clusters are formally associated with any of the 2FGL sources in the catalog. NGC 6624 is near 2FGL J1823.4−3014 ($\theta_{95} = 7'.7, \Delta = 7'.6$), but the formal posterior association probability of 50% is below our adopted threshold. A source associated with NGC 6752 was in our initial list of seeds for the catalog; however, it did not pass the detection threshold of TS > 25 for the 2FGL catalog. We could not find evidence for any sources in our data that might be associated with Liller 1 or NGC 6139.

5.2.7. Supernova Remnants

SNRs are a special class in our association scheme because a substantial number of the known objects are sufficiently extended to be potentially resolved with the LAT. We thus use two separate strategies to search for SNR associations among the 2FGL sources. For SNRs with angular diameters <20′, i.e., SNRs that still should appear point-like to the LAT, we use the Bayesian scheme to search for associations. In total, we find six 2FGL sources associated with point-like SNR, of which two are also associated with firmly identified pulsars. The remaining associations are the following:

1. 2FGL J1214.0−6237: G298.6−00.0
2. 2FGL J1911.0+0905: G043.3−00.2 (aka W49B)
3. 2FGL J2022.8+3843c: G076.9+01.0
4. 2FGL J2323.4+5849: G111.7−02.1 (aka Cas A).

None of them has a concurrent association with a PWN. Except for 2FGL J2022.8+3843c, all of them were already present and associated in 1FGL.

In a second pass we search for all 2FGL sources for which the 95% confidence error radius overlaps with the (assumed) circular extension of the SNR. This provides a list of 89 2FGL sources among which we estimate ~45% chance coincidences. Six of the 2FGL sources correspond to SNRs that were firmly identified as γ-ray sources based on their spatial extensions (IC 443, W28, W30, W44, W51C, and the Cygnus Loop), and four are the point-like SNRs listed above. Twenty of the 2FGL sources are firmly identified as being either a pulsar, a PWN, or an HMB system. This leaves 59 2FGL sources that might be associated with an extended SNR, among which we expect ~26 chance coincidences. Due to this high chance coincidence rate, we do not claim any SNR association for this list of sources, but we give the 2FGL names and associations in Table 11 for reference.

Several of the SNRs have extensions that encompass multiple 2FGL sources (G132.7+01.3, Monoceros Loop, Pup A, Vela Junior, and G089.0+04.7), in which case the 2FGL sources might actually correspond to local maxima of extended emission regions. A number of the SNRs have been detected at TeV energies, which makes their possible detection also in the LAT energy range more plausible. Three 2FGL sources have concurrent PWN associations, which makes them also good pulsar or PWN candidates. We also note that one source, 2FGL J2015.6+3709, is likely to be variable, hence a physical association with CTB 87 is highly improbable.

In 1FGL, 41 γ-ray sources were listed in the corresponding table of overlaps with SNRs (see Table 7 of Abdo et al. 2010f). About half of SNRs that were found overlapping with 1FGL sources are still in Table 11, while the other half have not been found to overlap spatially with any of the 2FGL sources. This illustrates the relatively large uncertainty that is tied to these associations and should present an additional warning to treat these potential associations with great care.

5.2.8. Binaries

The 2FGL catalog includes four HMB systems, all of which have been firmly identified by their orbital modulation, and are described in separate publications:

1. 2FGL J0240.5+6113: LSI +61 303 (Abdo et al. 2009c),
2. 2FGL J1019.0−5856: 1FGL J1018.6−5856 (Corbet et al. 2011),
3. 2FGL J1826.3−1450: LS 5039 (Abdo et al. 2009e), and
4. 2FGL J2032.1+4049: Cygnus X-3 (Abdo et al. 2009f).

Table 11
Potential Associations for Sources Near SNRs

2FGL Name	SNR Name	PWN Name	TeV Name	Common Name
J0128.0+6330	G127.1+00.5			
J0214.5+6251c	G132.7+01.3			
J0218.7+6208c	G132.7+01.3			
J0221.4+6257c	G132.7+01.3			
J0503.2+4643	G160.9+02.6			
J0526.6+4308	G166.0+04.3			
J0538.1+2718	G180.0−01.7			
J0553.9+3104	G179.0+02.6			
J0631.6+0640	G205.5+00.5			Monoceros Loop
J0636.0+0554	G205.5+00.5			Monoceros Loop
J0637.8+0737	G205.5+00.5			Monoceros Loop
J0821.0−4254	G260.4−03.4			Pup A
J0823.0−4246	G260.4−03.4			Pup A
J0823.4−4305	G260.4−03.4			Pup A
J0842.9−4721	G263.9−03.3			Vela
J0848.5−4535	G266.2−01.2		RX J0852.0−4622	Vela Junior
J0851.7−4635	G266.2−01.2		RX J0852.0−4622	Vela Junior
J0853.5−4711	G266.2−01.2		RX J0852.0−4622	Vela Junior
J0855.4−4625	G266.2−01.2		RX J0852.0−4622	Vela Junior
J1112.1−6040	G291.0−00.1	G291.0−0.1		
J1411.9−5744	G315.1+02.7			
J1441.6−5956	G316.3−00.0			
J1521.8−5735	G321.9−00.3			
J1552.8−5609	G326.3−01.8			Kes 25
J1615.0−5051	G332.4+00.1		HESS J1616−508	Kes 32
J1628.1−4857c	G335.2+00.1			
J1631.7−4720c	G336.7+00.5			
J1635.4−4717c	G337.2+00.1		HESS J1634−472	
J1640.5−4633	G338.3−00.0	G338.3−0.0	HESS J1640−465	
J1712.4−3941	G347.3−00.5		RX J1713.7−3946	
J1714.5−3829	G348.5+00.1		CTB 37A	CTB 37A
J1718.1−3725	G350.1−00.3			
J1727.3−4611	G343.0−06.0			RCW 114
J1731.6−3234c	G355.4+00.7			
J1737.2−3213	G356.3−00.3			
J1738.9−2908	G359.1+00.9			
J1740.4−3054c	G357.7−00.1			Tornado Nebula
J1745.5−3028c	G358.5−00.9		HESS J1745−303	
J1745.6−2858	G000.0+00.0	G359.98−0.05		Sgr A East
J1802.3−2445c	G005.4−01.2			Bird
J1811.1−1905c	G011.4−00.1			
J1828.3−1124c	G020.0−00.2			
J1834.3−0848	G023.3−00.3		HESS J1834−087	W 41
J1834.7−0705c	G024.7+00.6			
J1839.7−0334c	G028.8+01.5			
J1840.3−0413c	G027.8+00.6			
J1841.2−0459c	G027.4+00.0			Kes 73
J1849.3−0055	G031.9+00.0			Kes 77, 3C 391
J1850.7−0014c	G032.4+00.1			
J1852.7+0047c	G033.6+00.1			Kes 79
J1916.1+1106	G045.7−00.4			
J1932.1+1913	G054.4−00.3			
J2015.6+3709[a]	G074.9+01.2			CTB 87
J2019.1+4040	G078.2+02.1		VER J2019+407	Gamma Cygni
J2041.5+5003	G089.0+04.7			
J2043.3+5105	G089.0+04.7			
J2046.0+4954	G089.0+04.7			
J2333.3+6237	G114.3+00.3			
J2358.9+6325	G116.5+01.1			

Note. [a] Source is likely to be variable.

No further 2FGL source is associated with a high-mass X-ray binary from Liu's catalog (Liu et al. 2006). All four sources were already present in the 1FGL catalog, yet the orbital modulation of 1FGL J1018.6−5856 was only recently discovered in a blind search using the LAT data (Corbet et al. 2011).

Formally, the automatic association procedure associates three 2FGL sources with LMXBs, but all three are located in globular clusters, and the observed emission can be readily explained by the combined emission of MSPs (Abdo et al. 2009a). We thus conclude that no LMXB systems have been identified in the LAT data after two years of observations. We came to the same conclusion for 11 months of data in our study of the 1FGL associations (Abdo et al. 2010f).

5.2.9. Massive Stars and Open Star Clusters

Among the massive star catalogs (O stars, W–R stars, and LBVs) and the open cluster catalog we find only two possible associations with 2FGL sources:

1. *2FGL J1045.0−5941: η Carinae (LBV)*. The γ-ray emission of this well-known peculiar binary system has been studied in detail by Tavani et al. (2009), Abdo et al. (2010g), and Farnier et al. (2011), yet a firm identification of the system through periodic orbital variability in γ-rays is still missing.
2. *2FGL J2030.7+4417: HD 195592 (O star)*. This O9.5Ia type star is probably a short period (5.063 days) O+B binary system at a distance of 1.1 kpc that may have escaped from the open cluster NGC 6913 (De Becker et al. 2010). We note, however, that the object is located in the Cygnus region where the high O star density easily could lead to false associations and the complex diffuse emission may render precise source localization difficult. In addition, the spectral shape and the apparent lack of variability of 2FGL J2030.7+4417 are similar to the characteristics of identified γ-ray pulsars. Hence, we caution against overinterpreting this particular O star association and we do not list it in our final table.

5.2.10. Multiwavelength Associations

In addition to the catalogs of classified sources, we also search for associations with catalogs of radio and TeV sources. Our association procedure for AGNs heavily relies on associations with radio sources as most of the γ-ray-emitting AGNs are bright sources of radio emission (see Section 5.2.2). In fact, essentially all of the radio associations we find have been classified subsequently as AGNs.

Eighteen 2FGL sources that have not been associated with any object in one of our catalogs of known or plausible γ-ray-emitting source classes (our type 1 catalogs in Section 5.2) have associations with extended TeV sources. However, due to the relatively large extents of the sources in the extended TeV catalog, we expect on average 20 false associations (cf. Table 9), so from a statistical point of view, all 18 associations could be spurious. We discuss 2FGL associations with TeV sources more deeply in Section 5.3.

5.2.11. Other GeV Detections

The automated association process compares the 2FGL source locations with other catalogs of sources seen at GeV energies. Results are shown in the main table for individual sources. From the Bright Gamma-Ray Source List (Abdo et al. 2009d) we find 185 out of 205 sources associated with 2FGL

sources. Comparison with the 1FGL catalog was described in detail in Section 4.2. In total, we find 1099 out of 1451 1FGL sources that are associated with 2FGL sources.

The only contemporaneous catalog from a different instrument is the AGILE (1AGL) catalog (Pittori et al. 2009), which has 42 (out of 47) sources in common with the 2FGL catalog. The five 1AGL sources that are not formally associated (1AGL J0657+4554, 1AGL J0714+3340, 1AGL J1022−5822, 1AGL J1803−2258, and 1AGL J1823−1454) all lie close to 2FGL sources and spatially overlap within their mutual 99% confidence localization uncertainties. Several 2FGL sources are associated with the same 1AGL source, and in total we find 57 2FGL sources associated with sources listed in 1AGL.

From the previous generation high-energy γ-ray telescope, EGRET on the *Compton Gamma Ray Observatory*, the 3EG catalog (Hartman et al. 1999) had 111 sources (out of 271) associated by the automatic process with 2FGL sources, while the EGR catalog (Casandjian & Grenier 2008) had 66 (out of 188) sources associated with 2FGL sources. Also here we find several 2FGL sources that are associated with the same EGRET source. In total, 116 2FGL sources are associated with sources in 3EG, while 69 2FGL sources are associated with sources in EGR. The fractions of 3EG and EGR sources with 1FGL sources were similarly low and the discussion in the 1FGL catalog paper is still relevant (Abdo et al. 2010f); we also refer the reader to a study of unassociated 1FGL sources (Ackermann et al. 2012a). An EGRET catalog based on analysis of energies above 1 GeV (Lamb & Macomb 1997) found 46 high-confidence sources, of which 40 have clear 2FGL counterparts, 5 have close 2FGL sources just outside the 95% confidence contours, and only 1 (GEV 2026+4124 in the confused Cygnus region) lacks a plausible 2FGL match.

Through 2011 June, 94 flaring *Fermi*-LAT sources were detected and promptly reported in more than 150 Astronomer's Telegrams. Of these, eight are not in 2FGL. For six of these the flaring state was detected outside the time interval covered by 2FGL: SBS 0846+513 (a new NLSy1 system: Donato & Perkins 2011), SHBL J001355.9−185406 (see Section 5.3; Sanchez & Fegan 2010), PSR B1259−63 (see Section 5.3; Abdo et al. 2010t), PMN J1123−6417 (see Section 4.2; D'Ammando 2011), PMN J1913−3630 (Donato & Cheung 2010), and the flaring source in the Galactic center region (Vasileiou et al. 2011). The other two sources are J1057−6027 (Yasuda et al. 2009), detected in 2009 June, is not included in 1FGL and does not have a 2FGL counterpart but could be associated with 2FGL J1056.2−6021 using the 99.9% confidence error radius; and PKS 1915−458 (Sokolovsky et al. 2010) a faint and high-redshift blazar (z = 2.47), detected in 2010 June, whose average flux between 2008 August and 2010 August is below the 2FGL catalog significance threshold. Also, we note that two 1FGL unidentified flaring sources detected along the Galactic plane, 3EG J0903−3531 (Hays et al. 2008) and J0910−5041 (2FGL J0910.4−5050 or 1FGL J0910.4−5055; Cheung et al. 2008) are now associated with two unclassified AGNs in 2FGL, PMN J0904−3514 and AT20G J0910−5048, respectively. Furthermore, the 2FGL counterpart for J1512−3221 (Wallace 2010), which had no clear association, is 2FGL J1513.6−3233 which is associated with blazar CRATES J1513−3234.

5.3. TeV Source Associations

2FGL sources that are positionally associated with sources seen by the ground-based TeV telescopes are of particular interest because the TeV band overlaps with the LAT energy range,

suggesting the potential for common emission mechanisms if the spectra match. As described in Table 9, we investigated associations with the sources in the TeVCat compilation of detections. The compilation is growing with time, and information about the sources is subject to updates and refinements, but at any given time TeVCat represents a snapshot of current knowledge of the TeV sky.

The association analysis was done separately for extended and point-like TeV sources, taking into account the statistical and systematic uncertainties in the source localization. The "TeV" column of Table 4 lists associations with extended sources as "E" and point-like sources as "P." As the table indicates, 85 2FGL sources are positionally consistent with TeVCat sources, although multiple 2FGL associations are seen for some TeV sources. In the FITS version of the catalog, we also provide the names of the associated TeV sources.

Of the TeV sources considered for the associations performed here, most correspond to known objects at other wavelengths, in particular those that lie far from the Galactic plane. A large fraction (∼50%) of the TeV Galactic sources, however, are still unidentified. Many of these have plausible counterparts while others remain unassociated despite deep searches for counterparts at other wavelengths. Among the firm identifications in the TeV regime, there are seven different source classes, and members of each of these source classes have been associated with 2FGL sources. In total, 85 TeV sources have 2FGL counterparts. Eight of these TeV sources have more than one 2FGL association. RX J0852.0−4622 has four 2FGL associations, and the following TeV sources have two each: Westerlund 1 (Ohm et al. 2010), Westerlund 2, HESS J1632−478, RX J1713.7−3946, W28 (Abdo et al. 2010j), HESS J1841−055, and MGRO J2019+37. One LAT source, 2FGL J2229.0+6114, is associated with two TeV sources, Boomerang and G106.3+2.7. The LAT emission from two of the TeV sources, IC 443 and MSH 15−52, is measured to be extended.

The TeV class that has the most numerous associations with the 2FGL sources is the AGN class (see Ackermann et al. 2011b for a more detailed discussion of the LAT AGN). There are currently 45 AGNs detected at TeV energies and all but 6 of these are associated with 2FGL sources. The six that do not have 2FGL counterparts (SHBL J001355.9−185406, 1ES 0229+200, 1ES 0347−121, PKS 0548−322, 1ES 1312−423, and HESS J1943+213[100]) are all high-frequency peaked BL Lac objects. This is the subclass of AGNs that tend to have the lowest bolometric luminosities and their second emission peaks at the highest energies. The six TeV AGNs that did not reach the detection threshold to be included in the 2FGL catalog are among the weakest extragalactic TeV sources detected to date, ranging in flux from 0.4% to 2% of the flux of Crab Nebula at those energies.

Both of the starburst galaxies detected at TeV energies, M 82 and NGC 253, have 2FGL counterparts (Abdo et al. 2010b).

Four HMBs have confirmed detections in the TeV regime. Two of these, LS I +61 303 and LS 5039, have 2FGL counterparts and are already the subject of LAT publications (Abdo et al. 2009c, 2009e). We note that, although not in 2FGL, the TeV binary PSR B1259−63 has been detected by the LAT (Tam et al. 2011a; Abdo et al. 2011a). This system is a radio pulsar in orbit around a Be star with an orbital period of

∼3.4 years. During the time span of the 2FGL data, the system was far from periastron and no significant GeV emission was detected, but when the system approached periastron, variable emission, including flaring behavior, was observed by the LAT.

The PWNe comprise the second most numerous identified TeV class that is associated with 2FGL sources; of the 25 PWNe in TeVCat, 16 are associated with 2FGL sources. Indeed, the association between GeV γ-ray PSRs and the PWNe visible in the regime has been well established already (A. A. Abdo et al. 2012c, in preparation; Abdo et al. 2010s).

During the second year of LAT data taking, many more SNRs known at TeV energies were detected at GeV energies such as Cas A (Abdo et al. 2010l), RX J1713.7−3946 (Abdo et al. 2011d), and Vela Jr (Tanaka et al. 2011). Of the five SNR/Molecular Cloud associations in TeVCat, all but one (G318.2+0.1) have been associated with 2FGL sources. Ten shell-type SNRs have been detected at TeV energies and five of these now have 2FGL counterparts, so the GeV–TeV association is established although there are still many open questions. *Fermi*'s non-detection of RCW 86 is surprising since it is one of the brightest TeV SNRs, with a flux of ∼10% that of the Crab Nebula (Aharonian et al. 2009).

Sources of particular interest are those that are positionally consistent between the LAT and TeV telescopes but have no obvious associations with objects at longer wavelengths. Among the TeV sources that have no clear identifications, 17 are associated with 2FGL sources. In addition to these, although not formally associated with LAT sources using the automatic pipeline (Section 5.2), some other TeV sources have possible 2FGL counterparts, for example, HESS J1843−033, which has two potential 2FGL counterparts. Establishing a physical connection through spectral or variability studies may help determine the nature of these sources. In many cases, a GeV counterpart could prove crucial for our understanding of the nature of the TeV source, in particular for the following objects:

1. 2FGL J1022.7−5741 and 2FGL J1023.5−5749 are spatially consistent with HESS J1023−575, itself not yet firmly identified, but noted for its possible connection to the young stellar cluster Westerlund 2 in the star-forming region RCW 49, as discussed by HESS Collaboration (2011c).
2. 2FGL J1427.6−6048 is associated with HESS J1427−608 which is, so far, without plausible counterparts (Aharonian et al. 2008b).
3. 2FGL J1503.9−5800 is spatially coincident with the TeV source HESS J1503−582, which is tentatively associated with a forbidden velocity region of interstellar gas (Renaud et al. 2008).
4. 2FGL J1507.0−6223 is spatially consistent with HESS J1507−622 (HESS Collaboration 2011a), so far the only TeV unidentified source that is markedly offset from the Galactic plane (∼3°.5).
5. 2FGL J1615.2−5138 is spatially consistent with one of the brightest (∼25% of the Crab Nebula flux) TeV unidentified sources, HESS J1614−518 (Aharonian et al. 2006).
6. 2FGL J1650.6−4603 is spatially associated with a TeV source tentatively associated with the Westerlund 1 star-forming region. (The other 2FGL source that is spatially associated with this TeV source is 2FGL J1648.4−4612, which is pulsar PSR J1648−4611.)
7. 2FGL J1848.2−0139. This source is consistent with the TeV source, HESS J1848−018, which is suspected to be correlated with the star-forming region W 43 (Chaves et al. 2008).

---

[100] This source has not been confirmed to be an HBL but all available observations favor its classification as an HBL (HESS Collaboration 2011b).
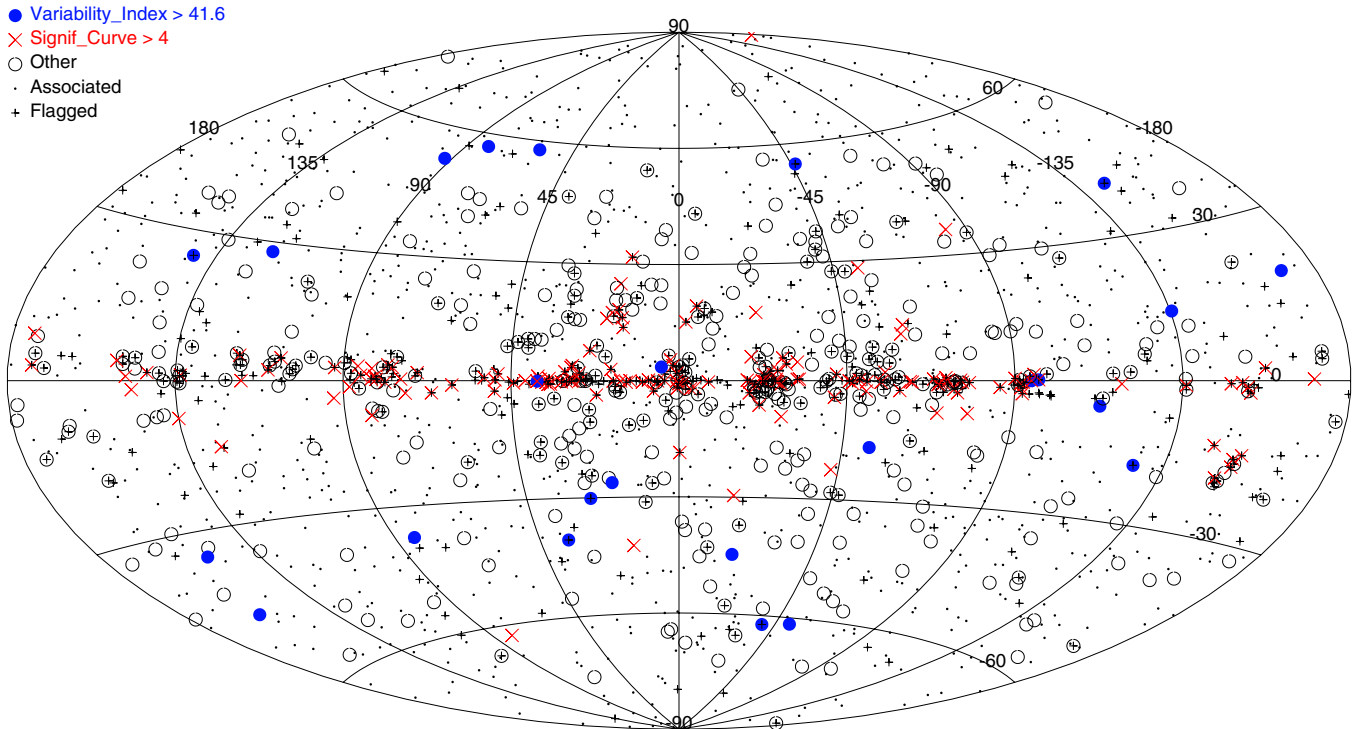
Figure 31. Sky distribution of associated (dots) and unassociated sources (large symbols). Sources that were flagged are marked by a plus. In particular, we mark variable unassociated sources (TS$_{var}$ > 41.6) using filled blue circles, unassociated sources with a curved spectrum (Signif_Curve > 4) by red crosses, and all other unassociated sources by open black circles.

(A color version of this figure is available in the online journal.)

As discussed in Section 2.2, the Galactic center region is particularly complex and its study is beyond the purpose of this paper; we do, however, find possible associations with all of the TeV γ-ray sources detected in this region, although not all were formally associated by the automatic pipeline analysis: the Galactic center source (Acero et al. 2010), HESS J1745−303 (2FGL J1745.5−3028c; Aharonian et al. 2008a), HESS J1741−302 (Tibolla et al. 2008), and HESS J1747−248 (2FGL J1748.0−2447; HESS Collaboration 2011d).

5.4. Properties of Unassociated Sources

Among the 1873 sources in the 2FGL catalog, 575 (31%) remain unassociated. Their distribution on the sky is compared in Figure 31 to the distribution of the associated sources. We note a number of interesting features in the map that should be kept in mind when considering unassociated 2FGL sources.

First, the number of unassociated sources decreases with increasing Galactic latitude. This is best illustrated by a latitude histogram of the fraction of unassociated 2FGL sources, shown in Figure 32. We plot here the data as a function of the sine of Galactic latitude as in this representation an isotropic distribution will appear as a flat profile. In contrast to that, we find that the fraction of unassociated sources decreases with latitude, with the decrease being steeper at positive latitudes. This asymmetry is also present in the absolute numbers: above Galactic latitudes $b > 60°$ only 3 sources in 2FGL are unassociated, while below $b < −60°$ we find 12 unassociated sources. This may be due to relative completeness in the north versus the source of the counterpart catalogs used for the source association analysis (Section 5.2).

Second, the numbers of unassociated sources increase sharply below $|b| \approx 10°$. This is attributable to the relative lack of sources below $|b| < 10°$ in many of the extragalactic source catalogs that we use for source association. The Milky Way is a bright source of radio emission, limiting sensitive searches for extragalactic sources near the Galactic plane. Furthermore, optical identifications of radio sources are hampered by the important interstellar obscuration, leaving many radio sources unclassified.

Third, the numbers of 2FGL sources with curved spectra increase at low Galactic latitudes, as can be seen in the latitude histogram (dashed line in Figure 32) and the sky map (red crosses in Figure 31). The sky map indicates that these sources tend to cluster in regions of bright Galactic diffuse emission, such as the inner Galactic ridge (Galactic longitudes $330° < l < 30°$), the Cygnus region ($l \approx 80°$), the Norma spiral arm tangent ($l \approx 330°$), or the Crux spiral arm tangent ($l \approx 300°$). Whether this clustering is diagnostic of the physical natures of the sources, or whether it indicates systematic uncertainties in the Galactic diffuse emission model that resulted in spurious source detections remains a possibility. We note, however, that the fraction of sources with curved spectra among the unassociated sources is greater (28%) than the fraction of curved spectra sources among the associated sources (16%). Because the spectrum of the Galactic diffuse emission at low latitudes is itself well represented with a curved spectrum, at least some fraction of the unassociated 2FGL sources at low latitudes may be local emission maxima of diffuse Galactic emission that are not adequately modeled by our Galactic diffuse model; see the discussion in Section 3.9 and the definitions of the several analysis flags that are related to the model of the Galactic diffuse emission in Section 3.10.
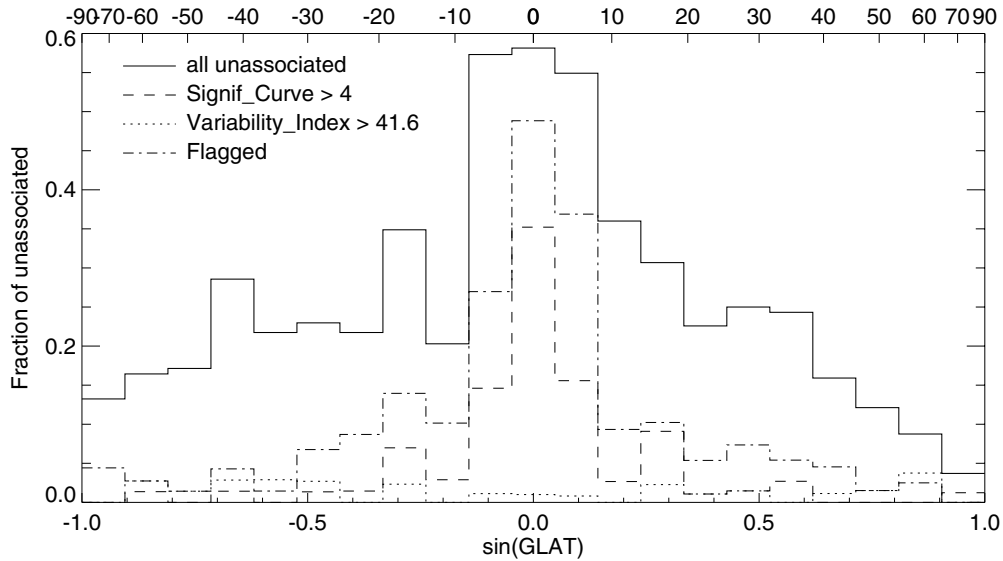
Figure 32. Latitude distribution of unassociated sources.

Fourth, a substantial fraction of the unassociated sources have at least one analysis flag (Section 3.10) set. We find that 51% of the unassociated sources have been flagged due to various issues, while only 14% of the associated sources have been flagged. None of the flags is related to our association procedure itself, but they identify a number of conditions that can shed doubt on the physical reality or localization quality of a source. The fact that such a large fraction of unassociated sources are flagged may indicate that some of these sources are indeed not real. We emphasize that the analysis flags should be taken into consideration when using the 2FGL catalog.

Fifth, 25 unassociated sources (4%) have been flagged as variable, and the spatial distribution of these sources appears rather isotropic. These sources are good candidates for being as-yet unassociated AGNs, as this is the source class that shows the largest flux variability in LAT data.

6. CONCLUSIONS

The second *Fermi*-LAT catalog is the product of a comprehensive analysis of the first two years of LAT science data. In several ways it is an advance over the 1FGL catalog, which was based on the first 11 months of data. The 2FGL analysis takes advantage of the new P7_V6 Source event selection and IRFs, which in particular provide increased effective area in the range below ∼200 MeV. The analysis also uses a refined model for the Galactic diffuse emission. The source detection and localization analyses were advanced for the 2FGL analysis to iteratively optimize the definitions of the "seed" sources used for the final likelihood analysis step. Both analysis steps allowed for non-PL source spectra and also incorporated special models for spatially extended sources. The source association analysis was also extensively updated for the 2FGL catalog, with updated catalogs of counterparts and local determinations of counterpart densities. For AGNs, the association analyses also included methods that took into account radio and X-ray properties of potential counterparts.

The 2FGL catalog contains 1873 sources. In developing the catalog analysis, we re-evaluated a number of the analysis flags used to tag sources with unusual or potentially problematic properties. The most prominent flag is the "c" designator, which we have appended to the names of 162 sources, and indicates

potential confusion with interstellar diffuse emission or an artifact in the model for the diffuse emission. A number of other flags are defined, and 315 sources have one or more of these other flags set.

The 2FGL catalog represents a new milestone in high-energy *γ*-ray astrophysics. As with any astronomical catalog, 2FGL enables a wide range of astrophysical research. For individual objects, the spectra and light curves offer opportunities for multiwavelength modeling that can lead to better physical understanding of sources. The catalog as a collection allows population studies for *γ*-ray-only sources and for comparative studies with other wavelengths. In the catalog, 127 sources are considered to be identified, and plausible associations are proposed for more than 1000 AGNs. In all identifications or associations of 2FGL sources with 15 classes of counterparts are proposed. In addition, the fact that 575 of the 2FGL sources have no plausible counterparts among known *γ*-ray-producing source classes presents discovery opportunities similar to those already found with the *Fermi*-LAT Bright Source List and 1FGL catalog. Even the absence of 2FGL sources in predicted source classes such as clusters of galaxies will stimulate additional research into why these known sources of nonthermal radiation are not producing *γ*-rays at a level yet detectable with the LAT. We look forward to extensive use of this catalog in high-energy astrophysics.
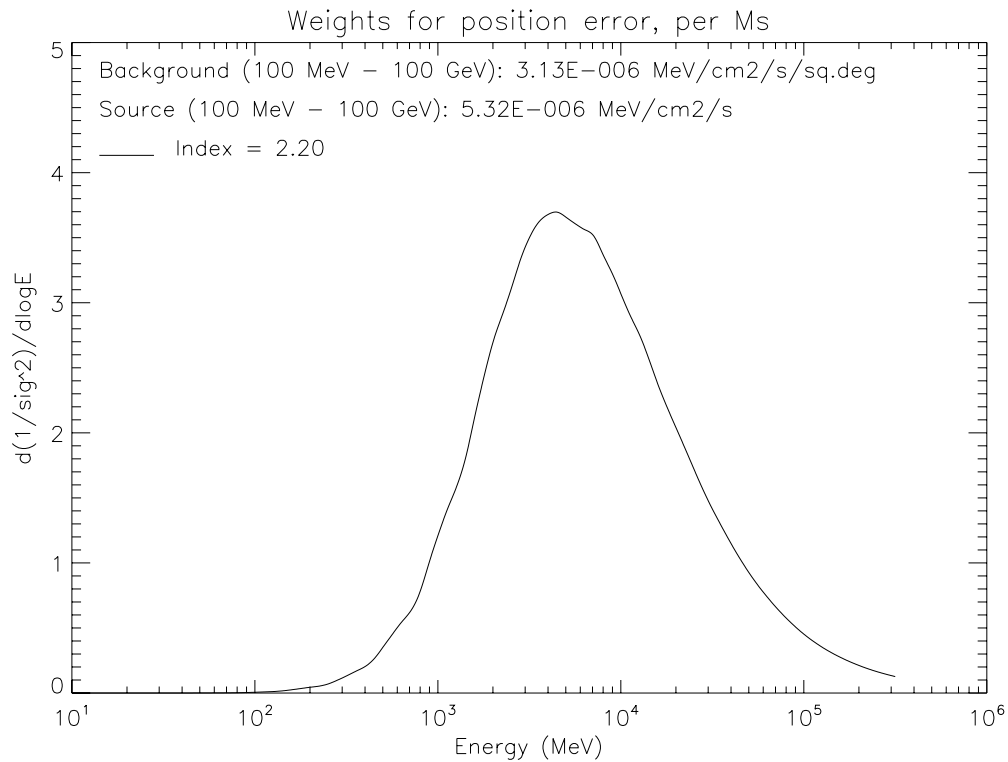
Figure 33. Theoretical contribution ($W_l(E)$ of Equation (A3)) to $\Delta\theta_0^{-2}$ per Ms and per $\log(E)$ interval as a function of energy for a TS = 100 power-law source over the average background at $|b| > 10°$. The assumed photon spectral index is 2.2.
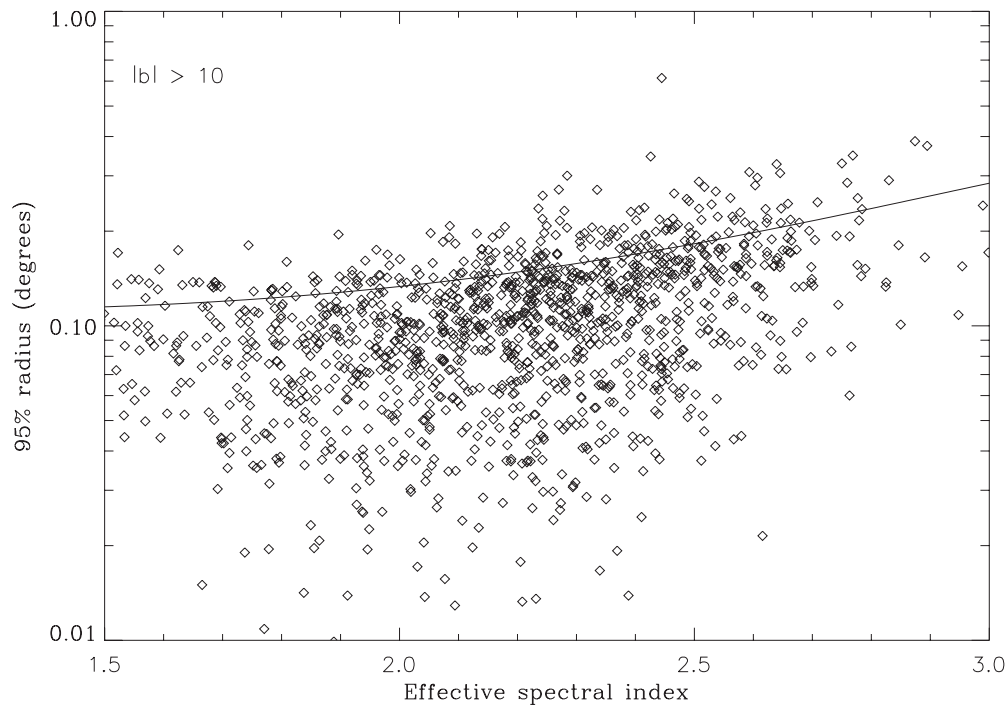

Figure 34. 95% error radius of sources at $|b| > 10°$ as a function of spectral index. The line shows the theoretical error radius for an isolated source at the detection threshold of TS = 25 over the average extragalactic background.

This work made extensive use of the ATNF pulsar catalog[101] (Manchester et al. 2005). This research has made use of the

---

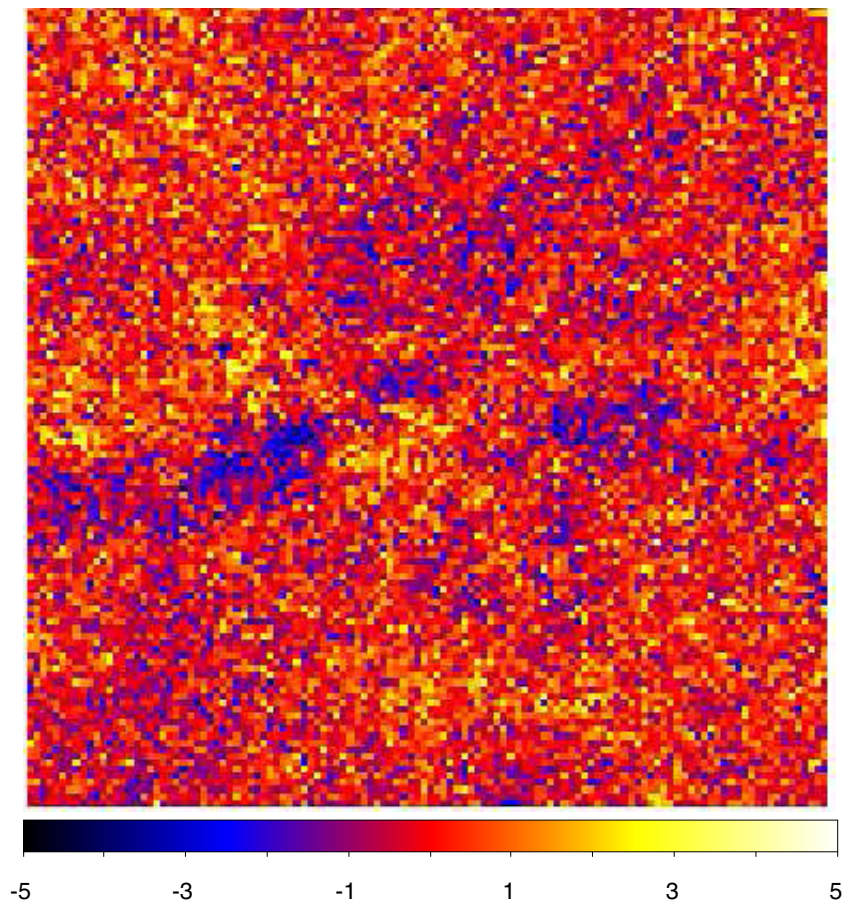[101] http://www.atnf.csiro.au/research/pulsar/psrcat

Figure 35. Residuals (in σ units) in $0°.5$ pixels over a $60° \times 60°$ area around the Galactic anticenter, summed over the full energy range (100 MeV to 100 GeV). All sources were fixed to the catalog values and the diffuse parameters were fitted as in an ordinary RoI (Section 3.2). The pixels used in the source fitting process were much smaller. The larger pixels used here allow reducing the statistical fluctuations to 5% in the Galactic plane and 10% at the top and bottom of the plot.

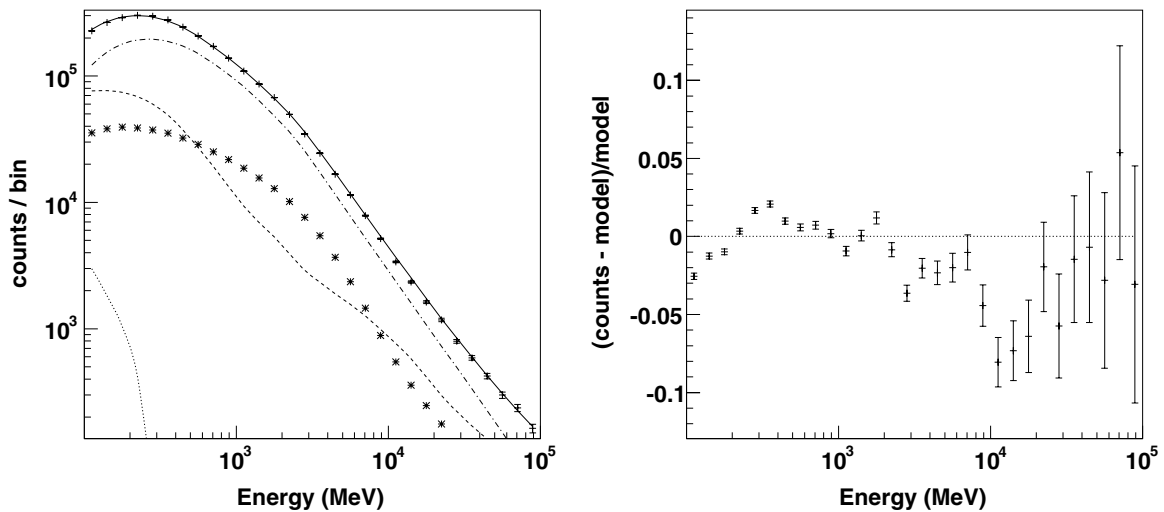(A color version of this figure is available in the online journal.)

Figure 36. Left: fit to the full spectrum integrated over the same anticenter region as in Figure 35. The spectral bins are the same as in the source fitting process. The dotted, dashed, and dash-dotted lines are the Earth limb, isotropic, and Galactic components, respectively. The asterisks show the total source contribution (dominated by the Geminga and Crab pulsars). The full line is the sum of all model contributions, to be compared with the data (plus signs). The statistical errors on the data are shown but barely visible except at high energy. Right: fractional residuals (data/model−1) with statistical error bars. The residuals are statistically significant because of the very large number of events (2.8×10^6 over that area) but are only a few percent.

NASA/IPAC Extragalactic Database (NED) which is operated by the Jet Propulsion Laboratory, California Institute of Technology, under contract with the National Aeronautics and Space Administration.

This research has made use of Aladin,[102] TOPCAT,[103] and APLpy, an open-source plotting package for Python.[104] The authors acknowledge the use of HEALPix[105] (Górski et al. 2005).

Facility: Fermi

APPENDIX A

LOCALIZATION POWER

In the maximum likelihood formalism, the error ellipse (Section 3.1.4) is given by the covariance matrix of the position parameters after the fit. One can obtain an approximate but reasonably accurate estimate of the localization power of the *Fermi*-LAT for a point source, assuming that the diffuse background is locally uniform and considering only one source. In that approximation the error ellipse is a circle and the 1σ localization precision of a source along any direction $\Delta\theta_0$ is given by

$$\Delta\theta_0^{-2} = \left| \frac{\partial^2 \log \mathcal{L}}{\partial \theta_0^2} \right| = \frac{1}{2} \left| \frac{\partial^2 \mathrm{TS}}{\partial \theta_0^2} \right| \qquad (A1)$$

and is related to the 95% error radius by $r_{95}/\Delta\theta_0 = \sqrt{-2 \log(0.05)} = 2.45$. Along the lines of Equation (A1) of Abdo et al. (2010f), denoting $S(E)$ the source spectrum, $B(E)$ the background spectrum per unit solid angle, T_0 the equivalent on-axis observing time, $A_{\mathrm{eff}}(E)$ the on-axis effective area and the local source to background ratio $g(\theta, E) = S(E)\mathrm{PSF}(\theta, E)/B(E)$, one may write

$$\Delta\theta_0^{-2} = T_0 \int_{\log E_{\min}}^{\log E_{\max}} W_l(E) \, d\log E \qquad (A2)$$

$$W_l(E) = \pi E A_{\mathrm{eff}}(E) \frac{S(E)^2}{B(E)} \int_0^\pi \left(\frac{\partial \mathrm{PSF}}{\partial \theta} \right)^2 \frac{\sin\theta \, d\theta}{1 + g(\theta, E)} \qquad (A3)$$

after integrating the $\cos^2 \phi$ term arising from the projection along one direction. Here $W_l(E)$ is the contribution to $\Delta\theta_0^{-2}$ per unit log(energy). It is illustrated in Figure 33 for a PL source spectrum at high latitude. Not surprisingly, the localization depends even more on high energy (where the core PSF is narrowest) than the detection itself (Figure 18 of Abdo et al. 2010f). For that reason, the average effect of confusion on localization is small, because it is important only at those energies when the average angular distance between sources (2°.8 at high latitude) is comparable to the PSF width.

For each spectral index it is possible to compute the detection threshold and then the localization precision at the detection threshold. This is normally the worst error radius one may expect in the catalog. That prediction is compared in Figure 34 with the actual 95% error radius. The curve accurately predicts the dependence on spectral index. The localization is worse for softer sources, but only by a relatively small factor at a given

TS. A few sources are above the line. This can happen for purely statistical reasons, because the background and exposure depend a little on direction even after taking out the Galactic plane, or because of another nearby source. The highest point (worst error ellipse) is 2FGL J1952.6−3252, which is specifically flagged for imperfect localization (Flags 8 and 9 set).

APPENDIX B

QUALITY OF THE FIT

In order to illustrate the global quality of the main spectral fit (Section 3.2), we show in Figures 35 and 36 the spatial and spectral residuals over a large sky region rather than an individual RoI which could hide cross-talk issues. We chose the Galactic anticenter which is halfway between the quiet high-latitude regions and the most difficult Galactic Ridge regions discussed in Section 3.9.

We fit the same parameters as in an ordinary RoI: normalizations of the isotropic and Galactic components K_{iso} and K_{gal}, and corrective slope of the Galactic component Γ_{gal}, such that the correction to the Galactic model is $K_{\mathrm{gal}}(E/E_0)^{-\Gamma_{\mathrm{gal}}}$ with E_0 set to 500 MeV. The fitted parameters were $K_{\mathrm{iso}} = 0.973$, $K_{\mathrm{gal}} = 1.003$, and $\Gamma_{\mathrm{gal}} = 0.029$.

The spatial residuals are scaled to the Poisson noise in each pixel in order to quantify whether the deviations are significant. What is shown is (data−model)/$\sqrt{\mathrm{model}}$. The pixel size is large enough that there are about 100 counts pixel^{-1} outside the plane. The distribution of spatial residuals on 0°.5 pixels follows very closely a normal law. Its standard deviation is only 1.1σ, implying that the intrinsic fluctuations are about 0.5σ, or 5%. They appear to be on a scale of a few degrees. The spectral residuals are a few percent and evolve slowly with energy. Those are small imperfections of the diffuse model, which show up because of the very high statistical quality of the data. Their impact on sources is limited because the residuals are on a larger scale than the LAT PSF except at low energy. It is quantified in Section 3.7.

APPENDIX C

DESCRIPTION OF THE FITS VERSION OF THE 2FGL CATALOG

The FITS format version of the 2FGL catalog[106] has four binary table extensions. The extension `LAT_Point_Source_Catalog Extension` has all of the information about the sources, including the monthly light curves (Table 12).

The extension `Hist_Start` lists the Mission Elapsed Time (seconds since 00:00 UTC on 2000 January 1) of the start of each bin of the monthly light curves. The final entry is the ending time of the last bin.

The extension `GTI` is a standard Good-Time Interval listing the precise time intervals (start and stop in MET) included in the data analysis. The number of intervals is fairly large because on most orbits (∼95 minutes) *Fermi* passes through the SAA, and science data taking is stopped during these times. In addition, data taking is briefly interrupted on each non-SAA-crossing orbit, as *Fermi* crosses the ascending node. Filtering of time intervals with large rocking angles, other data gaps, or operation in non-standard configurations introduces some more entries. The GTI is provided for reference and would be useful, e.g., for

---

Table 12
LAT 2FGL FITS Format: LAT_Point_Source_Catalog Extension

Column	Format	Unit	Description
Source_Name	18A	. . .	. . .
RAJ2000	E	deg	Right ascension.
DEJ2000	E	deg	Declination.
GLON	E	deg	Galactic longitude.
GLAT	E	deg	Galactic latitude.
Conf_68_SemiMajor	E	deg	Long radius of error ellipse at 68% confidence.
Conf_68_SemiMinor	E	deg	Short radius of error ellipse at 68% confidence.
Conf_68_PosAng	E	deg	Position angle of the 68% long axis from celestial north, positive toward increasing R.A. (eastward).
	. . .		
Conf_95_SemiMajor	E	deg	Long radius of error ellipse at 95% confidence.
Conf_95_SemiMinor	E	deg	Short radius of error ellipse at 95% confidence.
Conf_95_PosAng	E	deg	Position angle of the 95% long axis from celestial north, positive toward increasing R.A. (eastward).
Signif_Avg	E	. . .	Source significance in σ units (derived from test statistic).
Pivot_Energy	E	MeV	Energy at which error on differential flux is minimal.
Flux_Density	E	cm^{-2} MeV^{-1} s^{-1}	Differential flux at Pivot_Energy.
Unc_Flux_Density	E	cm^{-2} MeV^{-1} s^{-1}	1σ error on differential flux at Pivot_Energy.
Spectral_Index	E	. . .	Best-fit photon number power-law index. For LogParabola spectra, index at Pivot_Energy; for PLExpCutoff spectra, low-energy index.
	. . .		
Unc_Spectral_Index	E	. . .	1σ error on Spectral_Index.
Flux1000	E	cm^{-2} s^{-1}	Integral flux from 1 to 100 GeV.
Unc_Flux1000	E	cm^{-2} s^{-1}	1σ error on integral flux from 1 to 100 GeV.
Energy_Flux100	E	erg cm^{-2} s^{-1}	Energy flux from 100 MeV to 100 GeV obtained by spectral fitting.
Unc_Energy_Flux100	E	erg cm^{-2} s^{-1}	1σ error on energy flux from 100 MeV to 100 GeV.
Signif_Curve	E	. . .	Significance (in σ units) of the fit improvement between power-law and either LogParabola (for ordinary sources) or PLExpCutoff (for pulsars). A value greater than 4 indicates significant curvature.
SpectrumType	18A	. . .	Spectral type (PowerLaw, LogParabola, PLExpCutoff).
beta	E	. . .	Curvature parameter (β) for LogParabola. NULL for other spectral types.
Unc_beta	E	. . .	1σ error on β for LogParabola. NULL for other spectral types
Cutoff	E	MeV	Cutoff energy as exp(-E/Cutoff) for PLExpCutoff. NULL for other spectral types.
Unc_Cutoff	E	MeV	1σ error on cutoff energy for PLExpCutoff. NULL for other spectral types.
PowerLaw_Index	E	. . .	Best-fit power-law index. Equal to Spectral_Index if SpecrumType is PowerLaw.
Flux30_100	E	cm^{-2} s^{-1}	Integral flux from 30 to 100 MeV (not filled).
Unc_Flux30_100	E	cm^{-2} s^{-1}	1σ error on integral flux from 30 to 100 MeV (not filled).
Sqrt_TS30_100	E	. . .	Square root of the test statistic between 30 and 100 MeV (not filled).
Flux100_300	E	cm^{-2} s^{-1}	Integral flux from 100 to 300 MeV.
Unc_Flux100_300	E	cm^{-2} s^{-1}	1σ error on integral flux from 100 to 300 MeV[a].
Sqrt_TS100_300	E	. . .	Square root of the test statistic between 100 and 300 MeV.
Flux300_1000	E	cm^{-2} s^{-1}	Integral flux from 300 MeV to 1 GeV.
Unc_Flux300_1000	E	cm^{-2} s^{-1}	1σ error on integral flux from 300 MeV to 1 GeV[a].
Sqrt_TS300_1000	E	. . .	Square root of the test statistic between 300 MeV and 1 GeV.
Flux1000_3000	E	cm^{-2} s^{-1}	Integral flux from 1 to 3 GeV.
Unc_Flux1000_3000	E	cm^{-2} s^{-1}	1σ error on integral flux from 1 to 3 GeV[a].
Sqrt_TS1000_3000	E	. . .	Square root of the test statistic between 1 and 3 GeV.
Flux3000_10000	E	cm^{-2} s^{-1}	Integral flux from 3 to 10 GeV.
Unc_Flux3000_10000	E	cm^{-2} s^{-1}	1σ error on integral flux from 3 to 10 GeV[a].
Sqrt_TS3000_10000	E	. . .	Square root of the test statistic between 3 and 10 GeV.
Flux10000_100000	E	cm^{-2} s^{-1}	Integral flux from 10 to 100 GeV.
Unc_Flux10000_100000	E	cm^{-2} s^{-1}	1σ error on integral flux from 10 to 100 GeV[a].
Sqrt_TS10000_100000	E	. . .	Square root of the test statistic between 10 and 100 GeV.
Variability_Index	E	. . .	Sum of 2×Log(Likelihood) comparison between the flux fitted in 24 time segments and a flat light curve over the full two-year catalog interval. A value greater than 41.64 indicates <1% chance of being a steady source.
Signif_Peak	E	. . .	Source significance in peak interval in σ units.
Flux_Peak	E	cm^{-2} s^{-1}	Peak integral flux from 100 MeV to 100 GeV.
Unc_Flux_Peak	E	cm^{-2} s^{-1}	1σ error on peak integral flux.
Time_Peak	D	s (MET)	Time of center of interval in which peak flux was measured.
Peak_Interval	E	s	Length of interval in which peak flux was measured.
Flux_History	11E	cm^{-2} s^{-1}	Integral flux from 100 MeV to 100 GeV in each interval (best fit from likelihood analysis with spectral shape fixed to that obtained over two years).
Unc_Flux_History	11E	cm^{-2} s^{-1}	Error on integral flux in each interval using method indicated in Unc_Flag_History column and added in quadrature with 3% systematic component.
Unc_Flag_History	11B		1 if it is half of the difference between the 2σ upper limit and the maximum-likelihood value given in Flux_History, 0 if it is the

Table 12
(Continued)

Column	Format	Unit	Description
			1σ uncertainty derived from a significant detection in the interval.
Extended_Source_Name	18A	. . .	Cross-reference to the ExtendedSources extension for extended sources, if any.
0FGL_Name	18A	. . .	Name of corresponding 0FGL source, if any.
1FGL_Name	18A	. . .	Name of corresponding 1FGL source, if any.
ASSOC_GAM1	18A	. . .	Name of likely corresponding 1AGL source.
ASSOC_GAM2	18A	. . .	Name of likely corresponding 3EG source.
ASSOC_GAM3	18A	. . .	Name of likely corresponding EGR source.
TEVCAT_FLAG	A	. . .	P if positional association with non-extended source in TeVCat.
	. . .		E if associated with a more extended source in TeVCat, N if no TeV association.
ASSOC_TEV	24A	. . .	Name of likely corresponding TeV source from TeVCat.
CLASS1	3A	. . .	Class designation for associated source; see Table 6.
CLASS2	3A	. . .	Second class designation for associated source.
ASSOC1	24A	. . .	Name of identified or likely associated source.
ASSOC2	24A	. . .	Alternate name of identified or likely associated source.
Flags	I	. . .	Source flags (binary coding as in Table 3).

Note. [a] The upper limit is set equal to 0 if the flux in the corresponding energy band is an upper limit (TS < 10 in that band). The upper limits are 2σ.

Table 13
LAT 2FGL FITS Format: ExtendedSources Extension

Column	Format	Unit	Description
Source_Name	18A	. . .	. . .
1FGL_Name	18A	. . .	. . .
RAJ2000	E	deg	Right ascension of centroid.
DECJ2000	E	deg	Declination of centroid.
GLON	E	deg	Galactic longitude of centroid.
GLAT	E	deg	Galactic latitude of centroid.
Model_Form	24A	. . .	Spatial shape (2D Gaussian, Disk, Ring, Template,...)
Model_SemiMajor	E	deg	Long radius of source. Full size for bounded shapes (disk, ring). 68% containment for unbounded shapes (Gaussian).
Model_SemiMinor	E	deg	Short radius of source.
Model_PosAng	E	deg	Position angle of the long axis from celestial north, positive toward increasing R.A. (eastward).
Spatial_Filename	68A	. . .	Name of spatial template file[a].

Note. [a] Spatial_Filename refers to external files that should be included with the catalog distribution.

reconstructing the precise data set that was used for the 1FGL analysis.

The extension `ExtendedSources` contains information about the 12 spatially extended sources that are modeled in the 2FGL catalog, including locations and shapes (Table 13).

REFERENCES

Abdo, A. A., Ackermann, M., Ajello, M., et al. 2009a, Science, 325, 845
Abdo, A. A., Ackermann, M., Ajello, M., et al. 2009b, ApJ, 706, L1
Abdo, A. A., Ackermann, M., Ajello, M., et al. 2009c, ApJ, 701, L123
Abdo, A. A., Ackermann, M., Ajello, M., et al. 2009d, ApJS, 183, 46
Abdo, A. A., Ackermann, M., Ajello, M., et al. 2009e, ApJ, 706, L56
Abdo, A. A., Ackermann, M., Ajello, M., et al. 2009f, Science, 326, 1512
Abdo, A. A., Ackermann, M., Ajello, M., et al. 2009g, ApJ, 707, L142
Abdo, A. A., Ackermann, M., Ajello, M., et al. 2009h, Astropart. Phys., 32, 193
Abdo, A. A., Ackermann, M., Ajello, M., et al. 2010a, A&A, 524, A75
Abdo, A. A., Ackermann, M., Ajello, M., et al. 2010b, ApJ, 709, L152
Abdo, A. A., Ackermann, M., Ajello, M., et al. 2010c, ApJ, 714, 927
Abdo, A. A., Ackermann, M., Ajello, M., et al. 2010d, A&A, 523, A46
Abdo, A. A., Ackermann, M., Ajello, M., et al. 2010e, Science, 328, 725
Abdo, A. A., Ackermann, M., Ajello, M., et al. 2010f, ApJS, 188, 405
Abdo, A. A., Ackermann, M., Ajello, M., et al. 2010g, ApJ, 723, 649
Abdo, A. A., Ackermann, M., Ajello, M., et al. 2010h, A&A, 523, L2
Abdo, A. A., Ackermann, M., Ajello, M., et al. 2010i, ApJ, 708, 1254
Abdo, A. A., Ackermann, M., Ajello, M., et al. 2010j, ApJ, 718, 348
Abdo, A. A., Ackermann, M., Ajello, M., et al. 2010k, ApJ, 713, 146
Abdo, A. A., Ackermann, M., Ajello, M., et al. 2010l, ApJ, 710, L92

Abdo, A. A., Ackermann, M., Ajello, M., et al. 2010m, Science, 329, 817
Abdo, A. A., Ackermann, M., Ajello, M., et al. 2010n, Science, 327, 1103
Abdo, A. A., Ackermann, M., Ajello, M., et al. 2010o, ApJ, 712, 459
Abdo, A. A., Ackermann, M., Ajello, M., et al. 2010p, A&A, 512, A7
Abdo, A. A., Ackermann, M., Ajello, M., et al. 2010q, ApJ, 710, 1271
Abdo, A. A., Ackermann, M., Ajello, M., et al. 2010r, ApJ, 715, 429
Abdo, A. A., Ackermann, M., Ajello, M., et al. 2010s, ApJS, 187, 460
Abdo, A. A., Ackermann, M., Ajello, M., et al. 2011a, ApJ, 736, L11
Abdo, A. A., Ackermann, M., Ajello, M., et al. 2011b, ApJ, 734, 116
Abdo, A. A., Ackermann, M., Ajello, M., et al. 2011c, Science, 331, 739
Abdo, A. A., Ackermann, M., Ajello, M., et al. 2011d, ApJ, 734, 28
Abdo, A. A., Parent, D., Grove, J. E., et al. 2010t, ATel, 3085, 1
Acero, F., Aharonian, F., Akhperjanian, A. G., et al. 2010, MNRAS, 402, 1877
Ackermann, M., Ajello, M., Allafort, A., et al. 2011a, Science, 334, 1103
Ackermann, M., Ajello, M., Allafort, A., et al. 2011b, ApJ, 743, 171
Ackermann, M., Ajello, M., Allafort, A., et al. 2012a, A&A, 538, 71
Ackermann, M., et al. 2012b, ApJ, submitted
Ade, P. A. R., Aghamin, N., Arnaud, M., et al. 2011a, A&A, 536, A7
Ade, P. A. R., Aghamin, N., Arnaud, M., et al. 2011b, A&A, 536, A19
Aharonian, F., Akhperjanian, A. G., Barres de Almeida, U., et al. 2008a, A&A, 483, 509
Aharonian, F., Akhperjanian, A. G., Barres de Almeida, U., et al. 2008b, A&A, 477, 353
Aharonian, F., Akhperjanian, A. G., Barres de Almeida, U., et al. 2009, ApJ, 692, 1500
Aharonian, F., Akhperjanian, A. G., Bazer-Bachi, A. R., et al. 2006, ApJ, 636, 777
Atwood, W. B., Abdo, A. A., Ackermann, M., et al. 2009, ApJ, 697, 1071
Bates, S. D., Bailes, M., Bhat, N. D. R., et al. 2011, MNRAS, 416, 2455

Baumgartner, W. H., Tueller, J., Markwardt, C., & Skinner, G. 2010, BAAS, 42, 675
Bird, A. J., Bazzano, A., Bassani, L., et al. 2010, ApJS, 186, 1
Campana, R., Massaro, E., Gasparrini, D., Cutini, S., & Tramacere, A. 2008, MNRAS, 383, 1166
Casandjian, J.-M., & Grenier, I. A. 2008, A&A, 489, 849
Chaves, R. C. G., Renaud, M., Lemoine-Goumard, M., & Goret, P. 2008, in AIP Conf. Proc. 1085, High Energy Gamma-ray Astronomy: Proc. 4th Intl. Mtg. on High Energy Gamma-ray Astronomy, ed. F. A. Aharonian, W. Hofmann, & F. Rieger (Melville, NY: AIP), 372
Cheung, C. C., Reyes, L., Longo, F., & Iafrate, G. 2008, ATel, 1788, 1
Ciprini, S., Tosti, G., Marcucci, F., et al. 2007, in AIP Conf. Proc. 921, The First GLAST Symposium, ed. S. Ritz, P. Michelson, & C. A. Meegan (Melville, NY: AIP), 546
Clark, J. S., Larionov, V. M., & Arkharov, A. 2005, A&A, 435, 239
Cognard, I., Guillemot, L., Johnson, T. J., et al. 2011, ApJ, 732, 47
Corbet, R. H. D., Cheung, C. C., Kerr, M., et al. 2011, ATel, 3221, 1
Dame, T. M., Hartmann, D., & Thaddeus, P. 2001, ApJ, 547, 792
Damiani, F., Maggio, A., Micela, G., & Sciortino, S. 1997, ApJ, 483, 350
D'Ammando, F. 2011, ATel, 3394, 1
De Becker, M., Linder, N., & Rauw, G. 2010, New Astron., 15, 76
Dias, W. S., Alessi, B. S., Moitinho, A., & Lépine, J. R. D. 2002, A&A, 389, 871
Donato, D., & Cheung, C. C. 2010, ATel, 2966, 1
Donato, D., & Perkins, J. S. 2011, ATel, 3452, 1
Farnier, C., Walter, R., & Leyder, J.-C. 2011, A&A, 526, A57
Flesch, E. 2010, PASA, 27, 283
Górski, K. M., Hivon, E., Banday, A. J., et al. 2005, ApJ, 622, 759
Green, D. A. 2009, Bull. Astron. Soc. India, 37, 45
Grenier, I. A., Casandjian, J.-M., & Terrier, R. 2005, Science, 307, 1292
Grondin, M.-H., Funk, S., Lemoine-Goumard, M., et al. 2011, ApJ, 738, 42
Harris, W. E. 1996, AJ, 112, 1487
Hartman, R. C., Bertsch, D. L., Bloom, S. D., et al. 1999, ApJS, 123, 79
Haslam, C. G. T., Klein, U., Salter, C. J., et al. 1981, A&A, 100, 209
Hays, E., Cheung, C. C., & Reyes, L. 2008, ATel, 1771, 1
Healey, S. E., Romani, R. W., Cotter, G., et al. 2008, ApJS, 175, 97
Healey, S. E., Romani, R. W., Taylor, G. B., et al. 2007, ApJS, 171, 61
Helene, O. 1983, Nucl. Instrum. Methods Phys. Res., 212, 319
HESS Collaboration. 2011a, A&A, 525, A45
HESS Collaboration. 2011b, A&A, 529, A49
HESS Collaboration. 2011c, A&A, 525, A46
HESS Collaboration. 2011d, A&A, 531, L18
Hessels, J. W. T., Roberts, M. S. E., McLaughlin, M. A., et al. 2011, in AIP Conf. Proc. 1357, Radio Pulsars: An Astrophysical Key to Unlock the Secrets of the Universe, ed. M. Burgay et al. (Melville, NY: AIP), 40
Katagiri, H., Tibaldo, L., Ballet, J., et al. 2011, ApJ, 741, 44
Keith, M. J., Johnston, S., Ray, P. S., et al. 2011, MNRAS, 414, 1292
Lamb, R. C., & Macomb, D. J. 1997, ApJ, 488, 872

Lemoine-Goumard, M., Zavlin, V. E., Grondin, M.-H., et al. 2011, A&A, 533, A102
Liu, Q. Z., van Paradijs, J., & van den Heuvel, E. P. J. 2006, A&A, 455, 1165
Liu, Q. Z., van Paradijs, J., & van den Heuvel, E. P. J. 2007, VizieR Online Data Catalog, 346, 90807
Maíz-Apellániz, J., Walborn, N. R., Galué, H. Á., & Wei, L. H. 2004, ApJS, 151, 103
Manchester, R. N., Hobbs, G. B., Teoh, A., & Hobbs, M. 2005, AJ, 129, 1993
Massaro, E., Giommi, P., Leto, C., et al. 2009, A&A, 495, 691
Mattox, J. R., Bertsch, D. L., Chiang, J., et al. 1996, ApJ, 461, 396
Murphy, T., Sadler, E. M., Ekers, R. D., et al. 2010, MNRAS, 402, 2403
Ohm, S., Fernandes, M. V., de Ona Wilhelmi, E., et al. 2010, in Proc. 25th Texas Symposium on Relativistic Astrophysics, ed. F. Rieger, C. van Eldik, & W. Hoffman, http://pos.sissa.it/cgi-bin/reader/conf.cgi?confid=123
Pittori, C., Verrecchia, F., Chen, A. W., et al. 2009, A&A, 506, 1563
Ransom, S. M., Ray, P. S., Camilo, F., et al. 2011, ApJ, 727, L16
Renaud, M., Goret, P., & Chaves, R. C. G. 2008, in AIP Conf. Proc. 1085, High Energy Gamma-ray Astronomy: Proc. 4th Intl. Mtg. on High Energy Gamma-ray Astronomy, ed. F. A. Aharonian, W. Hofmann, & F. Rieger (Melville, NY: AIP), 281
Rolke, W. A., López, A. M., & Conrad, J. 2005, Nucl. Instrum. Methods Phys. Res. A, 551, 493
Sanchez, D., & Fegan, S. 2010, ATel, 3014, 1
Sanders, D. B., Mazzarella, J. M., Kim, D.-C., Surace, J. A., & Soifer, B. T. 2003, AJ, 126, 1607
Schlegel, D. J., Finkbeiner, D. P., & Davis, M. 1998, ApJ, 500, 525
Schmidt, K., Priebe, A., & Boller, T. 1993, Astron. Nachr., 314, 371
Smith, D. A., Guillemot, L., Camilo, F., et al. 2008, A&A, 492, 923
Sokolovsky, K. V., Schinzel, F. K., Healey, S. E., et al. 2010, ATel, 2666, 1
Sowards-Emmerd, D., Romani, R. W., & Michelson, P. F. 2003, ApJ, 590, 109
Starck, J.-L., & Pierre, M. 1998, A&AS, 128, 397
Strong, A. W., Moskalenko, I. V., & Ptuskin, V. S. 2007, Annu. Rev. Nucl. Part. Sci., 57, 285
Su, M., Slatyer, T. R., & Finkbeiner, D. P. 2010, ApJ, 724, 1044
Tam, P. H. T., Huang, R. H. H., Takata, J., et al. 2011a, ApJ, 736, L10
Tam, P. H. T., Hui, C. Y., Huang, R. H. H., et al. 2010, ApJ, 724, L207
Tam, P. H. T., Kong, A. K. H., Hui, C. Y., et al. 2011b, ApJ, 729, 90
Tanaka, T., Allafort, A., Ballet, J., et al. 2011, ApJ, 740, L51
Tavani, M., Bulgarelli, A., Vittorini, V., et al. 2011, Science, 331, 736
Tavani, M., Sabatini, S., Pian, E., et al. 2009, ApJ, 698, L142
Tibolla, O., Komin, N., Kosack, K., & Naumann-Godo, M. 2008, in AIP Conf. Proc. 1085, High Energy Gamma-Ray Astronomy: Proc. 4th Intl. Mtg. on High Energy Gamma-ray Astronomy, ed. F. A. Aharonian, W. Hofmann, & F. Rieger (Melville, NY: AIP), 249
van der Hucht, K. A. 2001, New Astron. Rev., 45, 135
Vasileiou, V., Chiang, J., Omodei, N., et al. 2011, ATel, 3162, 1
Véron-Cetty, M.-P., & Véron, P. 2010, A&A, 518, A10
Wallace, E. 2010, ATel, 2528, 1
Yasuda, H., Takahashi, H., & McConville, W. 2009, ATel, 2081, 1